THREE-DIMENSIONAL INVERSION OF POTENTIAL-FIELD DATA WITH APPLICATION TO KANSAS

by

Jianghai Xia

B. S., Chengdu College of Geology, Chengdu, P. R. China, 1976
M. S., Chinese Academy of Geological Sciences, Beijing, P. R. China, 1982

Submitted to the Department of
Geology and the Faculty of the
Graduate School of the University
of Kansas in partial fulfillment
of the requirements for the degree of
Doctor of Philosophy

Donald R. Sproul
Professor in Charge

Robert H. Goldstein

Martin S. Hanna
Committee Members

Date Defended: ____________________

ABSTRACT

Information about the thickness of the Kansas crust and the distribution of lithologies in the uppermost Precambrian of Kansas is obtained through inversion of gravity and magnetic data, constrained by drilling records. More than 59,000 gravity measurements, 72,000 line-km of aeromagnetic measurements, and 3,400 penetrations to the Precambrian basement are used in the study. Because direct inversion of potential-field data is possible only under the most restricted conditions, inversion is accomplished by iterative forward modeling.

New procedures are developed for:

a) the correction of topographic distortions in gravity and magnetic data. The numerical equivalent source is used in both the spatial domain and the frequency domain. The frequency domain algorithm is very efficient and is suitable for use with large data sets;

b) inversion by iterative forward modeling, in the frequency domain, of gravity and magnetic anomalies due to a layer of constant density with undulating surfaces. The derived procedure is very stable and therefore does not require either specific filtering of the input data or a reasonable initial model for convergence;

c) inversion by iterative forward modeling, in the frequency domain, of gravity anomalies due to a layer with exponentially varying density and undulating boundaries. The formula used in part b) is shown to be a special case of this general solution.

PREFACE

A major effort of the Kansas Geological Survey, to collect gravity data in the grids of 1.6 km by 1.6 km (1 mile by 1 mile) in eastern Kansas and 1.6 km by 3.2 km (1 mile by 2 mile) in western Kansas, is drawing to a close after more than 15 years of work. More than 59,000 gravity-station measurements are available at the Kansas Geological Survey (Lam, 1986; Xia and Sprowl, 1992). Approximately 72,000 line-km (45,000 line-mi) of digitally recorded aeromagnetic data have been available since the early 1980's (Yarger et al., 1981). These potential-field data can be used to study the Precambrian basement and the thickness of the earth's crust in Kansas. The results of seismic refraction in Kansas (Steeples and Miller, 1989), the results from earthquake seismograms (Miller, 1983), and more than 3,400 drill holes which penetrated to the Precambrian constrain the study.

In Chapter 1, I provide the background information of geological setting and geophysical studies in Kansas. I discuss the accuracies of the potential-field data and describe the objectives of the study. Chapter 2 deals with data processing. I discuss gridding, topographic correction, and separation of potential-field anomalies. The heart of the chapter is the topographic correction. I develop approaches to correct distortions in potential-field data both in the spatial domain and the wavenumber domain and apply them to the Kansas data (Xia and Sprowl, 1991; Xia et al., 1991). I provide the mathematic derivation of the orthogonal-polynomial fit in Appendix A and I show the convergence of the power series used in the topographic correction in Appendix B. Chapter 3 handles the problem of inverting potential-field data with a constant density/magnetization contrast model (Xia and Sprowl, 1990; Xia, 1991; Xia and Sprowl, 1992). Chapter 4 expands the approach developed in Chapter 3 to an exponential density contrast model (Xia and Sprowl, 1990; Xia, 1991). In Chapter 5, the approach developed in Chapters 3 and 4 are applied to the data of the whole state. In Appendix C, I give the derivation of the formula for calculating the gravity anomaly due to an exponential density contrast model and also show that the linear density contrast model is a special case of the exponential density contrast model.

CONTENTS

LIST OF FIGURES

LIST OF TABLES

CHAPTER 1

INTRODUCTION

1.1. Geological Setting

Phanerozoic rocks cover virtually all of the Precambrian basement in Kansas, except for a large inclusion of Precambrian granite found in the Cretaceous mica peridotite of Rose Dome in Woodson County (Bickford et al., 1971; Franks et al., 1971). The contour map of the top of the Precambrian rocks in Kansas (Cole, 1976) is shown in Figure 1-1. There are more than 3,400 wells (Figure 1-2) drilled to the Precambrian in Kansas (Cole and Watney, 1985). Most of them are located in the Central Kansas Uplift and Nemaha Uplift regions. The well data and Cole's map define the topographic surface of the Precambrian basement. The thickness of the Phanerozoic rocks changes from more than 3,000 m (9,840 ft) in Meade County of southwestern Kansas to less than 200 m (660 ft) in the Nemaha uplift of northeastern Kansas. Based mostly on well cuttings, Bickford et al. (1981) presented a preliminary distribution of rock types in the Precambrian of Kansas (Figure 1-3).

The Central North American Rift System (CNARS) in Kansas (e.g., Bickford et al., 1981; Berendsen et al., 1988), a north-northeast - south-southwest oriented feature, is the only Precambrian structural high that produces distinguishable gravity and magnetic anomalies (Figure 1-4). The CNARS is also called the Midcontinent Rift System (MRS) and the Midcontinent Geophysical Anomaly (MGA). The MRS is an areally extensive rift basin characterized by intrusive and volcanic rocks followed by and/or interspersed with immature clastic sedimentation (Berendsen et al., 1988). The Texaco Poersch #1 well provided valuable information about the MRS in Kansas (Berendsen et al., 1988). The depth to the Precambrian basement in Texaco Poersch #1, which is located in the MRS of the northeastern Kansas, is 867 m (2846 ft). The Precambrian rocks penetrated by the well can be divided into two distinct groups: the upper succession down to 2,264 m (7,429 ft) is mafic volcanics and subordinate mafic and acidic intrusives, the lower succession from 2,264 m to 3,444 m (11,300 ft) is arkose and subarkose (Berendsen et al., 1988). The central Kansas uplift and the

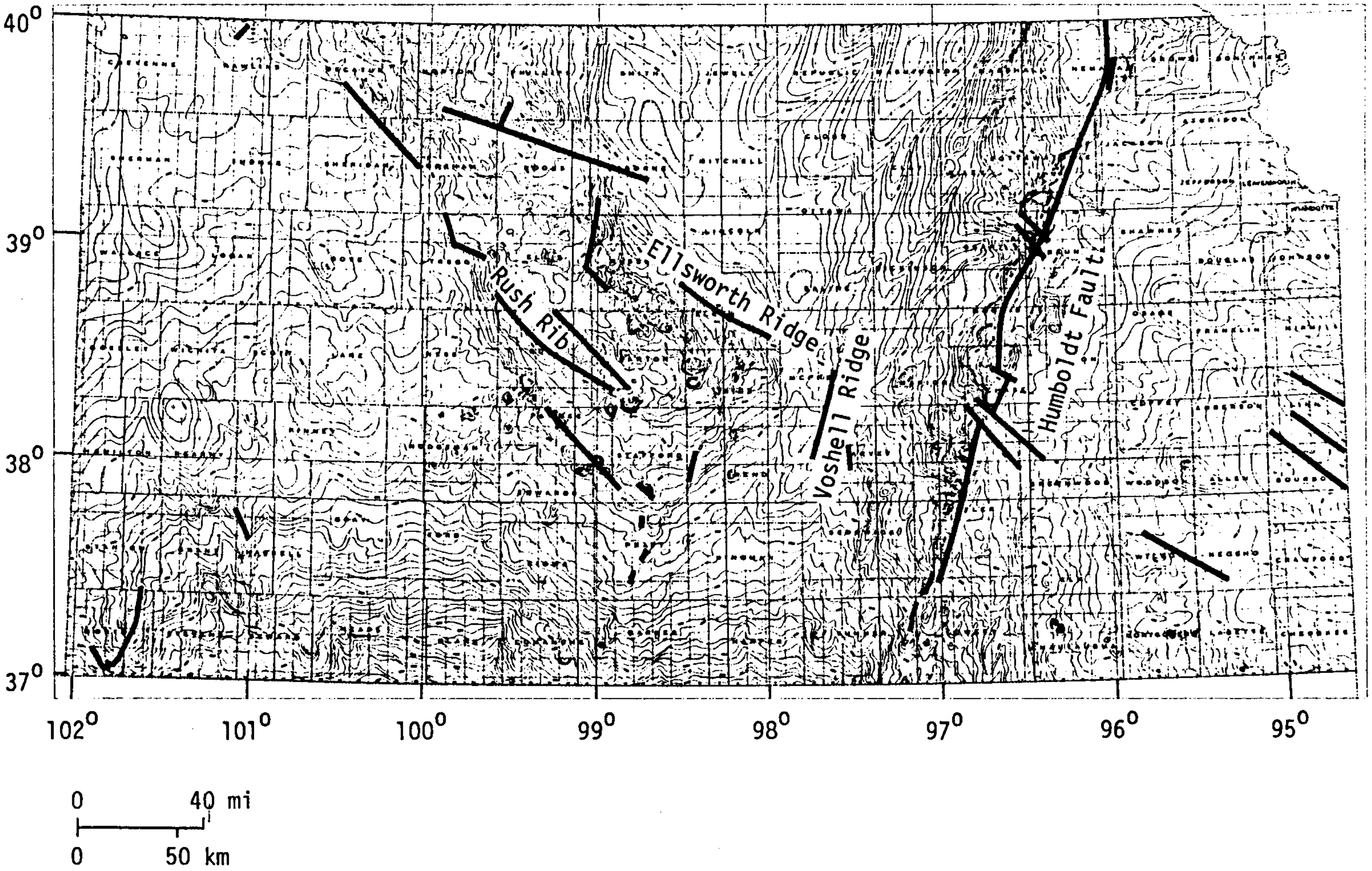

Figure 1-1. Configuration of the top of the Precambrian rocks in Kansas. After Cole (1976). Adapted from Yarger (1985).

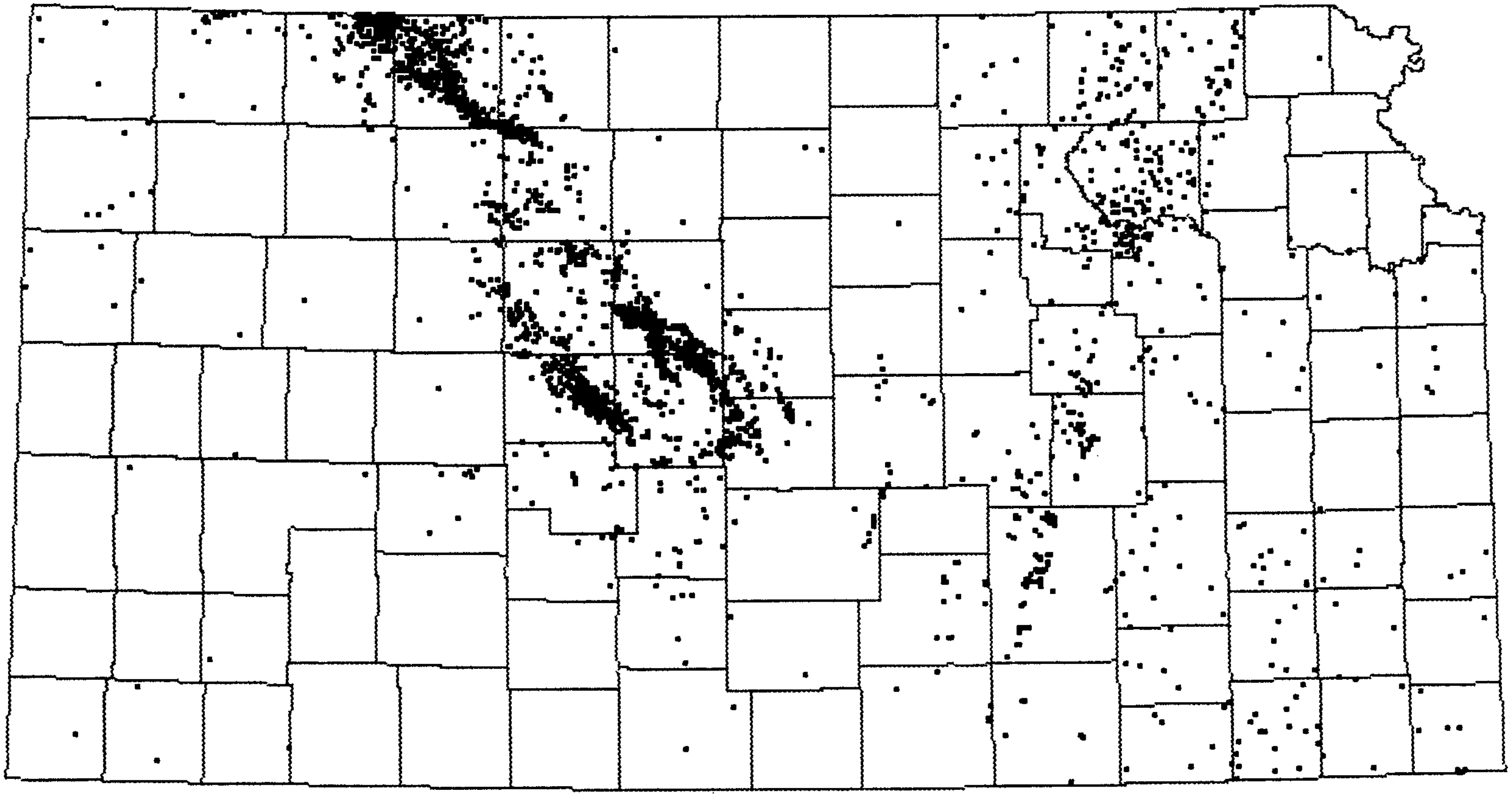

Figure 1-2. Distribution of the well drilled to the Precambrian basement. Based on the database from Kansas Geological Survey.

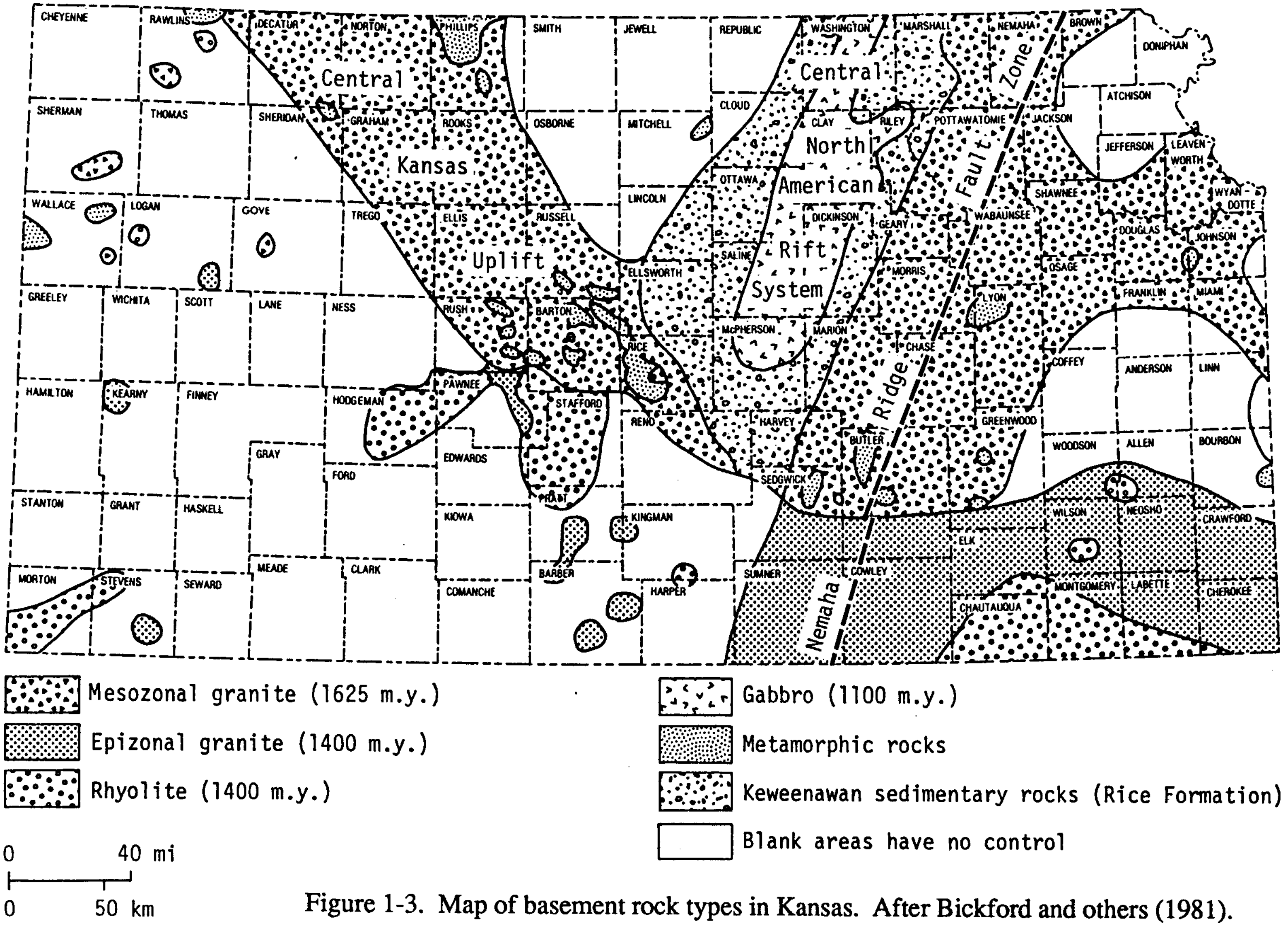

Figure 1-3. Map of basement rock types in Kansas. After Bickford and others (1981).

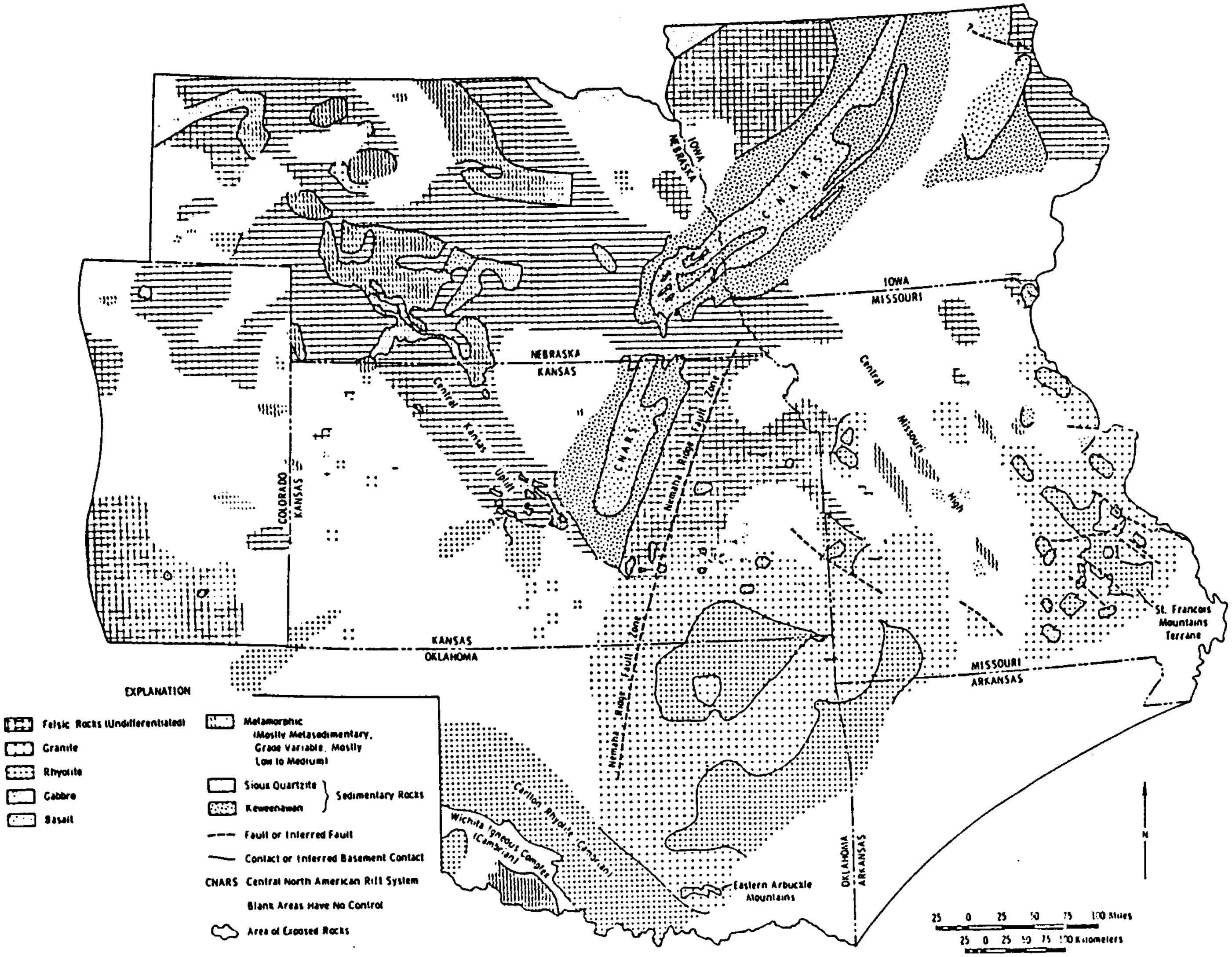

Figure 1-4. Map of basement-rock types in the central Midcontinent region. After Bickford and others (1981).

Nemaha uplift are two major post-Mississippian structural highs that dominate the subsurface geology in Kansas. The Nemaha uplift, a north-northeast - south-sothwest oriented feature, is the principal boundary between the Salina and Forest City basins (Steeples, 1982). The central Kansas uplift, a northwest—southeast oriented feature, is the west boundary of the Salina basin. The Humboldt fault system marks the boundary between the Nemaha uplift and the Cherokee and Forest City basins (Newell et al., 1987). Microearthquake studies (Steeples, 1982; and Hildebrand et al. , 1988) indicate that the Humboldt Fault system is still active. The Pratt anticline, which extends southward from the central Kansas uplift, separates the Hugoton basin in southwest Kansas from the Sedgwick basin in south-central Kansas (Newell, 1987).

1.2. Geophysical Studies

More than 59,000 gravity-station measurements and approximately 72,000 line-km (45,000 line-mi) of digitally recorded aeromagnetic data are available at the Kansas Geological Survey. These potential-field data contain useful information about the Precambrian basement and the Moho discontinuity in Kansas. Lam (1986) used filtering methods to systematically study the Bouguer anomaly. Lam and Yarger (1989) discussed the major features of the gravity anomaly. They showed that there are two dominant lineations in gravity, one oriented N40E and associated with the MGA, and the other oriented N45W, probably due to aligned pre-rift fractures. Yarger (1983, 1985) used filtering techniques to study the Kansas basement based on analysis of aeromagnetic data. He showed that the MRS does not terminate in central Kansas, but is continuous along a southwestern trend to at least the Kansas-Oklahoma border. Yarger also suggested evidence for a distinct east-west trending boundary across central Kansas between the 1,600-1,700 Ma mesozonal granitic terrane to the north and a younger, about 1,400 Ma epizonal granitic terrane to the south (Figure 1-5). Two-dimensional geophysical models of the MRS were shown which satisfy potential fields and seismic data (Yarger, 1989; Lam and Yarger, 1989; Somanas et al., 1989; and Woelk and Hinze, 1991). A three-dimensional model of the MRS has also been calculated from gravity data (Xia and Sprowl, 1990).

Steeples (1982) studied the Salina-Forest City interbasin boundary using

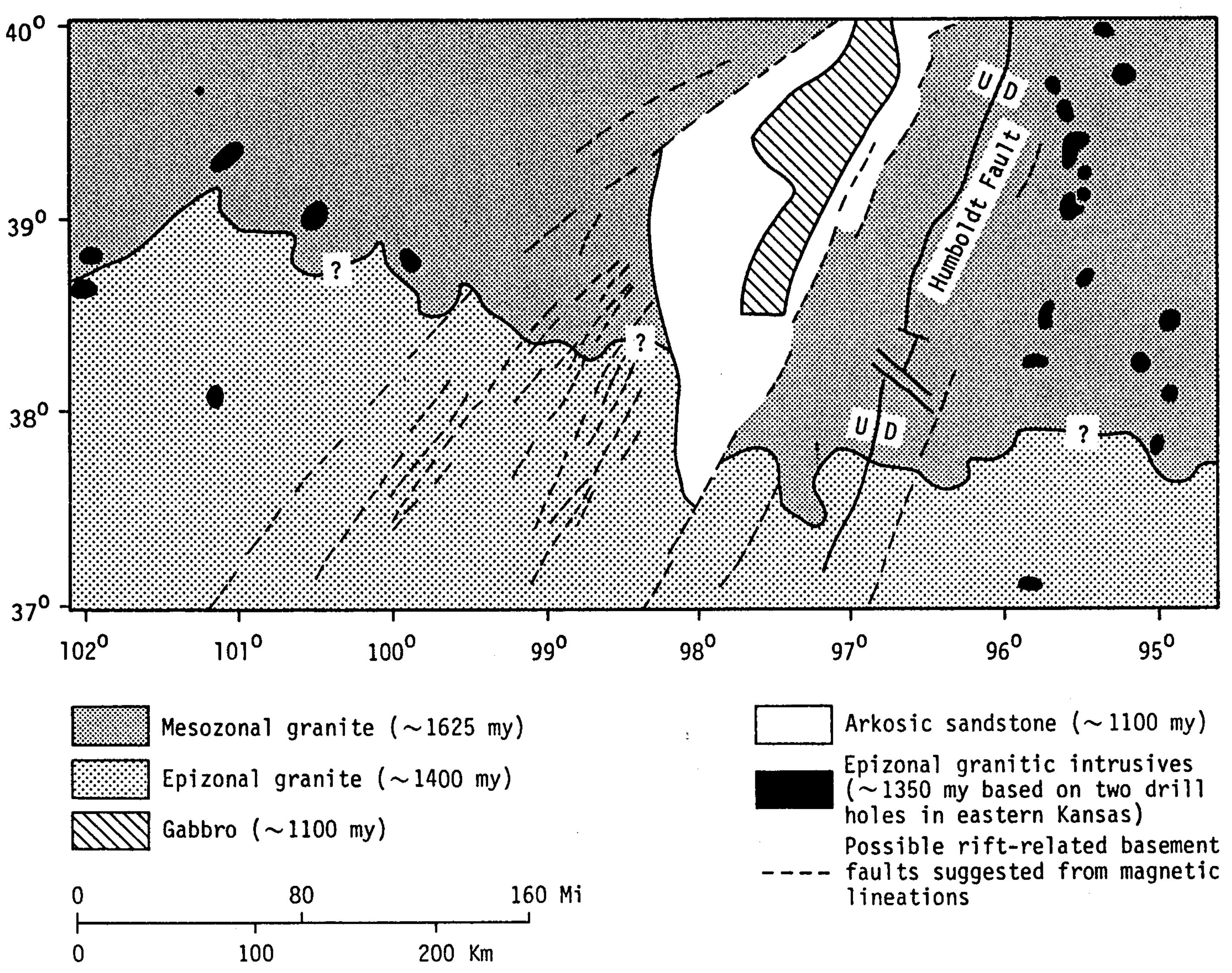

Figure 1-5. Precambrian Terranes in Kansas. After Yarger (1985).

seismic data and pointed out that the edges of the Salina and Forest City basins should become of increased economic interest. Microearthquake studies (Steeples, 1982; and Hildebrand et al., 1988) indicate that the Humboldt Fault system is still active along a zone 400 km (240 miles) long (north-south) and 50 km (30 miles) wide (east-west) coincident with the Nemaha uplift from southeastern Nebraska to north-central Oklahoma. Miller (1983) used earthquake seismograms to study the crust in Kansas and postulated the presence of several anomalous velocity areas in eastern Kansas (Figure 1-6). Steeples and Miller (1989) studied refraction-profile data from Concordia, Kansas, to Agate, Colorado (Figure 1-7). The results showed an average crustal velocity of 6.1 km/sec (3.7 mi/sec), an average upper-mantle P_n phase velocity of 8.29 km/sec (4.97 mi/sec), depth to Moho of 36 km (23 mi) at Concordia, Kansas, and depth to Moho of 46 km (29 mi) at Agate, Colorado. The results from seismic data provide a useful constraint on the potential-field inversion.

1.3. Errors in Potential-field Data

It is shown below that the root-mean-square error in the Bouguer gravity is around 0.1 mGal. The error in aeromagnetic data is 3 nT (Yarger, 1983).

1.3.1. Bouguer gravity

Bouguer gravity is defined as the following,

$$g_b = g_a - g_r - 0.3086 \times h + 0.04193 \times d \times h, \tag{1.1}$$

where g_b is the Bouguer gravity, g_a is the measured absolute gravity after the "meter drift" correction, g_r is the reference gravity field, units of g_b, g_a, and g_r are in mGal, and h is the elevation in meters.

For $d = 2.67$ g/cm^3, the upper crustal density, it becomes,

$$g_b = g_a - g_r - 0.19655 \times h, \tag{1.2}$$

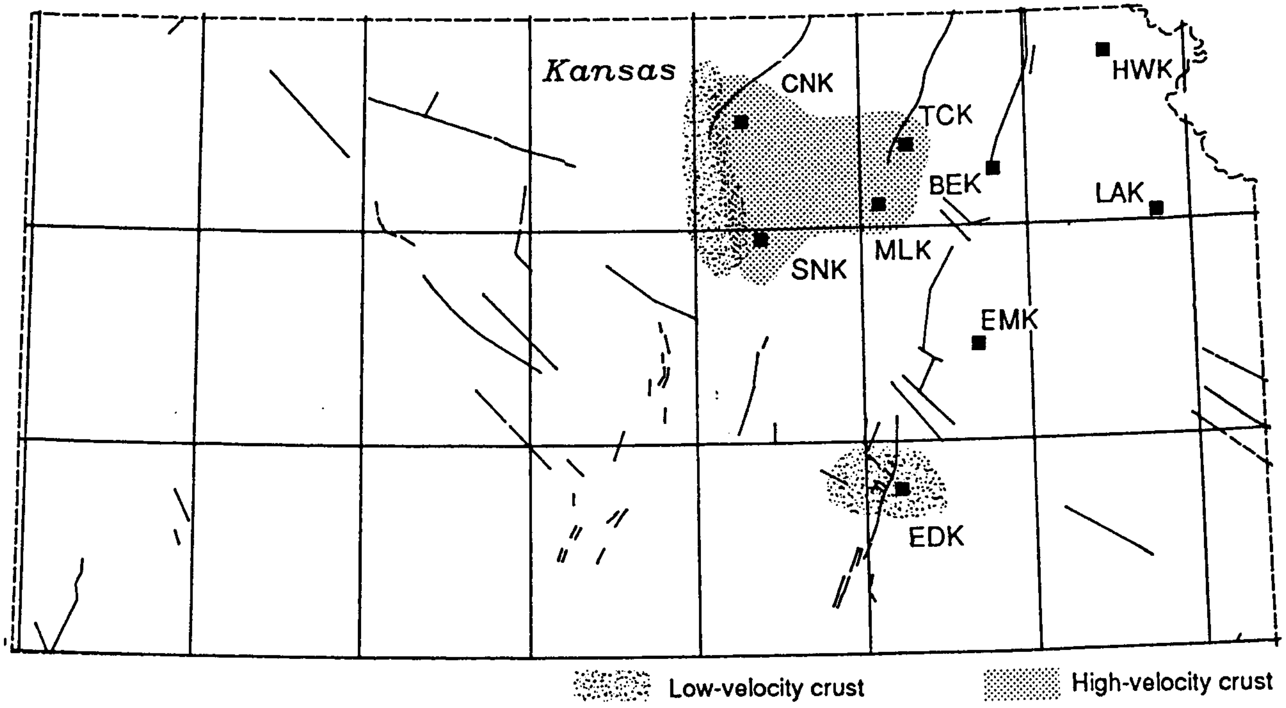

Figure 1-6. Postulated the presence of several anomalous velocity areas in the crust of eastern Kansas. After Miller (1983).

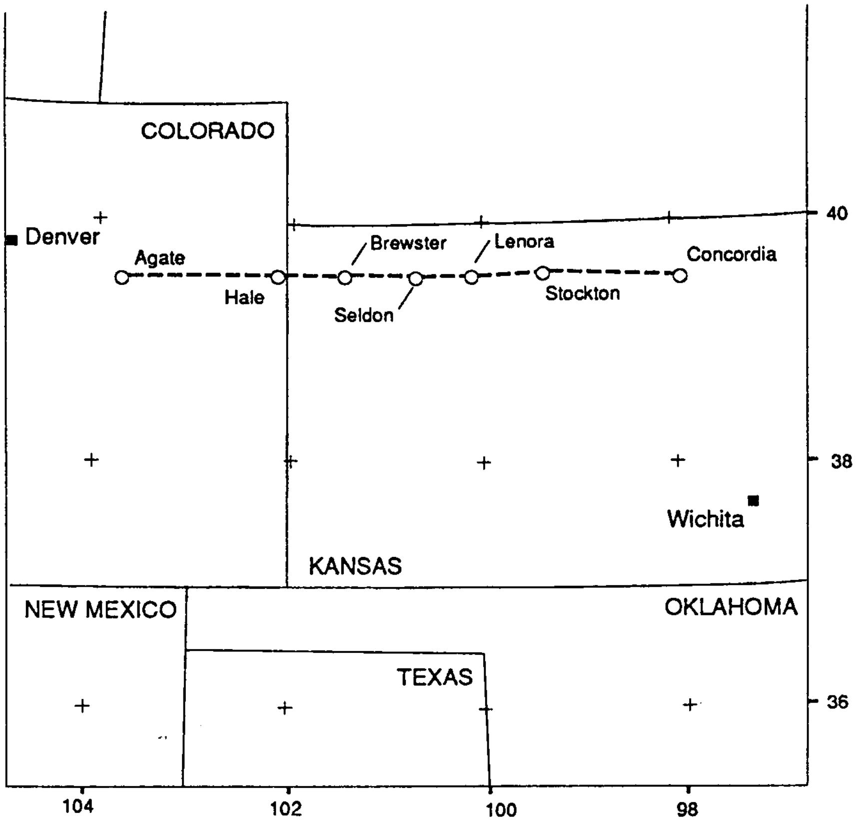

LOCATION OF LINE OF SHOTS. Open circles show shotpoints; recordings were made along dashed line.

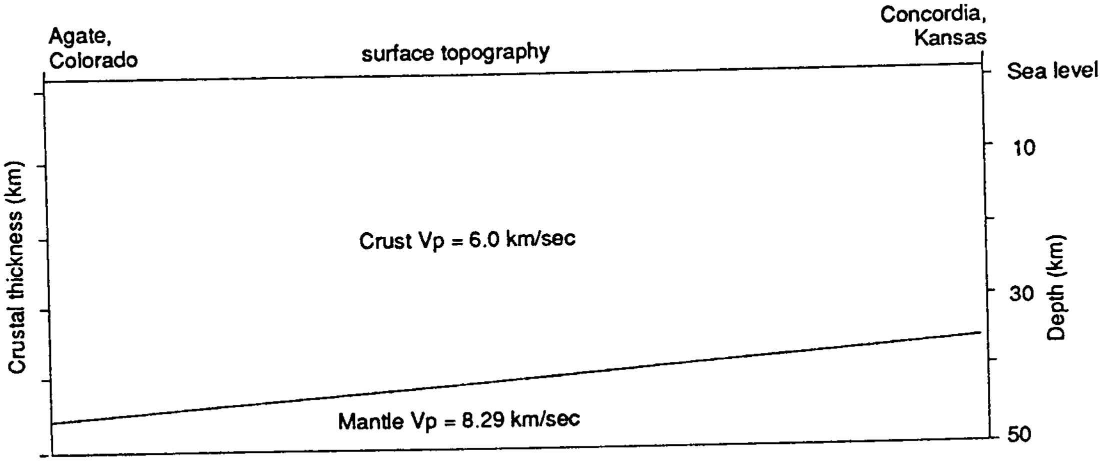

Figure 1-7. Seismic refraction profile and results. After Steeples and Miller (1989).

Based on error transformation theory (e.g., Snedecor and Cochran, 1989, p. 286) and assuming that errors are white noise, the error in g_b can be written

$$\delta g_b = \left[(\delta g_a)^2 + (\delta g_r)^2 + (0.19665 \times \delta h)^2\right]^{1/2}, \qquad (1.3)$$

where δg_b is the root-mean-square (rms) error in the Bouguer gravity, δg_a is the rms error in the measured absolute gravity after the "meter drift" correction, δg_r is the rms error in the reference gravity field, and δh is the rms error in elevation.

δg_a consists of three parts: 1) the rms error in the "meter drift" correction, 2) the rms error in gravity readings and the base-tie readings, which tie the base stations of each block to DOD (Department of Defense) reference stations, and 3) the rms error in the DOD value. The rms error in the "meter drift" correction is 0.01 mGal (Lam, 1986). The rms error in the gravity readings and the base-tie readings is 0.064 mGal, which is obtained by calculating misfit on the 404 overlapped stations. The rms error in DOD stations is about 0.1 mGal (Lam, 1986). Therefore,

$$\delta g_a = \left(0.01^2 + 0.064^2 + 0.1^2\right)^{1/2} = 0.119 \text{ mGal}. \qquad (1.4)$$

The reference field is given by (e.g., Mittermayer, 1969)

$$g_r = 978{,}031.85 \times \left(1 + 0.005278895 \times \sin^2\phi + 0.000023462 \times \sin^4\phi\right) \text{ mGal},$$

where ϕ is the north latitude. Taking the derivative with respect to ϕ and choosing an Earth radius = 6.367×10^8 cm, I obtain

$$\frac{\partial g_r}{\partial \phi} = 1.622 \cos\phi \delta H \text{ mGal/km},$$

where δH is the rms error in N-S location, normally δH is less than 0.01 km. The average latitude ϕ in Kansas is 38.5 degrees. Therefore

$$\delta g_r = \left|\frac{\partial g_r}{\partial \phi}\right| = 0.013 \text{ mGal}. \tag{1.5}$$

The elevation of gravity stations is taken from the topographic map of the 7.5 minute series, which has an accuracy of 0.3 m (1 ft), so the error associated with the elevation is

$$0.19665 \times \delta h = 0.19665 \times 0.3 = 0.059 \text{ mGal}. \tag{1.6}$$

Uncertainty in station elevation arises from errors in mapped elevation as well as errors in station location and therefore may be larger than estimated above. The uncertainty in the elevation could be as large as 3 feet (Steeples, 1992) and the rms error in the Bouguer gravity data associated with the elevation will be 0.177 mGal in this case.

If assuming the rms error in the elevation as 1 foot, the rms error in the Bouguer gravity is (substituting Equations (1.4) - (1.6) into Equation (1.3))

$$\delta g_b = \left(0.119^2 + 0.013^2 + 0.059^2\right)^{1/2} = 0.133 \text{ mGal}.$$

Given a maximum error in the DOD values, the uncertainty in the Bouguer gravity values is 0.133 mGal. With minimum error in the DOD values, the uncertainty is 0.089 mGal. If choosing the rms error in the elevation as 3 feet, the rms error in the Bouguer gravity is 0.2 mGal. Calculations in this thesis assume an intermediate value of 0.1 mGal.

1.3.2. Aeromagnetic data

The International Geomagnetic Reference Field 1975 (IGRF) was computed at each measurement location for the appropriate day and subtracted from the total-intensity-magnetic field (Yarger, 1983). The temporal variations in the magnetic field were removed by analysis of the mismatches of magnetic-field value at tie line-flight line intersections (Yarger et al., 1978b). After fifth-order temporal variation adjustment to tie lines and flight lines, the residuals were normally distributed about zero with the root-mean-square of 3 nT (Yarger, 1983).

1.4. Objectives of the Study

An objective of this study is to develop an inverse technique which converges stably and is efficient enough to apply to the data for the entire state. This is only possible in the wavenumber domain. Iterative forward modeling based on constant and exponential density contrast models is used in this study because the forward modeling procedure with fixed distance between grid points is stable and efficient. At the same time, if the interface can be fit to a grid of data there is, in theory, a unique solution to the inverse problem given error-free potential-field data with a known average-depth-to-interface and a known average density/magnetization.

The inversion results from this study are constrained by results from seismic data (Steeples, 1982; Miller, 1983; Steeples and Miller, 1989) and results from well data (Cole, 1976; Cole and Watney, 1985; and Berendsen et al., 1988) and the known geology (Bickford et al., 1981, Steeples and Bickford, 1981). The inversion results are compared with the work done by Yarger (1983, 1985), Lam (1986), Lam and Yarger (1989), and others.

Before inversion of potential-field data, topographic correction and anomaly separation must be done. I have developed a fast and accurate approach in the wavenumber domain for correction of topographic distortions in potential-field data. I also present an approach in the spatial domain, useful for small data sets, which suffers less from edge effect problems.

CHAPTER 2

DATA PROCESSING

2.1. Introduction

In order to obtain the Bouguer anomaly, standard corrections must be applied to the measured gravity, which include: the "meter drift" correction, the normal field correction, and elevation associated corrections (the free-air correction and Bouguer correction). The Bouguer anomaly is still on the measurement surface after standard corrections, which means that distortions due to topographic relief of the measurement surface remain in the Bouguer gravity. The aeromagnetic data in Kansas were measured on three different horizontal planes (Yarger et al., 1981).

In this chapter, I begin with a description of the data gridding procedure. Then I discuss methods, in both the spatial and wavenumber domains, to reduce the data onto a horizontal plane, which I call the topographic correction. Sources of magnetic anomalies are mostly restricted to the middle crust, but gravity measurements are affected by sources at all depths. Inversion of the data for the geology at a particular depth must be preceded by separation of regional and residual anomalies. This chapter ends with a discussion of anomaly separation methods.

2.2. Gridding

Gridding is a necessary step for most potential-field data processing and inversion. The gridding method of preference is kriging, named after D. G. Krige, a south African mining engineer and pioneer in the application of statistical techniques to mine evaluation, (Krige, 1966). Under kriging, the gridded values are unbiased and errors are minimized. SURFACE III (Sampson, 1988) provides the kriging computer code.

There are more than 59,000 gravity stations measured on the topographic surface in Kansas. The data are spaced about 1.6 km by 3.2 km (1 mi by 2 mi) in western Kansas and about 1.6 km by 1.6 km (1 mi by 1 mi) in most of eastern Kansas except between Salina and Topeka, which is covered at 1.6 km by 6.4 km (1 mi by 4 mi). The highest point on the topography is 1,231 m (4,039 ft) above sea level in western Kansas and the lowest is 215 m (706 ft) above sea level in eastern Kansas. I used kriging in SURFACE III (Sampson, 1988) to grid the Bouguer gravity data to 1.6 km by 1.6 km (1 mi by 1 mi). The final gridded data set for the whole state is 205 × 408 points. The Bouguer anomaly map is shown Figure 2-1.

There are about 72,000 line-km (45,000 line-mile) of aeromagnetic data in Kansas. The data density along a flight line is 8-11 points/km (12-18 points/mile). The distance between flight lines is 3.2 km (2 mi). The data were measured at three different elevations, 760 m (2,500 ft) above sea level in eastern Kansas, 910 m (3,000 ft) and 1,370 m (4,500 ft) above sea level in the east half and west half of western Kansas, respectively. There is a transition zone about 5-15 km (3-9 mi) wide in about the middle of western Kansas, across which the plane changed elevation from 910 m (3,000 ft) to 1,370 m (4,500 ft). Elevations in the transition zone are linearly interpolated (Yarger, 1985). I used kriging in SURFACE III (Sampson, 1988) to grid these data to 1.6 km by 1.6 km (1 mi by 1 mi). The final gridded data set is 205 × 408 points. The Kansas aeromagnetic map exhibits an offset between the eastern and western parts due to data acquisition factors. This offset is corrected by subtraction of 1,236 nT from eastern Kansas and 1,054 nT from western Kansas. Subtraction is executed prior to determination of equivalent source and yields a zero average value for each half of the state. After correction, the magnetic anomaly satisfies Gauss's law (e.g., Halliday and Resnick, 1981, p. 451):

$$\oint_{s} t(\vec{x})d\vec{x} = 0,$$

where s is a closed surface, $t(\vec{x})$ is magnetic anomaly, and $\vec{x}$ is a variable vector on the surface s. When the measurement surface is large enough, I can treat it as the surface s in Gauss's equation. The final aeromagnetic map is shown in Figure 2-2. The original aeromagnetic map is given by Yarger et al. (1981).

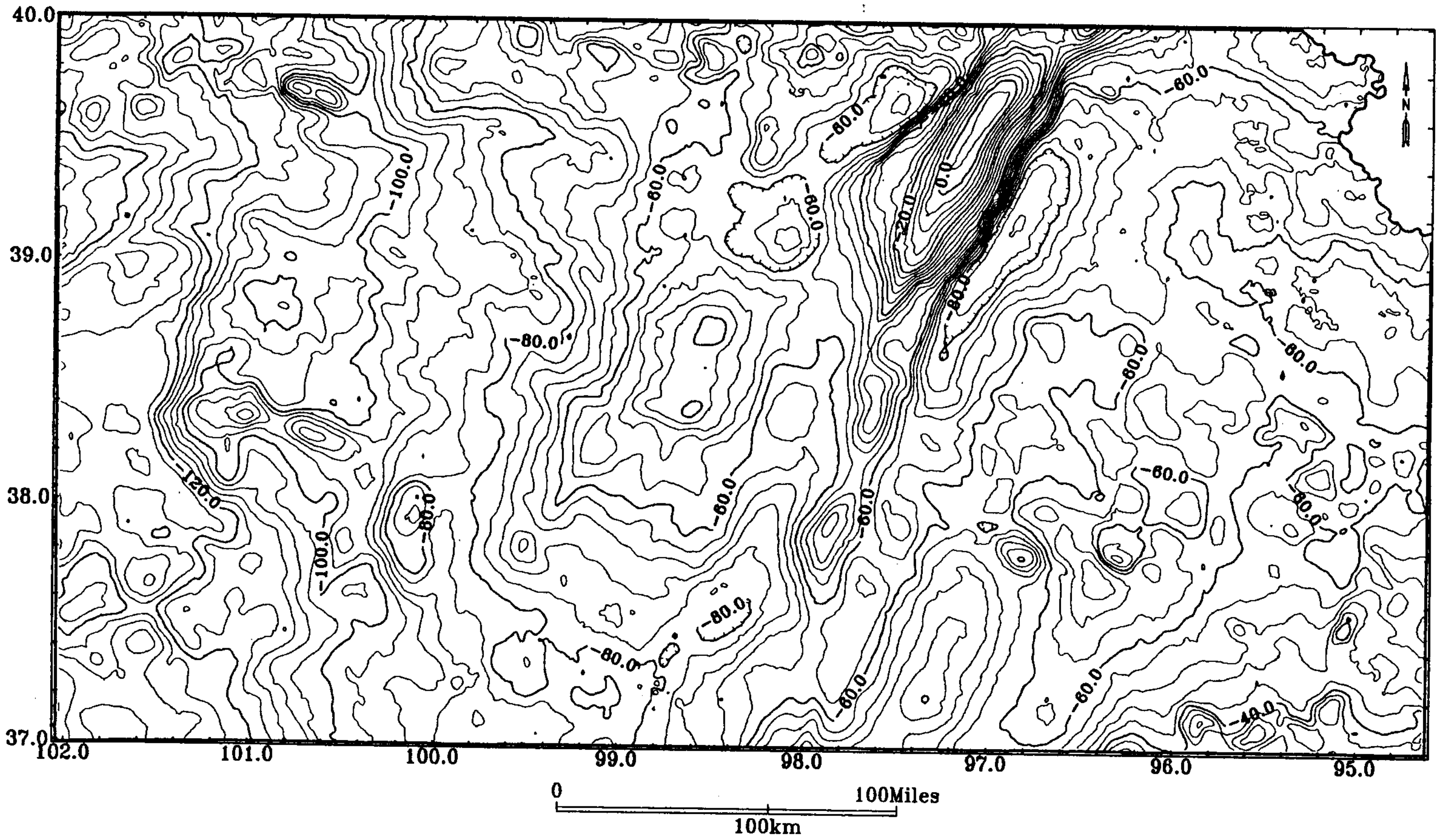

Figure 2-1. The Bouguer gravity anomaly of Kansas measured on the topographic surface. Contour interval is 4 mGal. Coordinates in x and y directions are longitude and latitude in degrees, respectively.

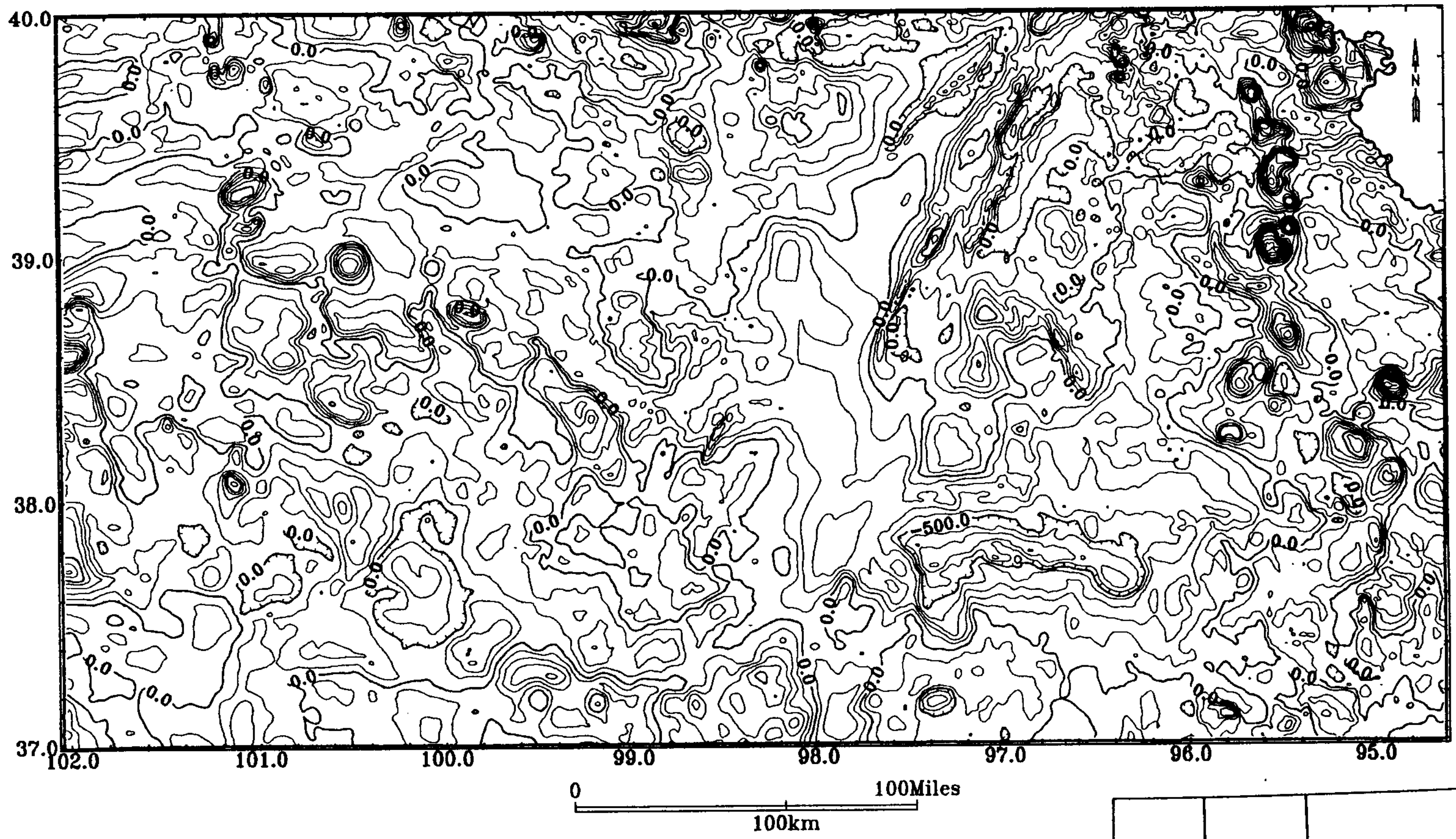

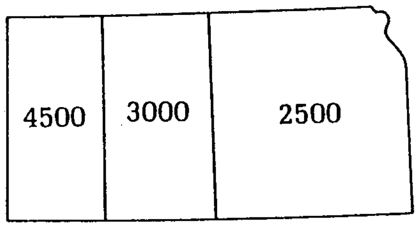

Flight altitude in feet above sea level

Figure 2-2. Aeromagnetic anomaly of Kansas measured at three different elevations. Contour interval is 100 nT. Coordinates in x and y directions are longitude and latitude in degrees, respectively.

2.3. Topographic Correction for Gravity Data in the Spatial Domain

It is well known that topographic relief on the measurement surface distorts the gravity anomaly relative to that which would be measured on a planar surface. This distortion is due to the varying vertical separation of the measurement points from the source body and is not accounted for by the standard Bouguer and Free-air corrections. Tsuboi (1965) calls such anomalies "station" Bouguer anomalies reduced to sea level and distinguishes them from real Bouguer anomalies at sea level. The latter involves a vertical (upward and/or downward) continuation of the gravity field onto a common horizontal plane, which I call topographic correction. Figure 2-3 gives a simple example. Figure 2-3c diagrams a point-mass model. Figure 2-3b shows a cross-section, with a station spacing of 100 m, through a point-mass gravity source buried 100 m directly beneath a 100 m vertical scarp at the surface. The source has an excess mass of 10^{10} kg. Figure 2-3a plots the expected anomaly if measurements were taken on a horizontal datum 200 m above the source ($z = -100$ m) as well as the "measured" anomaly at the topographic surface, after "normal" data corrections to a common datum have been performed. The distortion in the measured anomaly is due to the small vertical separation between the source body and the lower measuring stations.

Several methods of correcting the topographic distortion have been developed. Dampney (1969) determined an equivalent source of discrete point masses on a horizontal plane from Bouguer anomaly measurements on an irregular surface by solving a system of simultaneous equations. He found that the depth to equivalent source should be limited within a certain range relative to the station spacing as indicated by the condition number of the matrix of the system. Henderson and Cordell (1971) discussed an approach of topographic correction by means of finite harmonic series. Syberg (1972) developed simple convolution operators for upward continuation of potential field data from a general surface to a horizontal plane. Bhattacharyya and Chan (1977) determined an equivalent source by solving a Fredholm integral equation of the second kind.

I present an alternative correction which is effective and efficient enough to be incorporated into a routine processing stream when the size of data set is around several

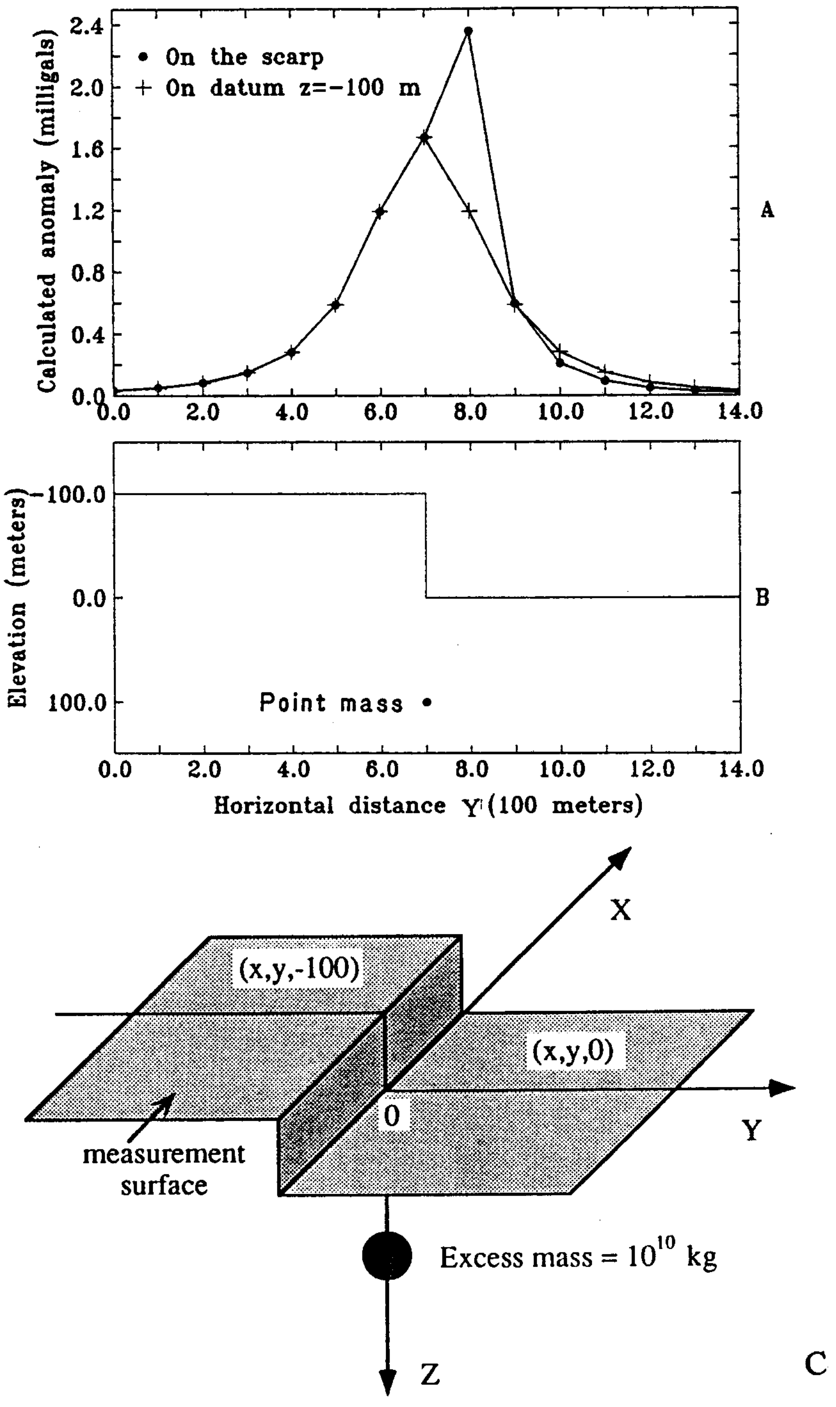

Figure 2-3. A vertical cross-section through a point-mass gravity source buried 100 m directly beneath a 100 m vertical scarp at the surface (b) and the Bouguer anomalies on the scarp and on the horizontal datum 200 m above the source (z = -100 m) (a). (c) is the point-mass gravity model.

thousands. The corrected anomaly is calculated from an ensemble of point-mass equivalent sources derived from the iterative solution of the Dirichlet boundary-value problem. The optimum depth to the source ensemble is that which maximizes the smoothness of the calculated anomaly between the data points.

2.3.1. The method

I seek the gravity function, U, in the region $z \leq f(x,y)$ (z is positive downward), such that

$$\frac{\partial^2 U}{\partial x^2}+\frac{\partial^2 U}{\partial y^2}+\frac{\partial^2 U}{\partial z^2}=0,$$
$$U\big|_{z=f(x,y)}=g(x,y), \tag{2.1}$$

where $f(x,y)$ is the topographic function and $g(x,y)$ is the measured gravity anomaly. With discrete functions $f(x,y)$ and $g(x,y)$, I am given a Dirichlet boundary-value problem.

An iterative forward solution for U can be obtained using an equivalent source approximation. The equivalent source is a collection of point masses, one beneath each surface measurement point. There are two primary difficulties with the equivalent source approach, both related to the depth of the source ensemble. If the source depth is too shallow relative to the station spacing, then the anomaly at each station is determined only by the source directly beneath it. The solution converges quickly, but the anomaly tends to disappear or "sag" between the stations, i.e., high-frequency noise (HFN) is introduced. This noise appears when the equivalent source is used to calculate the anomaly on a new surface (the purpose of the operator). High-frequency noise is also introduced if the source ensemble is too deep because positive and negative sources must be combined to correct for anomaly width. Also with sources that are too deep, the solution converges slowly or not at all. The present work demonstrates that an optimum source depth can be determined which minimizes HFN between stations and therefore minimizes noise introduced by the topographic operator.

Figure 2-4 illustrates the HFN problem in two dimensions (2-D). The "measured" anomaly is specified at 11 stations, located at the horizontal distances given by $x = 0.0$ to 10.0 (station spacing: $DX = 1$). The equivalent source ensemble is 11 mass lines (because the problem is 2-D), one beneath each station. The unknowns are the mass per unit length of each mass-line, which are determined by 11 simultaneous equations. Based on their condition numbers, the equations are well posed for the depths to the equivalent source in the region from 0.1 DX to 10 DX. Therefore, the unknowns can be solved exactly, ie., the difference between the "measured" anomaly and the anomaly caused by the equivalent source can be made arbitrarily small for depths of the equivalent source in the region $0.1DX$ to 10 DX. HFN due to inappropriate source depth is demonstrated by using the derived equivalent sources to calculate the anomaly at midpoints ($x = 0.5$, 1.5, etc.). Figure 2-4 shows the disappearance of the anomaly at intermediate points when the source depth is very shallow ($H = 0.1\ DX$) and also shows distortion of the anomaly when the source depth is too deep ($H = 10.0\ DX$). Figure 2-4 also demonstrates the existence of an optimum source depth that minimizes midpoint HFN. This is contrary to intuition which suggests that the optimum source depth is the maximum depth for which convergence can be realized.

To determine the optimum depth for the equivalent source, I quantitatively estimate the degree of smoothness with Equation (2.2).

$$S(H) = \sqrt{\frac{1}{n}\sum_{i=1}^{n}(\overline{g}_{i,i+1} - g_{i+0.5})^2} \quad , \tag{2.2}$$

where S is our estimate of smoothness, H is the depth to the equivalent source, n is the number of midpoint calculation points, $\overline{g}_{i,i+1}$ is the average of the anomaly values calculated at stations i and $i+1$, and $g_{i+0.5}$ is the calculated gravity from the equivalent source at the midpoint between i and $i+1$. This is a valid estimator as long as the average curvature of the anomaly between the points i and $i+1$ is roughly zero. A more rigorous treatment would use a higher order of polynomial interpolation function. $S(H)$ is calculated for the equivalent source ensemble as H is increased from some small value (e.g., $0.5DX$). The optimum depth, H_j, is that which satisfies the inequality:

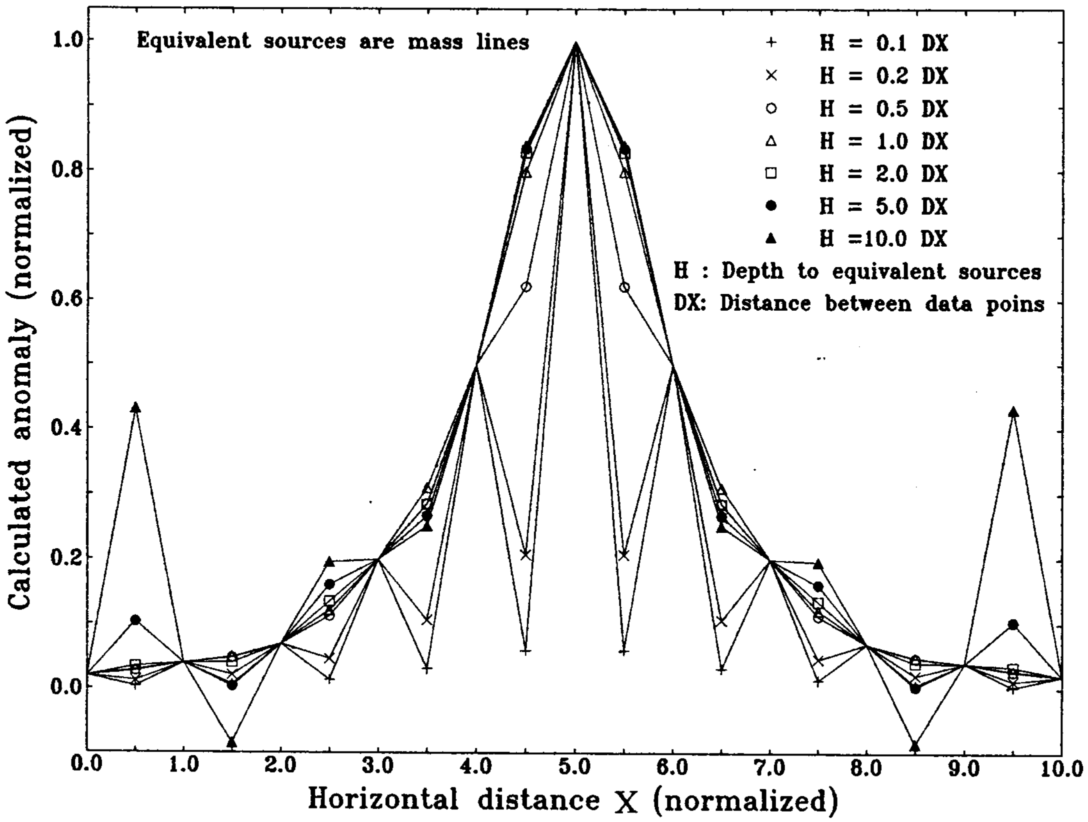

Figure 2-4. High frequency noise (HFN) of intermediate point anomalies as a function of depth of the equivalent source. Intermediate point anomalies are inaccurate both for source depths that are too shallow and too deep.

$S(H_{j-1}) > S(H_j) < S(H_{j+1})$. Figure 2-4 suggests that the optimum depth is in the neighborhood of $H = DX$.

The appropriate mass distribution for the equivalent source at a given depth is determined by iteratively reducing the misfit between the measured anomaly and the calculated anomaly at the measurement stations. The initial estimate of the mass distribution is given by the Gauss formula (e.g., Garland, 1979, p. 136),

$$M_i^0 = g_i \times DS / 2\pi G \quad , \tag{2.3}$$

where M_i^0 is the initial value of the mass of the ith source element, g_i is the anomaly at the ith station, G is the gravitational constant, and DS is the average area between data points. Forward calculations are performed to determined the E_{RMS} error in the equivalent gravity field relative to $g(x,y)$ by

$$E_{RMS} = \sqrt{\frac{1}{m}\sum_{i=1}^{m}(g_i^k - g_i)^2} \quad , \tag{2.4}$$

where m is the total number of data points, g_i^k is the value of the equivalent gravity field at the ith point after the kth iteration, and g_i is the measured gravity at the ith point. Iterative reduction in the E_{RMS} error is then obtained by adjusting the mass distribution. The ith point mass at the $(k+1)$th iteration is given by:

$$M_i^{k+1} = M_i^k + C(g_i - g_i^k)H^2 / G \quad , \tag{2.5}$$

where H is the depth to equivalent source, and C is a coefficient that is chosen in the range from 0.1 to 1 to produce convergence. Equation (2.5) is derived from the differential formula of the gravity field of a point mass. Initially, C is set to 1 which gives the maximum modification to the equivalent source. If this value of C does not produce reduction in E_{RMS} error, then C is repeatedly halved until iterative reduction in E_{RMS} error is achieved. Iteration with the appropriate C value continues until the E_{RMS} error in the equivalent field is less than or equal to the precision of the gravity data. The gravity anomaly of a point source satisfies Laplace's equation, thus the solution obtained above satisfies all conditions of the Dirichlet boundary-value problem.

2.3.2. Testing with synthetic and real data

Table 2-1 lists the results of topographic corrections to the gravity fields of eight buried rectangular slabs with a unit density and having the same horizontal boundaries, $x_1 = 1000$ m, $x_2 = 1800$ m, $y_1 = 600$ m, $y_2 = 1200$ m. The depth to top and bottom (z_1 and z_2, respectively) of the slabs is varied as given in Table 2-1. The "measured" anomaly is calculated at $z = 0$ m while the true anomaly is calculated at $z = -50$ m. The equivalent source is then used to continue the measured anomaly to $z = -50$ m where the misfit with the exact solution is evaluated. The station grid is 15 × 15 with a station spacing of 200 m in both x and y directions. The error between the true anomaly and the corrected anomaly is the true error and is calculated with

$$E_T = \sqrt{\frac{1}{m}\sum_{i=1}^{m}(ge_i - gc_i)^2} \quad , \tag{2.6}$$

where ge_i and gc_i are the true anomaly and the anomaly calculated from the equivalent source on the datum $z = z_0$, respectively. The solution is iterated until E_{RMS} is less than 0.05 mGal. A perfect estimator for S would show minima of S and E_T at the same depth of equivalent source. Table 2-1 indicates that this is only approximately true for the estimator used here. Even so, the value of E_T (Table 2-1, column 5) at minimum S is very close to E_{RMS}, indicating that very little noise is introduced into the continuation when the equivalent source at $H(S_{\min})$ is used. This approach to the topographic correction is thus stable and reliable. For upward continuation, E_T (Table 2-1, column 5) continues to decrease with increase in equivalent source depth beyond the depth of minimum S. This is expected because upward continuation reduces the HFN introduced by using a source that is too deep (Figure 2-4). Downward continuation of the equivalent source results demonstrates (Table 2-1, column 7) the expected correspondence between the depth of minimum S and the depth of minimum E_T (Table 2-1, column 7).

Table 2-1. Testing the approach of the topographic correction in the spatial domain.

z_1/z_2 (m)	H (m)	k	E_{RMS}	E_T (z =- 50 m)	S	E_T (z = 10 m)
50/2000	100	17	0.0413	0.5704	0.8654	0.2796
	200	8	0.0483	0.0644	0.0564	0.0469
	400	59	0.0495	0.0349	0.0743	0.0531
100/2000	100	17	0.0389	0.5226	0.7874	0.2511
	200	7	0.0481	0.0608	0.0510	0.0475
	400	36	0.0488	0.0346	0.0605	0.0526
200/2000	100	16	0.0466	0.3921	0.6100	0.2829
	200	6	0.0420	0.0547	0.0421	0.0415
	400	21	0.0490	0.0380	0.0472	0.0520
400/2000	100	15	0.0453	0.3510	0.5016	0.1329
	200	5	0.0338	0.0473	0.0320	0.0333
	400	12	0.0476	0.0399	0.0394	0.0497
	800	22	0.0485	0.0402	0.0513	0.0505
600/2000	100	14	0.0456	0.2114	0.3198	0.1822
	200	4	0.0390	0.0492	0.0363	0.0380
	400	9	0.0416	0.0371	0.0352	0.0429
	800	19	0.0477	0.0470	0.0450	0.0480
50/1000	100	15	0.0489	0.4566	0.7052	0.2183
	200	8	0.0474	0.0537	0.0528	0.0456
	400	57	0.0497	0.0338	0.0727	0.0533
10/100	100	8	0.0468	0.0999	0.1605	* 0.0695
	200	7	0.0435	0.0449	0.0337	0.0422
	400	44	0.0492	0.0384	0.0373	0.0502
20/500	100	14	0.0412	0.3212	0.5267	0.2338
	200	9	0.0446	0.0531	0.0520	0.0413
	400	81	0.0498	0.0366	0.0773	0.0525

Note: z_1 and z_2 are the depths to the top and the bottom of the rectangular slabs, respectively; H is the depth to the equivalent source; k is the number of iterations; the definitions of S, E_{RMS} and E_T are shown in Equations 2, 4 and 6, respectively; z is the elevation of the corrected datum.

** The datum z in this case is equal to 5 m.*

The technique is applied to the step topography problem of Figure 2-3. The grid is 15 × 15 points with a station spacing of 100 m in both x and y directions. Table 2-2 lists the result. Figure 2-5 plots the anomaly after topographic correction, which is calculated from the ensemble of equivalent sources located at the optimum depth (H = 100 m). Figure 2-6 shows the anomaly which is calculated from the ensemble of equivalent sources located at the depth 12.5 m. Clearly, the distortions in the anomaly still remain in the latter case even though E_{RMS} is equal to 0.02 mGal.

Table 2-2. The topographic correction of the point source problem.

H (m)	k	E_{RMS}	E_T (z = -100 m)	S
12.5	86	0.0200	0.0726	0.1380
50	9	0.0183	0.0257	0.0459
100	20	0.0239	0.0244	0.0299
200	20	0.0541	0.0426	0.0441

I now topographically correct the gravity of McPherson County, Kansas, shown after removal of a second order regional trend in Figure 2-7. The data are gridded to 1.6 km by 1.6 km (1 mi by 1 mi) by SURFACE III (Sampson, 1988), giving a total of 1,156 grid points. Total relief in McPherson County is 120 m (410 ft), as plotted in Figure 2-8. The selected horizontal datum is 500 m above sea level (z = -500 m). Table 2-3 shows the values of smoothness S as a function of depth to

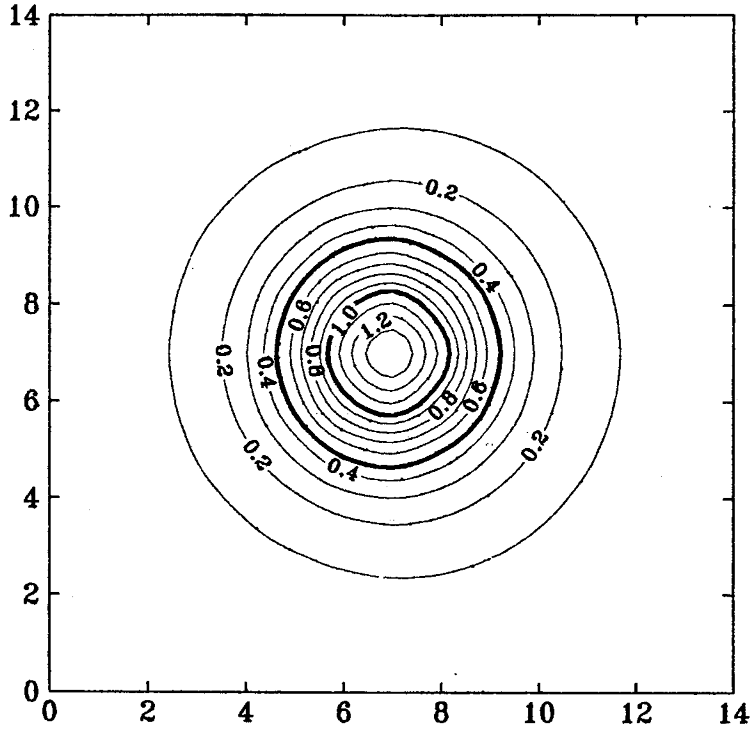

Figure 2-5. Anomaly on the horizontal datum $z = -100$ m caused by an ensemble of point-mass equivalent sources which are located at a depth of 100 m. E_{RMS} (the error between the "measured" anomaly on the scarp and the anomaly caused by the equivalent source on the same surface) is 0.0239 mGal. S (smoothness between the data points) is 0.0299 mGal. E_T (the actual error in the corrected gravity at the datum) is 0.0244 mGal. The topographic correction is visually satisfying. The unit in both x and y directions is a station spacing, 100 m.

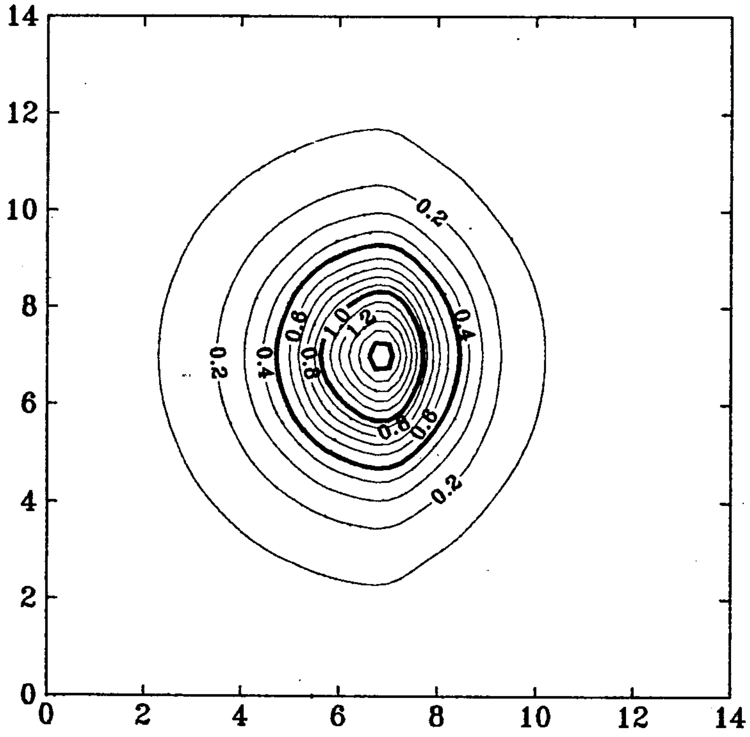

Figure 2-6. Anomaly on the horizontal datum z = -100 m caused by the ensemble of point-mass equivalent sources which are located at a depth of 12.5 m. E_{RMS} is equal to 0.02 mGal, essentially the same as for Figure 2-5. S is equal to 0.1380 mGal, much larger than in Figure 2-5. E_T is 0.0726 mGal. The unit in both x and y directions is a station spacing, 100 m.

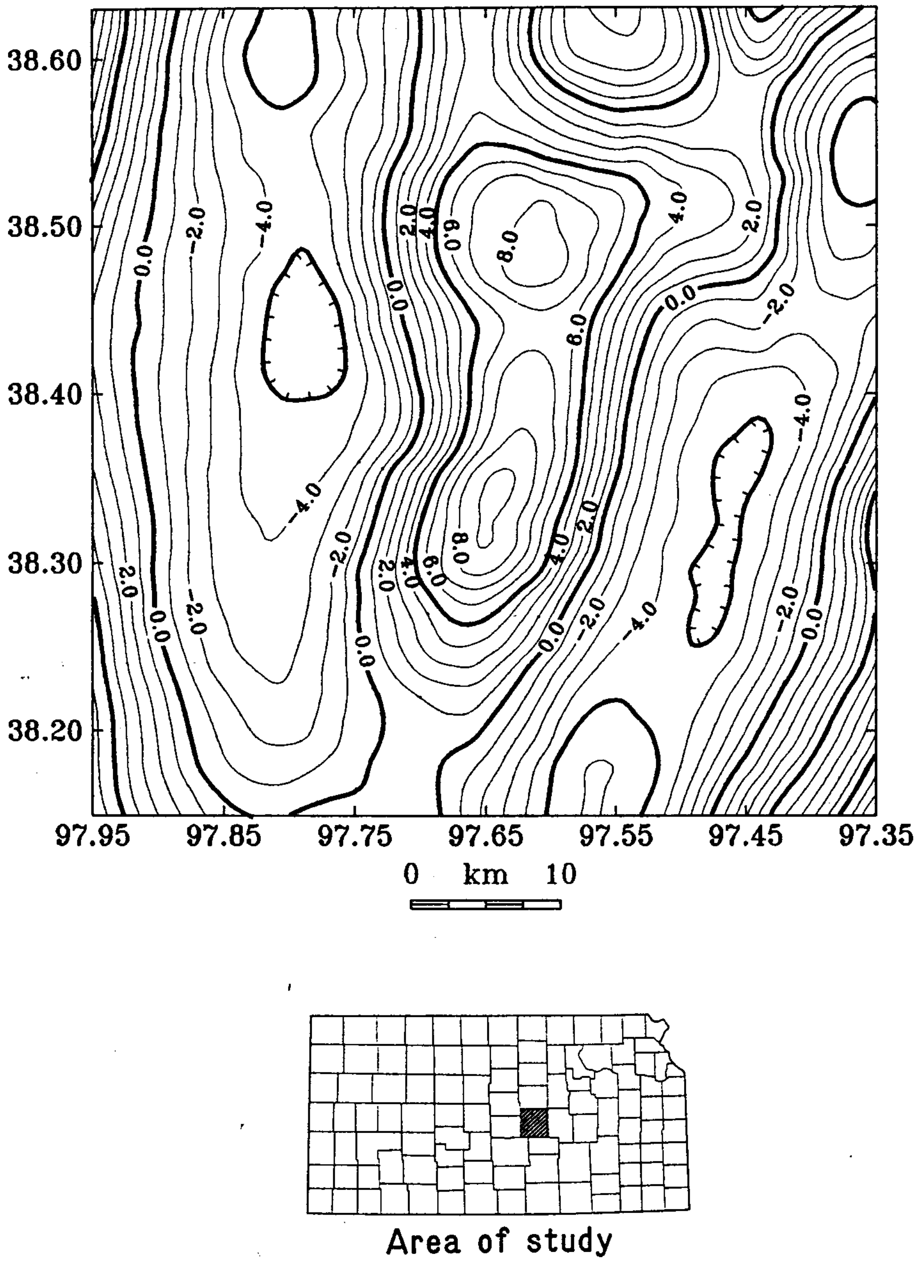

Figure 2-7. Residual Bouguer anomaly of McPherson County, Kansas, after removal of a second order trend. Contour interval is 1 mGal. Coordinates in *x* and *y* directions are longitude and latitude in degrees, respectively.

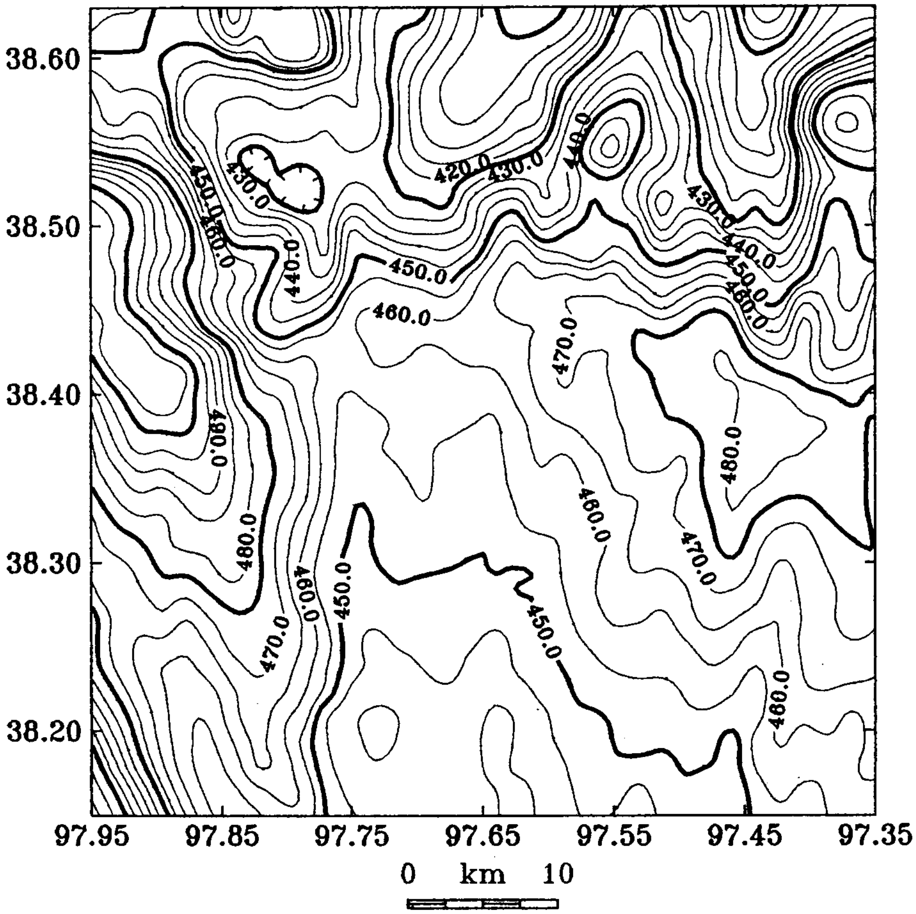

Figure 2-8. The topographic map of McPherson, Kansas. The contour interval is 5 m. Coordinates in x and y directions are longitude and latitude in degrees, respectively.

equivalent source H, which indicate that the optimum depth to the equivalent source is 2,400 m (1.5 DX). Figure 2-9 gives the anomaly after the topographic correction. E_{RMS} is less than 0.1 mGal, the precision of Bouguer anomaly, after 10 iterations. Although E_{RMS} is equal to 0.06 mGal in Table 2-3 when H = 800 m after 7 iterations, Figure 2-10 indicates a poor topographic correction with H = 800 m. Minimization of S rather than E_{RMS} defines the optimum source depth.

Table 2-3. The topographic correction of gravity data in McPherson, Kansas.

H (m)	k	E_{RMS}	E_T (z = -500 m)	S
804.5	7	0.0598	N/A	3.1573
1609.0	5	0.0684		0.2387
2413.5	10	0.0958		0.1106
3218.0	15	0.2207		0.1429

2.3.3. Discussion

The numerical results in Table 2-1 show that the number of iterations required for convergence increases significantly as the equivalent source becomes too deep. Conversely, few iterations are required when the equivalent source is at the optimum depth. Thus, slow convergence of the E_{RMS} (single-step $\Delta E_{RMS} \approx 1$ percent of the last E_{RMS}) is an indication that the equivalent source is too deep.

The minimization of HFN input to the data by optimization of equivalent source depth permits reasonable downward continuation. Thus, the corrected datum could be chosen at the average elevation of a measurement surface rather than at the highest point. It should be pointed out that the optimum depth to equivalent source is

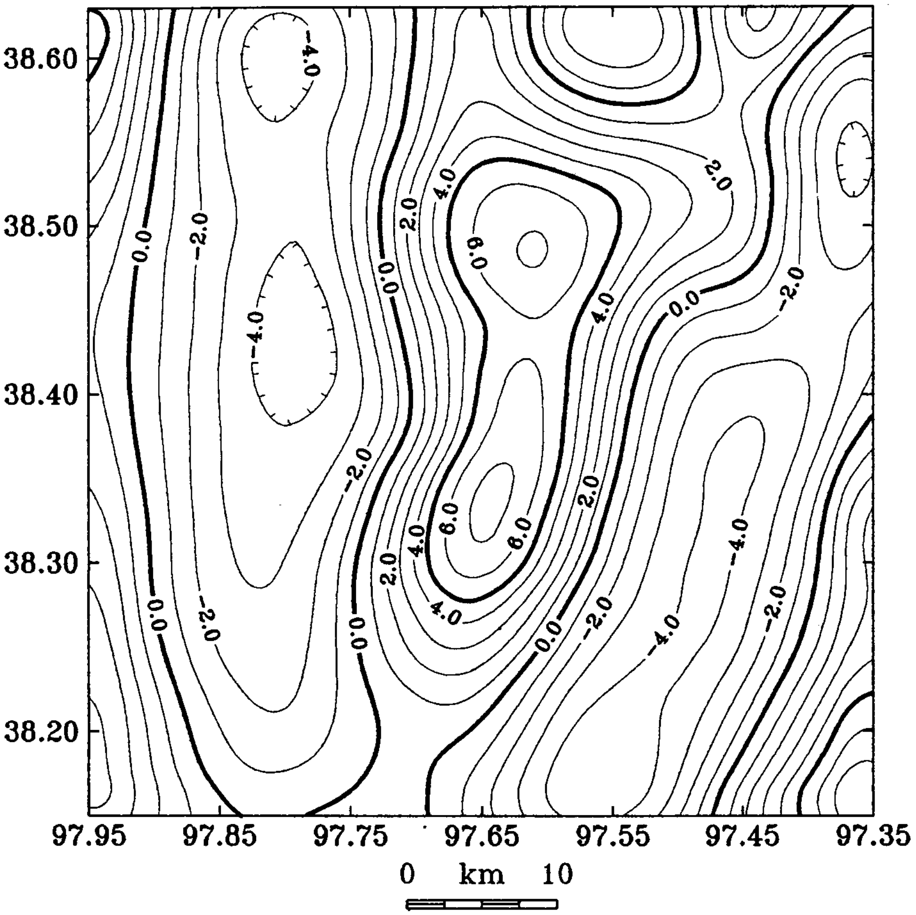

Figure 2-9. Topographically corrected anomaly on the horizontal datum z = -500 m, calculated from the equivalent source which is located at a depth of 2,400 m. E_{RMS} is 0.0958 mGal. S is 0.1106 mGal. Coordinates in x and y directions are longitude and latitude in degrees, respectively.

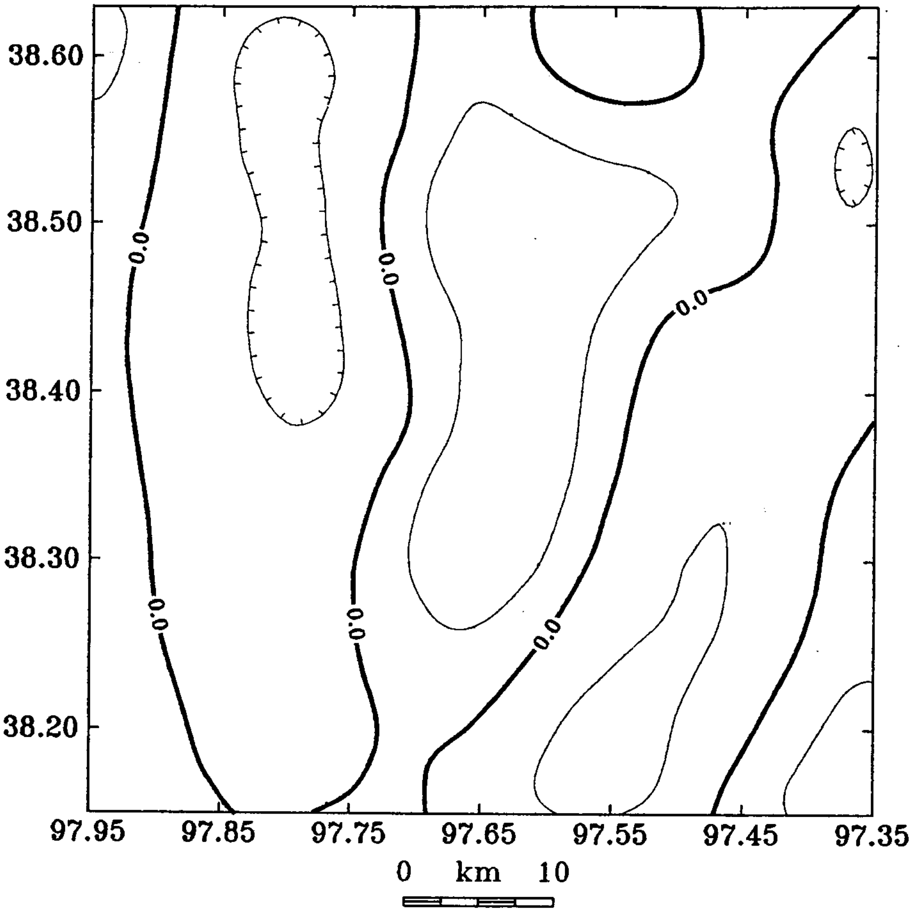

Figure 2-10. Anomaly calculated from an equivalent source located at a depth of 800 m. E_{RMS} is 0.0598 mGal. S is 3.1573 mGal. The correction is clearly inappropriate, as suggested by the non-minimum value of S. Coordinates in x and y directions are longitude and latitude in degrees, respectively.

dependent on the type of the equivalent source. In the next section, I will show that the error caused by the depth to equivalent source discussed here will not occur for an equivalent source covered on a plane continuously.

For larger data sets, calculation of the optimum depth to the equivalent source can be prohibitive. Considerable time savings can be realized by using Taylor series to calculate approximate anomalies and by neglecting the contributions of sources that are very distant from the point of measurement. At horizontal distance ten times the depth, the gravity contribution is only 0.1 percent. Care must be taken in this regard, however, because the topographic corrections are also small relative to the total gravity. In the next section, I will develop a method for calculating topographic correction in the wavenumber domain which is efficient enough to be applicable to large data sets.

2.4. Topographic Correction for Potential-field Data in the Wavenumber Domain

Two methods developed in the wavenumber domain have been proposed by previous workers in order to handle large sets of data. Syberg (1972) developed continuation operators for translating potential-field data from one general surface to another utilizing 2-D integrals in the wavenumber domain. Pilkington and Urquhart (1990) determined an equivalent source on a mirror image of the observation surface. When the mirror image surface is replaced by a horizontal plane, the anomaly caused by the equivalent source on the horizontal plane approximates the corrected anomaly on the corrected datum. The numerical stability of Syberg's operator has not been demonstrated, and the approach proposed by Pilkington and Urquhart is an approximate method.

In this section I present a fast and accurate method for determining an equivalent source for a large set of data measured on a topographic surface. Reduction to a horizontal plane is then straight-forward. The approach is tested using two synthetic examples. This section ends with application of this approach to potential-field data in Kansas. The accuracy of the Fourier-based approach is demonstrated by the two synthetic examples and the efficiency of the approach is shown by application to the gravity and aeromagnetic grids for Kansas.

2.4.1. The method

I define

$$f(\vec{k}) = F[f(\vec{r})] \text{ and } f(\vec{r}) = F^{-1}[f(\vec{k})],$$

where F and F^{-1} are Fourier transform and inverse Fourier transform of function f, respectively. Considering the case in Figure 2-11, let $\sigma(\vec{k})$ be an equivalent density on a given horizontal plane E, where $\vec{k}\,(= k_x\vec{e}_x + k_y\vec{e}_y)$ is the wave vector, and $\vec{e}_x$ and $\vec{e}_y$ are the unit vectors in x and y directions, respectively, I want to calculate a gravity anomaly on the observation surface S. The anomaly $\bar{g}(\vec{k})$ on the plane E can be written as

$$\bar{g}(\vec{k}) = 2\pi G\sigma(\vec{k}), \tag{2.7}$$

where G is gravitational constant. To apply upward continuation to $\bar{g}(\vec{k})$, I obtain the gravity anomaly on the observation surface S, $g(\vec{k})$

$$g(\vec{k}) = \bar{g}(\vec{k})e^{-|\vec{k}|z(\vec{r})}, \tag{2.8}$$

where $Z(\vec{r})$ is the vertical distance from observation surface S to the plane E, (see Figure 2-11), and $\vec{r}\,(= x\vec{e}_x + y\vec{e}_y)$ is the vector of coordinates on the x-y plane.

If $Z(\vec{r})$ is constant, Equation (2.8) is a well-known upward continuation expression in the wavenumber domain. I will show that when $Z(\vec{r})$ is not constant, Equation (2.8) can still be used to calculate $g(\vec{k})$ on the observation surface S, if the anomaly $\bar{g}(\vec{k})$ on the horizontal plane E can be determined.

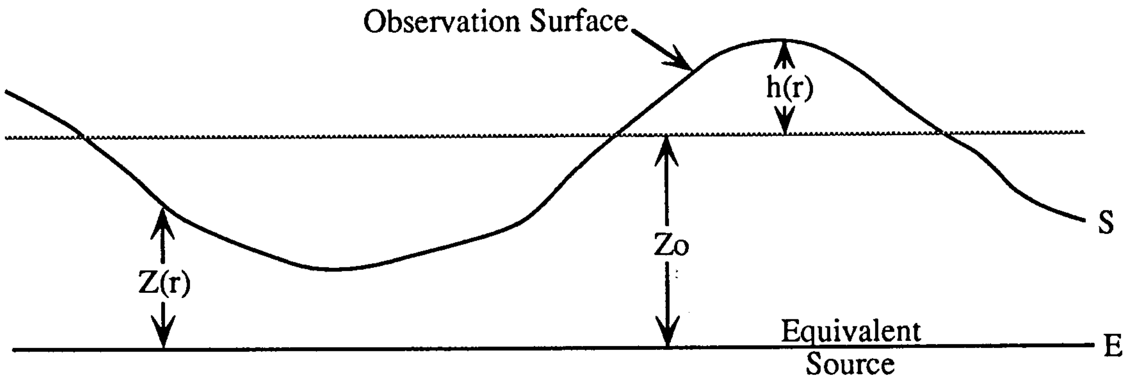

Figure 2-11. Geometry of the plane of the equivalent source *E* and the observation surface *S*.

Let Z_0 be the median distance from the surface $Z(\vec{r})$ to the plane *E*, then

$$Z(\vec{r}) = Z_0 + h(\vec{r}),$$

where $h(\vec{r})$ is the topographic change relative to Z_0 (see Figure 2-11). Equation (2.8) can be written as

$$g(\vec{k}) = \bar{g}(\vec{k}) e^{-|\vec{k}|Z_0} \left\{ e^{-|\vec{k}|h(\vec{r})} \right\}. \tag{2.9}$$

The exponential term in Equation (2.8) is split up into two exponential terms in Equation (2.9). The first term is a conventional upward continuation operator, and the second term is related to topographic change. I use a Taylor series to express the term in { } and substitute equation (1) for $\bar{g}(\vec{k})$, then Equation (2.9) can be written as

$$g(\vec{k}) = 2\pi G\sigma(\vec{k}) e^{-|\vec{k}|Z_0} \sum_{n=0}^{\infty} \frac{\left[-|\vec{k}|h(\vec{r})\right]^n}{n!} . \tag{2.10}$$

Equation (2.10) is the basis for the reduction technique, and is also mentioned by Parker (1973), Gusip (1987), Pilkington and Urquhart (1990), and Pilkington (1990) in different ways. The problem can then be solved if the series converges. Appendix B gives the proof that the series in Equation (2.10) is uniformly convergent over the entire wavenumber domain and also shows it is independent of the wavenumber $\vec{k}$. The condition is that the plane *E* must be chosen below the observation surface *S* ($Z_0 > H$).

Based on Poisson's relation (e.g., Dobrin, 1976, p. 483), an equation for the magnetic anomaly can be written directly from Equation (4),

$$T(\vec{k}) = 2\pi \frac{(\tilde{k}\cdot\vec{e})(\tilde{k}\cdot\vec{j})}{|\vec{k}|} J(\vec{k}) e^{-|\vec{k}|Z_0} \sum_{n=0}^{\infty} \frac{\left[-|\vec{k}|h(\vec{r})\right]^n}{n!} , \tag{2.11}$$

where "·" is the dot product of two vectors, $\vec{k} = i\left(k_x\vec{e}_x + k_y\vec{e}_y\right) + \sqrt{k_x^2 + k_y^2}\,\vec{e}_z$, $\vec{e}_z$ is the unit vector in the z direction, $\vec{e}$ and $\vec{j}$ are the unit vectors of the Earth's field and the magnetization, respectively, and $i = \sqrt{-1}$ is the imaginary unit.

Equations (2.10) and (2.11) allow us to calculate gravity and magnetic anomalies on a topographic surface caused by a source located on a horizontal plane. I use the equations to determine an equivalent source $\sigma(\vec{r})$ (or $J(\vec{r})$) on the plane E based on measured anomalies on the observation surface S by iterative forward calculations.

1) Initialize $\sigma(\vec{r})$ (or $J(\vec{r})$) and define the depth to the equivalent source;

2) Calculate the modeled gravity (or magnetic) anomaly from $\sigma(\vec{r})$ (or $J(\vec{r})$) by the Equations (4) (or (5));

3) Estimate errors: two errors used to trace the iterative procedure are an rms error *RMS(k)* at the *k*th iteration

$$RMS(k) = \sqrt{\frac{1}{N}\sum_{i=1}^{N}\left(s_i - u_i^k\right)^2} \tag{2.12}$$

and the maximum deviation *MAXD(k)* at the *k*th iteration

$$MAXD(k) = \max_{1 \le i \le N}\left|s_i - u_i^k\right|, \tag{2.13}$$

where superscript k stands for the kth iteration and subscript i for the ith data point; s is the measured anomaly; u is modeled anomaly calculated by Equation (4) (or (5)), and N is the total number of data points. If at any step, neither of these errors are reduced or the *RMS* reaches the accuracy threshold, the iterative procedure is terminated.

4) Modify the $\sigma(\vec{r})$ (or $J(\vec{r})$) based on equation (8), then repeat step 2);

$$\sigma_i^{k+1} = \sigma_i^k + \left(s_i - g_i^k\right)/2\pi G \quad (\text{or } J_i^{k+1} = J_i^k + C\left(s_i - T_i^k\right)), \tag{2.14}$$

where s is measured gravity (or magnetic) anomaly; g and T are calculated by Equations (2.10) and (2.11), respectively; and C is a dimensionless constant, which is chosen to produce convergence. In our experience, C is chosen as 0.1 when J and T are in the same units. These simple equations of modification are effective and efficient.

Once the equivalent source on the plane E is determined, the field on a horizontal plane (corrected datum) above the plane E is the normal upward continuation by Equation (2.8). In this case, function $Z(\vec{r})$ is a constant, which is the vertical distance from the corrected datum to the plane E. The equivalent source can also be used to calculate pseudo-gravity, anomaly migrated to pole, directional derivatives, etc.

2.4.2. Testing by synthetic models

The first example is the same as the synthetic example in section 2.3 (Figure 2-3) from Xia and Sprowl (1991). Figure 2-12a shows the Bouguer anomaly measured on the topographic surface, after "normal" data corrections to a common datum have been performed. Figure 2-12b is the desired anomaly as would be measured on a horizontal datum 200 m above the source (z = -100 m, z is positive downward). The distortion in the measured anomaly is due to the small vertical separation between the source body and the lower measuring stations. The initial equivalent density on the plane $z = 1$ m is set to 0 and the gravity anomaly is calculated at each point on the measurement surface. The initial RMS and $MAXD$ errors are 0.316 mGal and 2.358 mGal. After 11 iterations, the RMS and $MAXD$ errors between the modeled and measured anomalies are reduced to 0.009 mGal and 0.126 mGal, respectively. The modified equivalent source is used to calculate the corrected anomaly on the plane z = -100 m, which is plotted in Figure 2-12c. The RMS error between the corrected anomaly (Figure 2-12c) and the desired anomaly (Figure 2-12b) is 0.012 mGal. The maximum and average values of correction, which are defined as the difference between the measured data (Figure 2-12a) and the corrected data on a given horizontal plane (Figure 2-12c), are 1.203 mGal and 0.059 mGal, respectively. Figure 2-12d shows the difference between Figures 2-12b and 2-12c and demonstrates that the correction of the topographic distortion is very good.

The accuracy of the solution is not significantly dependent on the depth of the equivalent source. To confirm this, I set the equivalent source at different depths

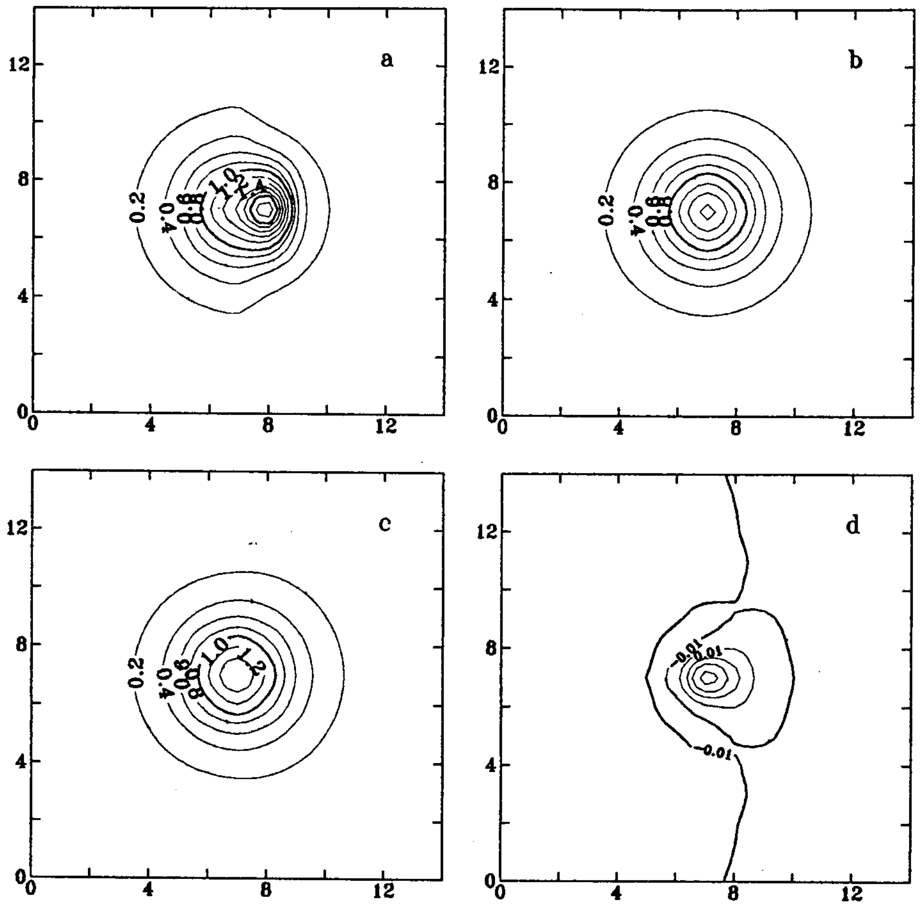

Figure 2-12. Results for the point-mass example. (a) is the Bouguer anomaly on the topographic surface, (b) is the expected anomaly on the plane z = -100 m. (c) is the topographically corrected anomaly on the plane z = -100 m. (d) is the difference between (b) and (c). The unit in both x and y directions is one station spacing, 100 m. Contour interval is 0.2 mGal in (a) - (c), and 0.02 mGal in (d).

from $z = 0.001$ m to 100 m for the example. The results show that the *RMS* error between the corrected and true anomalies on the plane $z = -100$ m is in the region 0.011- 0.012 mGal. However, the number of iterations increases from 7 to 53 with increasing depth to equivalent source from 0.001 m to 100 m.

A second example utilizes a magnetized rectangular solid with inclination = 60 degrees, declination = 30 degrees, and magnetization = 400 nT, buried beneath the scarp of the previous example. The solid is 100 m × 100 m × 100 m, centered in the data area, with its top at a depth of 50 m. The data are a 15 × 15 grid of points, spaced every 100 m (Figure 2-13). Figure 2-14a shows the magnetic anomaly measured on the topographic surface. Figure 2-14b shows the desired anomaly as would be measured on a horizontal plane $z = -50$ m (half way up the scarp). The initial magnetization is set to 0 and the depth to equivalent source is 1 m. The initial *RMS* and *MAXD* errors are 11.618 nT and 76.580 nT, respectively. The *RMS* and *MAXD* errors are reduced to 0.490 nT and 3.246 nT, respectively, after 42 iterations. Figure 2-14c shows the corrected anomaly on the plane $z = -50$ m. The *RMS* error and average deviation between the corrected anomaly (Figure 2-14c) and the desired anomaly (Figure 2-14b) are 2.109 nT and 0.743 nT, respectively. Figure 2-14d plots the difference between Figures 2-14b and 2-14c. If the corrected datum is chosen as $z = -100$ m, the *RMS* error and average deviation between the corrected anomaly and desired anomaly are 0.520 nT and 0.250 nT, respectively.

2.4.3. Application to potential-field data in Kansas

Bouguer Gravity

The original Bouguer anomaly measured on the topographic surface is shown in Figure 2-1. The gridded data set is 205 × 408 points.

The initial equivalent density is 0 and the equivalent source is on a plane $z = -200$ m (660 ft), just below the lowest measurement point. The initial *RMS* and *MAXD* errors are 79.9 mGal and 151.1 mGal, respectively. The *RMS* and *MADX* errors are reduced to 0.1 mGal and 1.7 mGal, respectively, after 2 iterations. In each iteration, the value of the second term in the series of Equation (4) is about 5 percent of

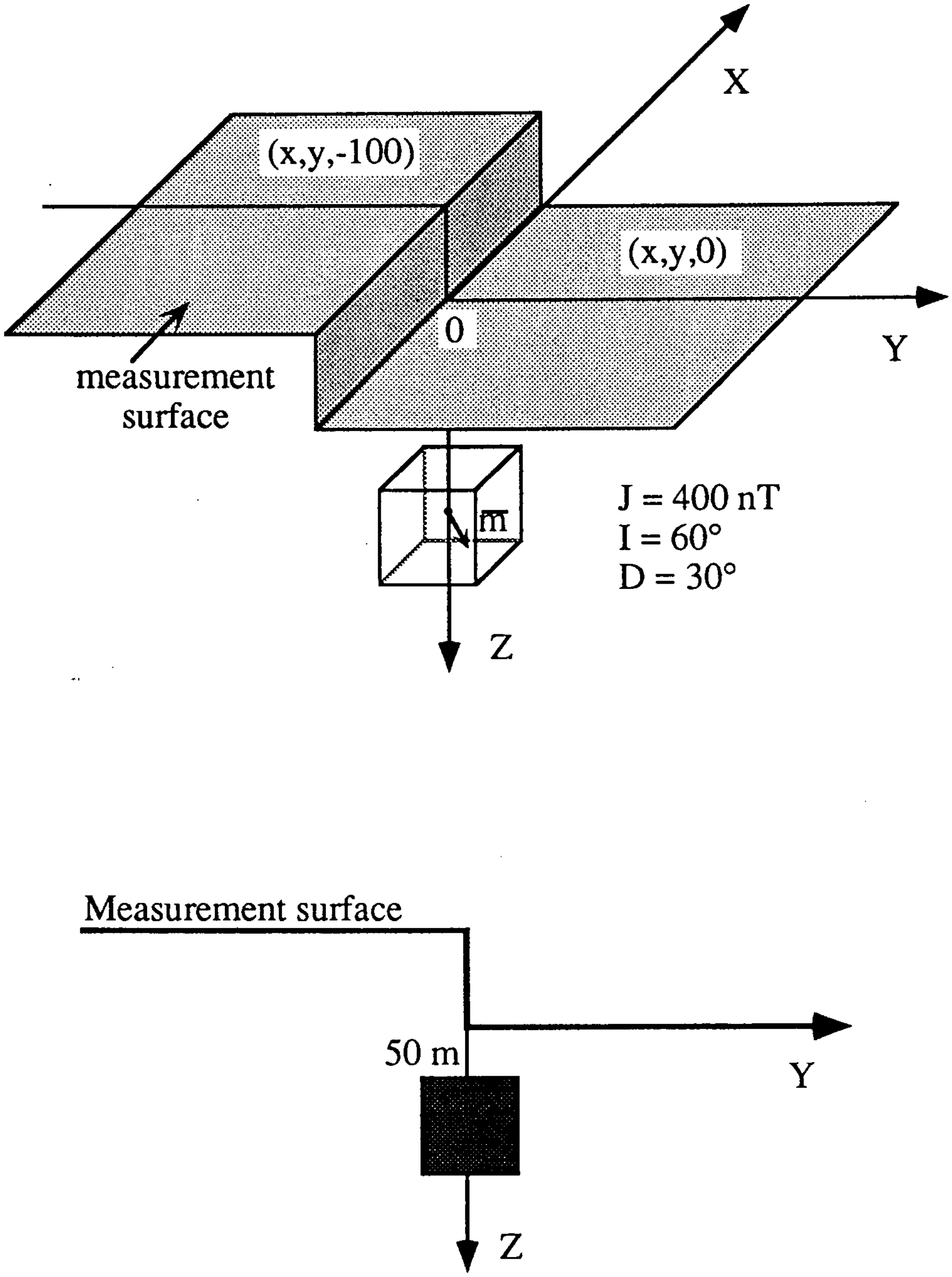

Figure 2-13. Magnetic model: a rectangular solid is buried beneath a 100 m vertical scarp at the surface with inclination = 60 degrees, declination = 30 degrees, and magnetization 400 nT. The solid is a 100 m cube located in the center of the data area and has its top at a depth of 50 m.

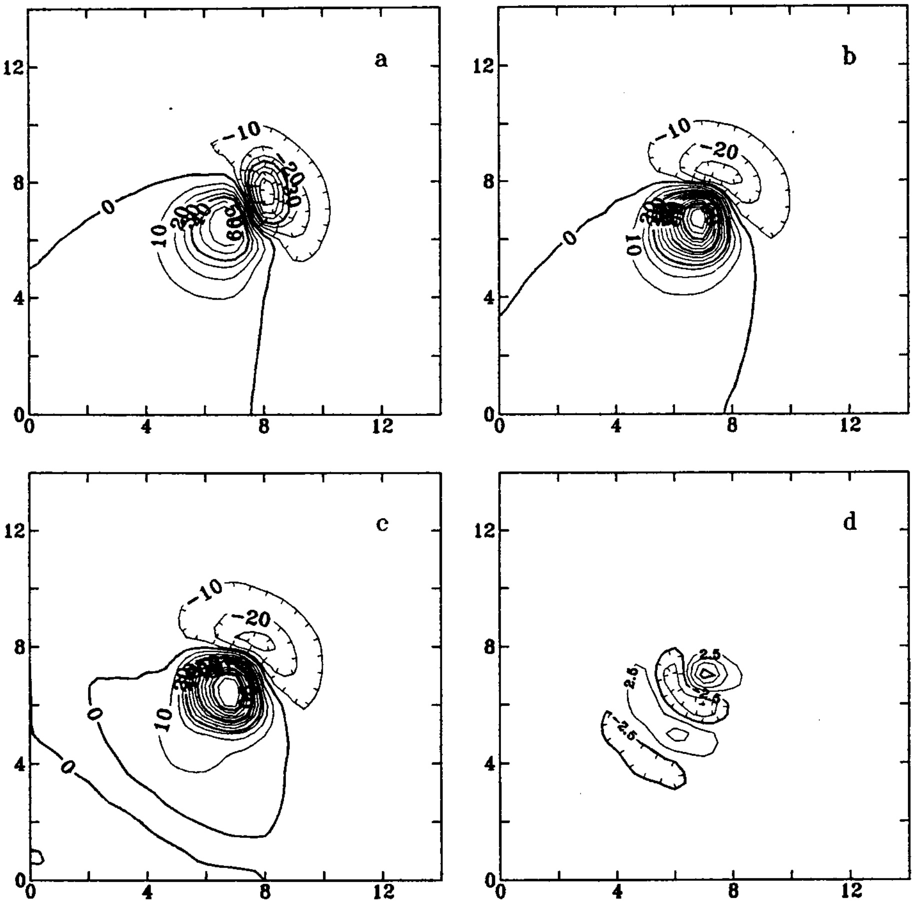

Figure 2-14. Results of the rectangular solid example. (a) is the magnetic anomaly on the measurement surface. (b) is the expected anomaly on the plane z = -50 m. (c) is the topographically corrected anomaly on the plane z = -50 m. (d) is the difference between (b) and (c). The units in both x and y directions is one station spacing, 100 m. Contour interval is 10 nT in (a) - (c), 5 nT in (d).

the first term, indicating very rapid convergence. The same is true in the magnetic case below. I use the equivalent density to calculate the corrected Bouguer anomaly on the plane z = -700 m, which is shown in Figure 2-15. Figure 2-16 plots the magnitude of the correction at each point, which is the difference between the gravity anomaly on the topographic surface (Figure 2-1) and the corrected anomaly (Figure 2-15). In the vicinity of the 100th meridian in western Kansas, the magnitude of correction is close to zero because the measurement surface is close to the datum of calculation. The maximum and average values of correction are 2.55 mGal and 0.18 mGal, respectively. The maximum elevation change in the gravity data is up to 500 m. The calculations took about 4 minutes on a Data General MV 20000.

Aeromagnetic Anomaly

The aeromagnetic anomaly measured on the three different planes is shown in Figure 2-2. The final gridded data set is 205 × 408 points.

The initial equivalent magnetization is 0 and the inclination and declination are chosen as 65 degrees and 7 degrees for both the Earth's field and the magnetization, respectively. The equivalent source is on the plane z = -760 m (760 m above sea level), just below the lowest level of the survey. The initial *RMS* and *MAXD* errors are 190 nT and 1,106 nT, respectively. The *RMS* and *MAXD* errors are reduced to 4 nT and 20 nT, respectively, after 12 iterations. The calculations took about 20 minutes on a Data General MV20000. I used the equivalent magnetization to calculate the corrected anomaly on three different planes, z = -760.0 m, -910 m, and -1,370 m. Table 2-4 shows the variation in correction with datum chosen and indicates the amount of correction increase with amount of vertical distance change. When the corrected datum coincides with the one of measurement levels, the average value of the corrections is approximately the *RMS* error between the modeled and measured anomalies, i.e., no correction is made to the data in this case. Using a datum of 910 m above sea level, the average correction in the western quarter of Kansas is 11 nT, due to downward continuation of 460 m (1,500 ft). Almost no correction is made to the data in the west-central quarter of Kansas, because there is no elevation change in this area. For eastern Kansas, the average correction is 5 nT due to upward continuation of 150 m (500 ft). Figure 2-17 shows the corrected aeromagnetic anomaly on the datum z =

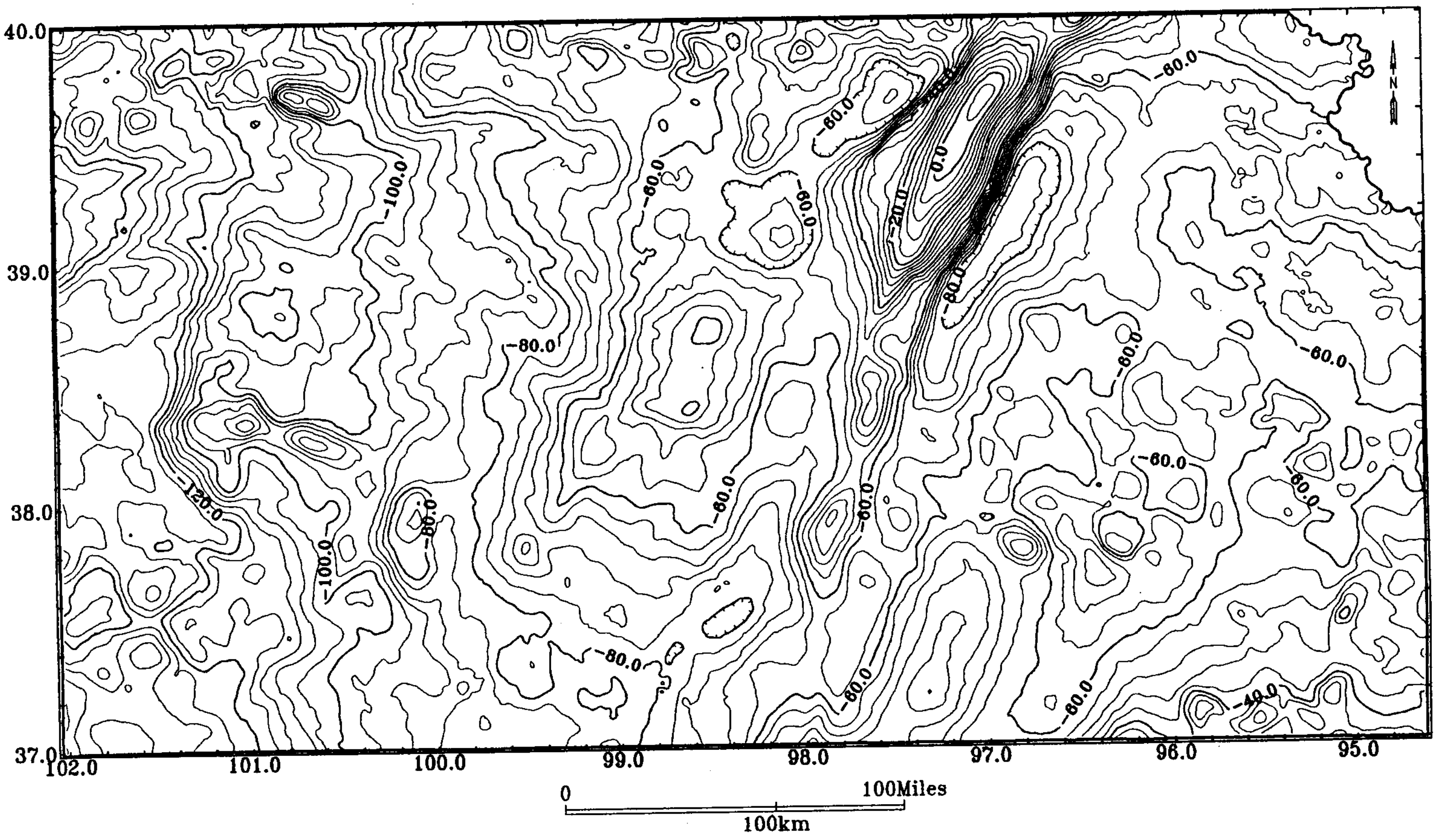

Figure 2-15. The corrected Bouguer gravity of Kansas on the plane 700 m above sea level. Contour interval is 4 mGal. Coordinates in *x* and *y* directions are longitude and latitude in degrees, respectively.

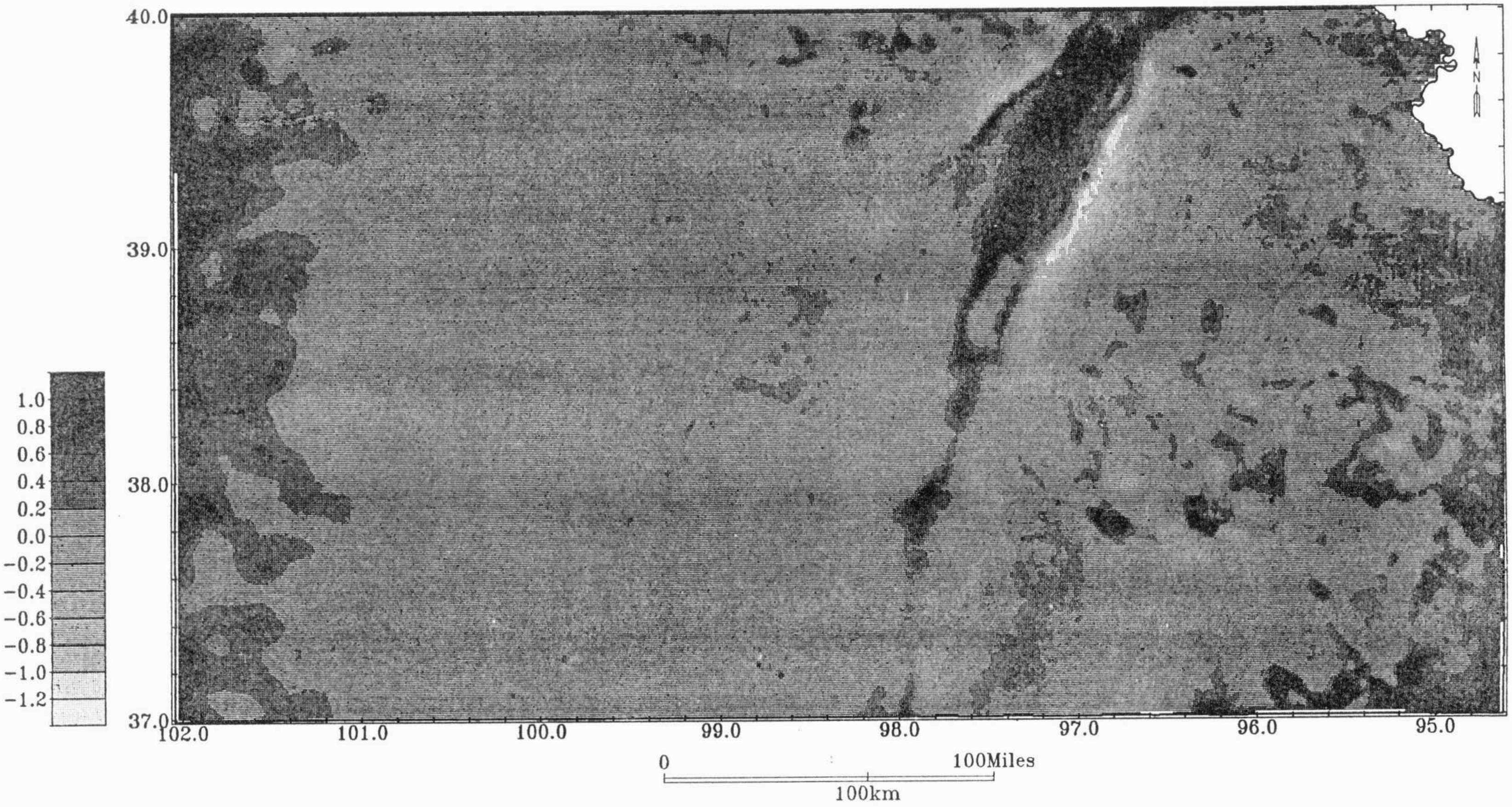

Figure 2-16. Values of the topographic correction in the Bouguer gravity data, which is the difference between the Bouguer gravity on the measurement surface (Figure 2-1) and the corrected anomaly (Figure 2-15). Shading interval is 0.2 mGal. The Coordinates in *x* and *y* directions are longitude and latitude in degrees, respectively.

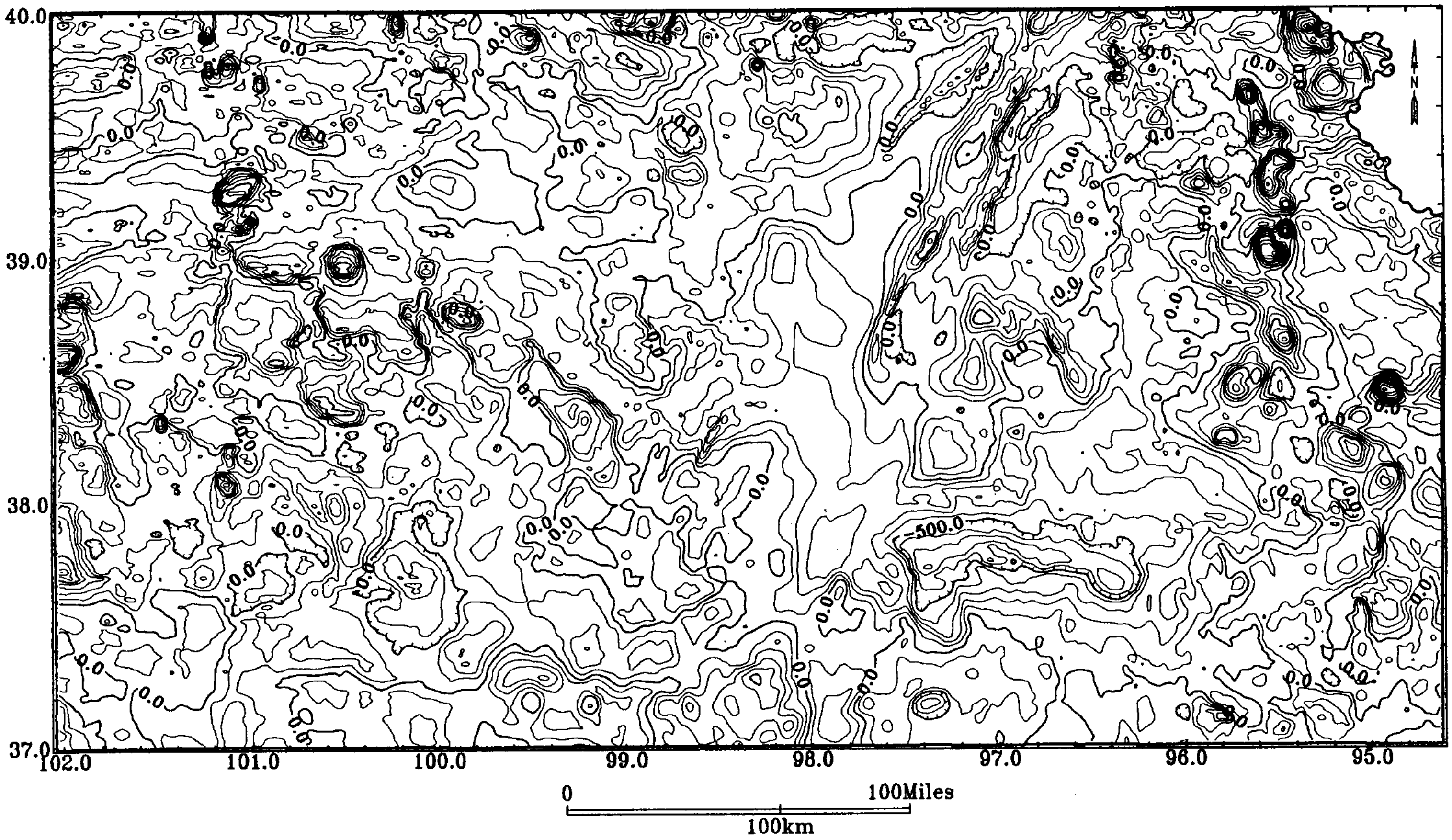

Figure 2-17. Corrected aeromagnetic anomaly of Kansas on the datum 910 m (3,000 ft) above sea level. Contour interval is 100 nT. Coordinates in *x* and *y* directions are longitude and latitude in degrees, respectively.

-910 m (3,000 ft). Figure 2-18 plots values of the correction, which is the difference between the aeromagnetic anomaly on the three different levels (Figure 2-2) and the corrected anomaly (Figure 2-17). The maximum horizontal shifting of aeromagnetic anomalies is 460 m.

Table 2-4. Values of correction of the aeromagnetic data on three parts of Kansas.

Datum (m)	Average values of correction (nT)			Maximum correction (nT)
	Western Kansas		E. Kansas	
	-1,370 m	-910 m	-760 m	
-760	14	5	4	383
-910	11	3	5	270
-1,370	3	10	14	270

2.5. Separation of Potential-field Anomalies

Anomaly separation is the process of separating the potential-field anomaly due to the geological feature of interest from the interfering potential-field effects of other geological features (commonly called regional-residual separation). Theoretically, the separation is impossible because the frequency spectra of the anomalies are broad-band for sources at all depths. In practice, the peak in spectral power is depth dependent so reasonable separations can be made if the geology is “well behaved”.

I assume that the regional field can be expressed as a two-dimensional polynomial of some degree. Extraction of the residual from the measured anomaly can then be done both graphically and computationally. Graphical methods have both the advantage and disadvantage of being subjective (Dobrin and Savit, 1988, p. 603). The fundamental problem with the graphical methods is the limited complexity of regional

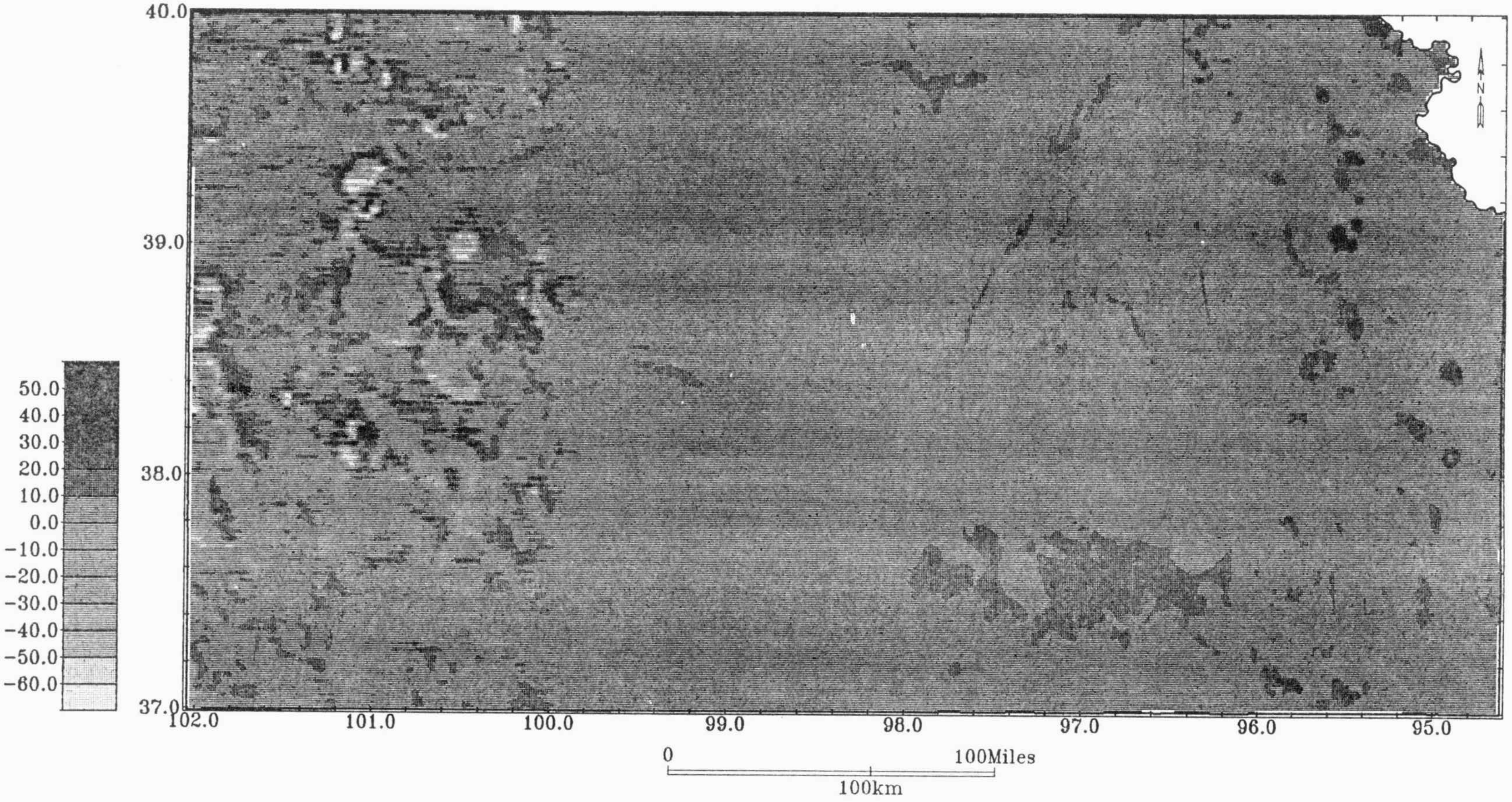

Figure 2-18. Values of the topographic correction in the aeromagnetic data, which is the difference between the aeromagnetic anomaly on the three different levels (Figure 2-2) and the corrected anomaly on the plane 910 m (3,000 ft) above sea level (Figure 2-17). Shading interval is 10 nT. Coordinates in *x* and *y* directions are longitude and latitude in degrees, respectively.

field that the interpreter can reasonably handle. Computational methods are fast, accurate, and objective, but guarantee no correspondence between the chosen regional and the actual regional. The most straight-forward, flexible, and commonly used approach is the polynomial-fitting method. The observed data are fitted, usually by the least-squares method, to the mathematically describable surface (regional surface) that fits most closely with the data within a specified degree of detail. A method to determine the optimum order of a polynomial that fits the regional surface is discussed by Abdelrahman et al. (1985). They studied several synthetic models and derived a useful procedure. The overall similarity between each two successive residual maps is determined by calculating a correlation factor between the mapped variables. The correlation factors are computed using a formula given by Davis (p. 40, Eq. 2.24 and p. 448, 1986). The lower order of two successive residual maps with the maximum value of the correlation factor is the optimum order of the polynomial to fit the regional surface.

If we can assume that anomalous sources are randomly distributed in the subsurface, then we can use Wiener filtering to separate gravity anomalies (Pawlowski and Hansen, 1990). The Wiener filtering is constrained by geologic information. If we assume layered anomalous sources randomly distributed in the subsurface, then anomaly separation can be accomplished through upward continuation (Jacobsen, 1987).

In this study, I use orthogonal-polynomial fitting to determine the regional field and use Abdelrahman et al.'s criterion (1985) to determine the optimum order of the polynomial. The details of orthogonal-polynomial fitting are in Appendix A. I compare the speed of calculations for both the orthogonal-polynomial fitting and the normal polynomial fitting. The result shows that the former is five times faster than the latter. For example, normal polynomial fitting of the magnetic data for all of Kansas from first order to third order took 408 CPU seconds on a Data General MV20000, but only 82 CPU seconds is need for the orthogonal polynomial fitting. The main reason I use the orthogonal-polynomial fitting is its numerical stability, especially when higher order polynomials are needed. It is well known that the normal equations in the least-squares method are usually ill-posed when normal polynomial fitting is used with a large set of data.

To separate the Bouguer gravity anomaly (Figure 2-15), I calculated the correlation factors between the first order and the second order residuals, the second and the third, and the third and fourth, which are 0.5982, 0.9682, and 0.9269, respectively. Therefore, the optimum order of polynomial to fit the regional anomaly is 2. Figure 2-19 is the regional gravity map of the second order orthogonal-polynomial trend and Figure 2-20 is the residual Bouguer anomaly. The pattern of the regional Bouguer anomaly looks very similar to Kane and Godson's result (1985, Figure 2-21). They point out that the short-wavelength (< 250 km) anomaly is mainly caused by the anomalous mass in the crust. For the aeromagnetic anomaly (Figure 2-17), the correlation factors between the first order and the second order residuals, the second and the third, and the third and fourth are 0.9757, 0.9409, and 0.9798, respectively. Because the correlation coefficient of the first and second order residual is very close to that of the third and fourth order, I choose the optimum order of polynomial to fit the regional anomaly is 1. Figure 2-22 is the regional magnetic anomaly of the first order orthogonal-polynomial trend and Figure 2-23 is the residual magnetic anomaly.

2.6. Assumptions about the Separated Anomalies

In the inversions derived in the next two chapters, the following assumptions are made about the separated anomalies:

1) The residual potential-field anomalies are caused by topographic relief and lithologic variation in the Precambrian basement;

2) The regional Bouguer gravity anomaly is caused by the Moho discontinuity.

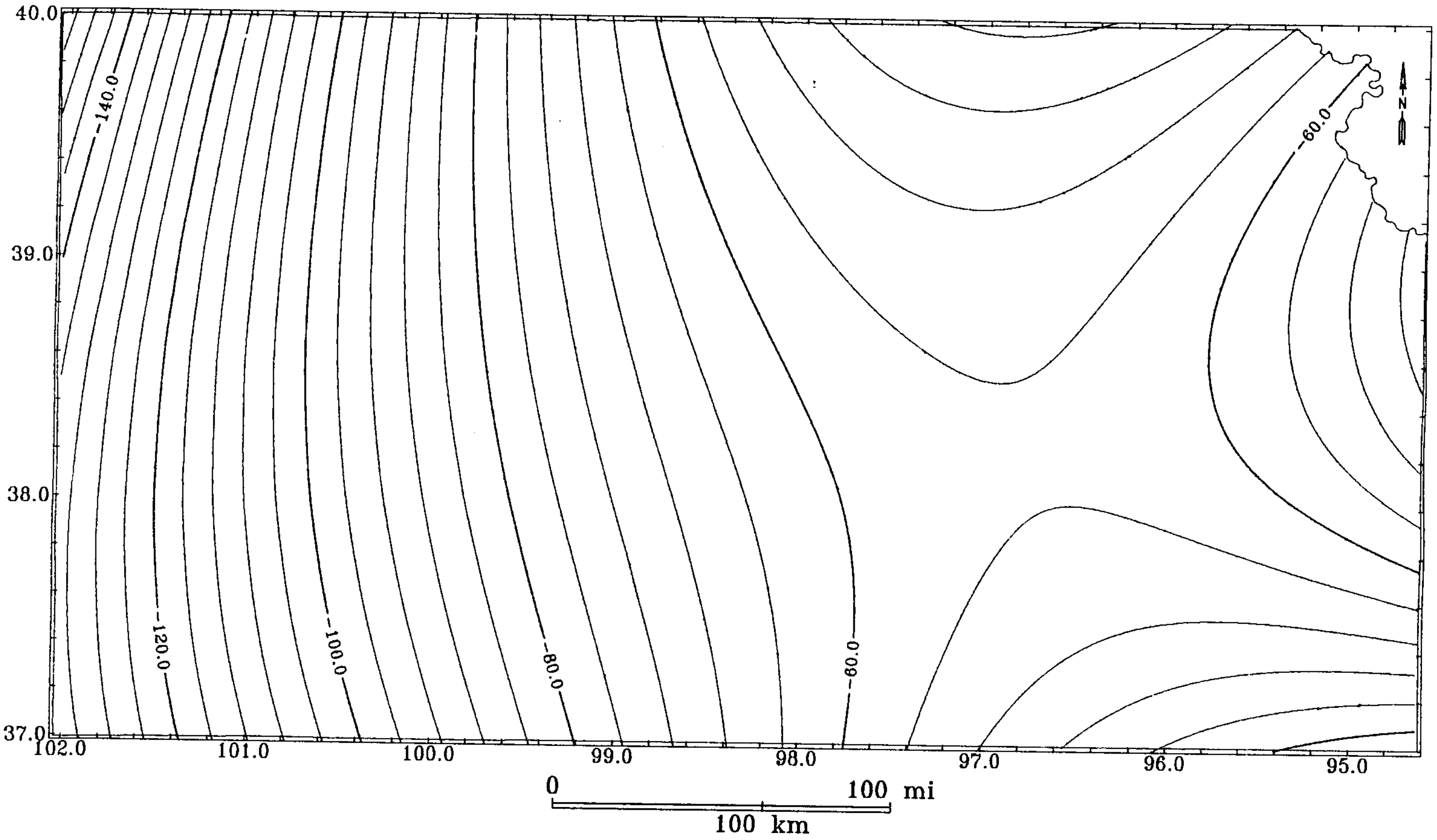

Figure 2-19. The regional Bouguer gravity in Kansas, the second order orthogonal-polynomial trend. Contour interval is 4 mGal. Coordinates in *x* and *y* directions are longitude and latitude in degrees, respectively.

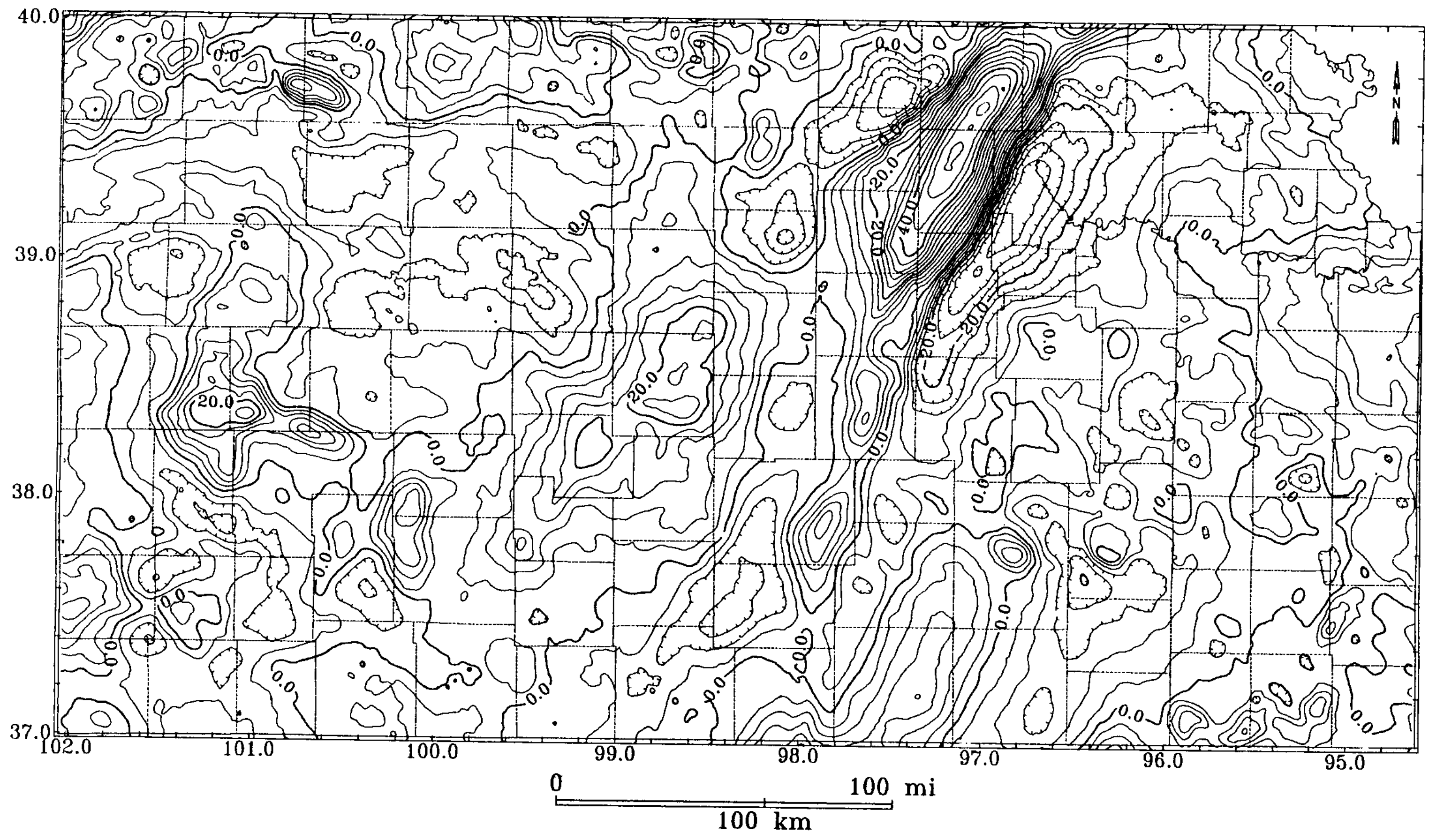

Figure 2-20. The residual Bouguer gravity in Kansas. Contour interval is 4 mGal. Coordinates in *x* and *y* directions are longitude and latitude in degrees, respectively.

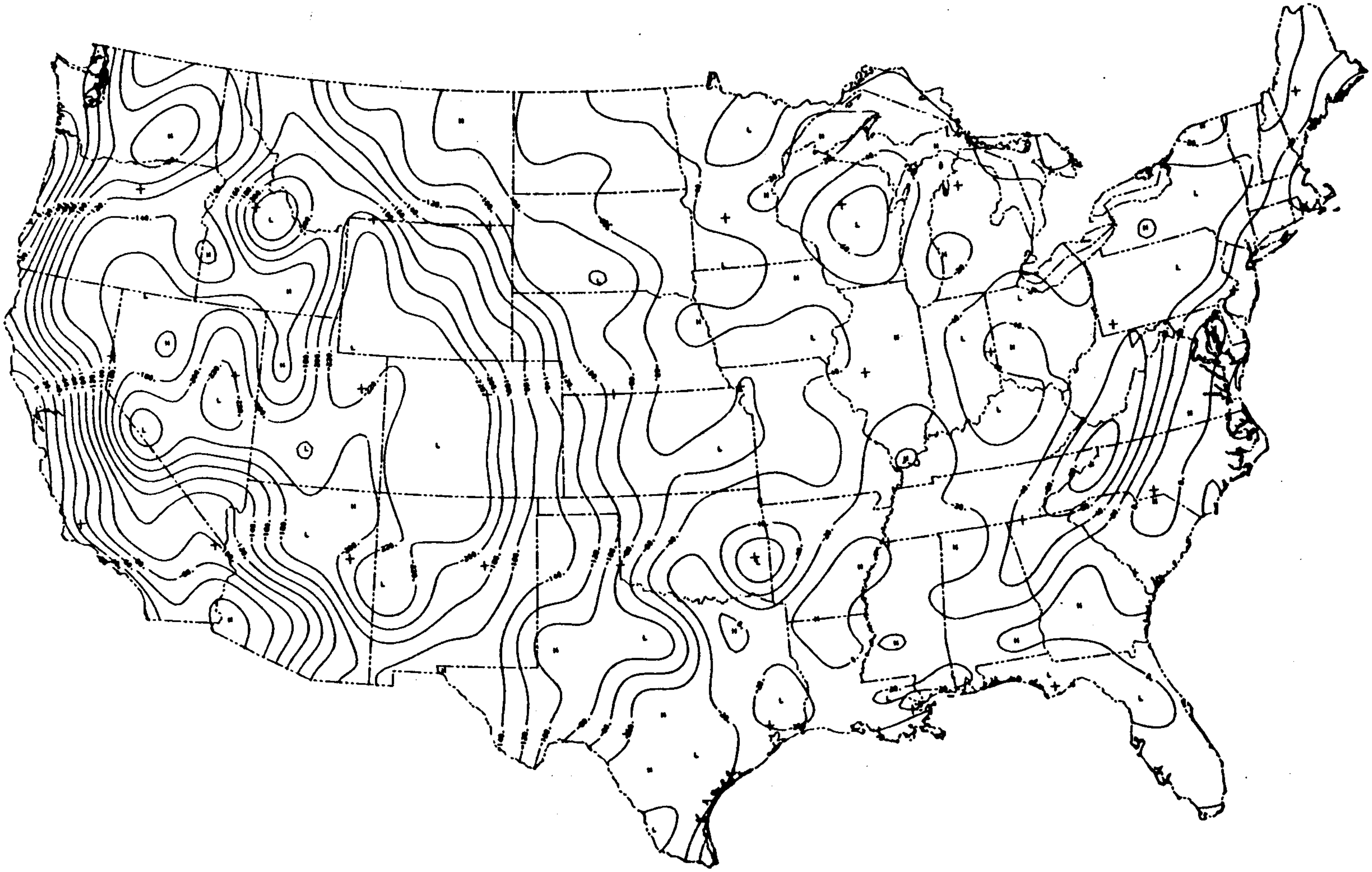

Figure 2-21. Regional Bouguer gravity map of the United States composed of wavelengths longer than 250 km. Contour interval is 20 mGal. After Kane and Godson (1985).

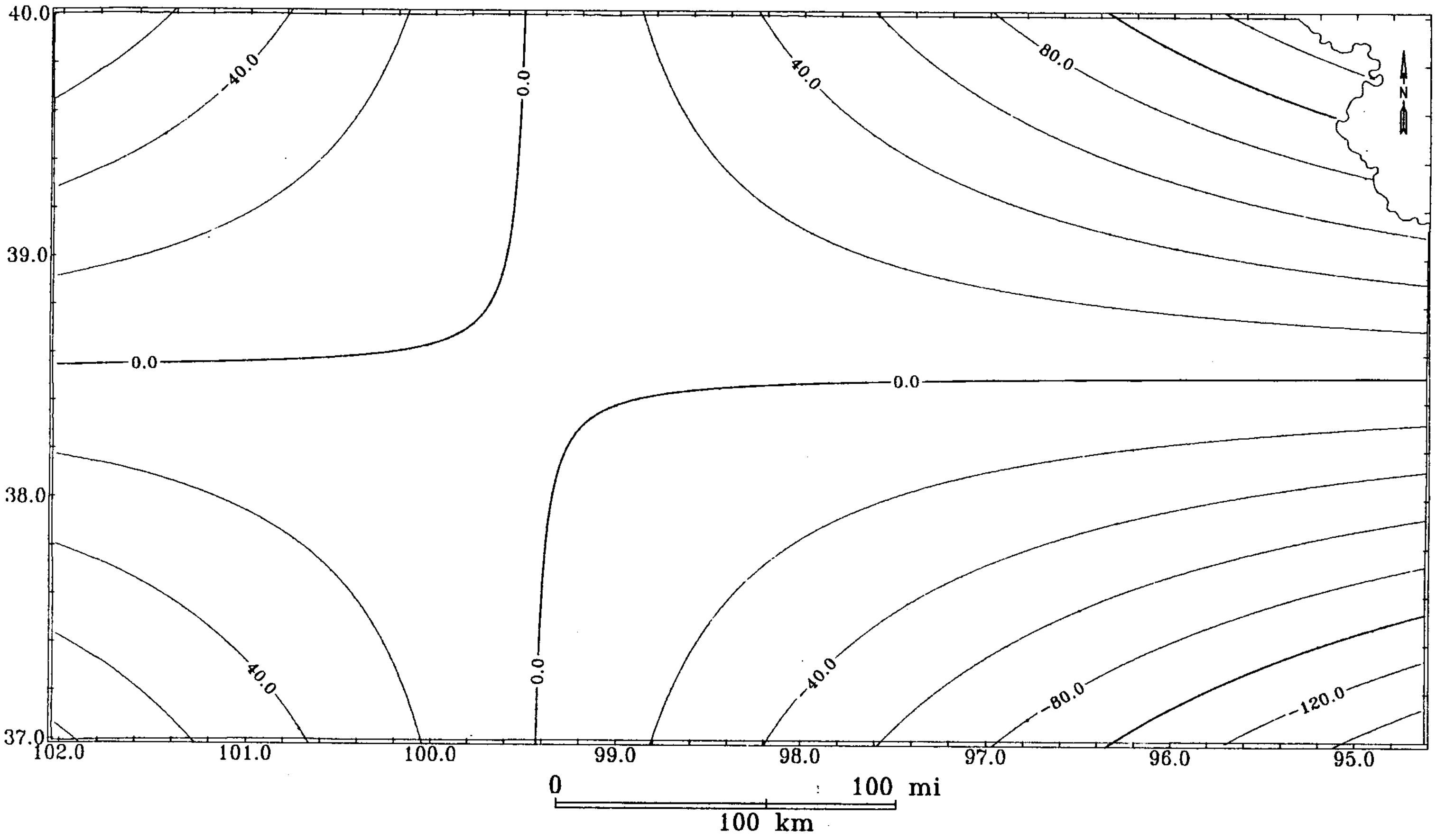

Figure 2-22. The regional magnetic anomaly in Kansas, the first order of orthogonal-polynomial trend. Contour interval is 20 nT. Coordinates in *x* and *y* directions are longitude and latitude in degrees, respectively.

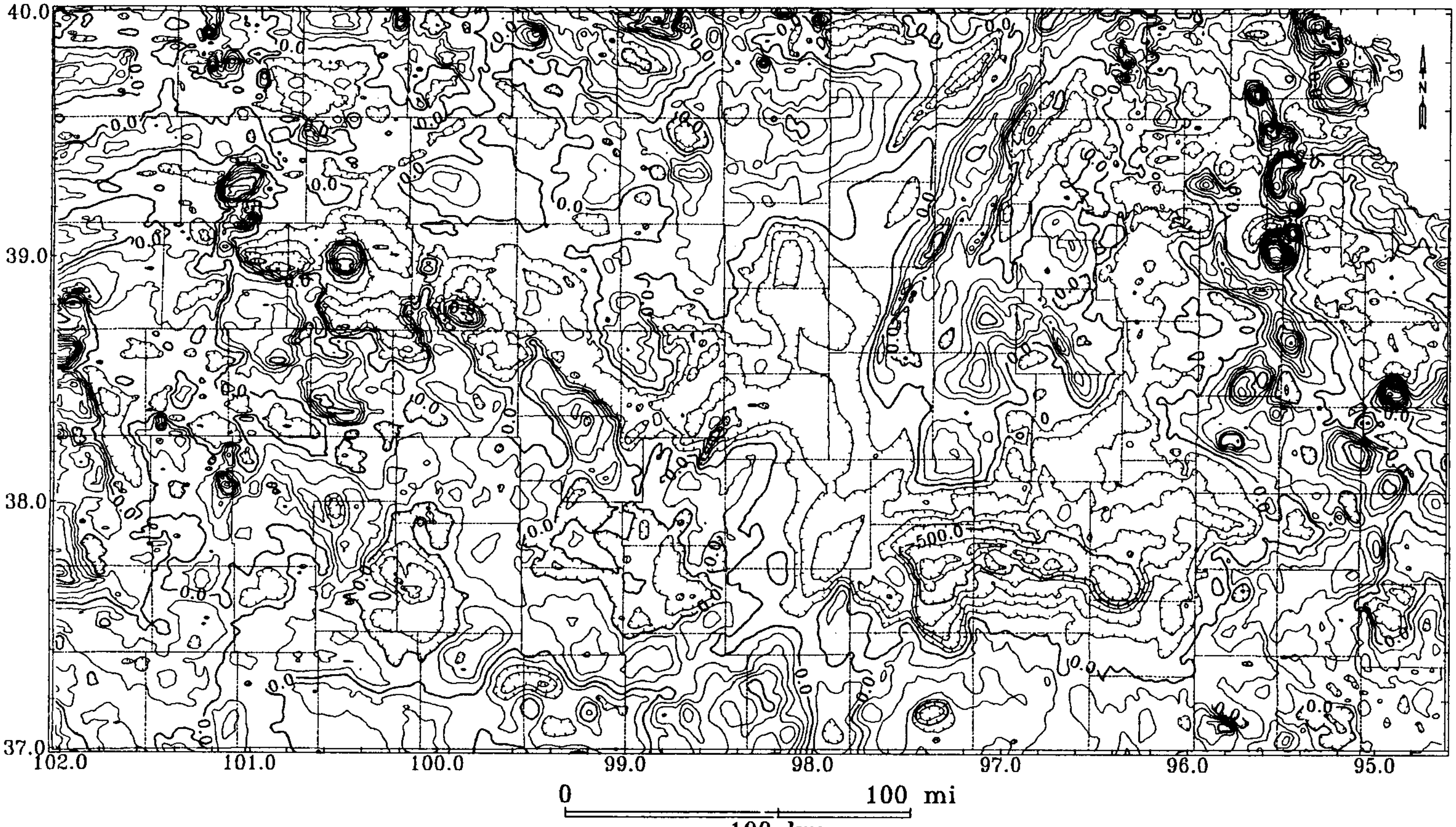

Figure 2-23. The residual magnetic anomaly in Kansas. Contour interval is 100 nT. Coordinates in *x* and *y* directions are longitude and latitude in degrees, respectively.

CHAPTER 3

INVERSION ASSUMING CONSTANT PARAMETERS

3.1. Introduction

The nonlinear inverse problem of mapping the interface topography from potential-field data was first discussed by Peters (1949) who proposed that by using a combination of downward continuation and the equivalence principle one could effectively map the topography of an interface separating uniformly but differently magnetized media. Inversion of potential-field data in the wavenumber domain has been of interest since Parker's (1973) formula was published. Oldenburg (1974) rearranged Parker's formula to find the topography of the basement from gravity data, and the approach was applied further by Kieniewicz and Luyendyk (1986). The inversion of magnetic anomalies to determine the magnetization of the subsurface was demonstrated by Parker and Huestis (1974).

In general, the inverse problem in geophysics is ill-posed in that the solution is non-unique and unstable. Inverse formulas in the wavenumber domain contain the downward continuation operator, which can cause divergence of the inversion operator. As discussed by Oldenburg (1974), a major problem is the instability of the technique because explicit or implicit downward continuation is involved. Therefore, recent implementations have involved theoretical or empirical regularization filters to taper growth of the exponential continuation function (Parker and Huestis, 1974; Oldenburg, 1974; Granser, 1986; Ferguson et al., 1988; and Reamer and Ferguson, 1989). Formulas for direct inversion of gravity and magnetic data were derived by Granser (1987) and Pustisek (1990), respectively. Both are based on Parker's formula and the Schmidt - Lichtenstein theory (e.g., Rall, 1974). For convergence of these formulas, only low frequencies are utilized, and thus high-frequency geologic information is lost. Pilkington and Crossley (1986) used the orthogonality of the Fourier transform to derive an approach requiring no matrix inversion. Again, high-cut filtering or some equivalent damping function is required. The largest set of data inverted in the above studies is approximately 9,000 gravity stations (Ferguson et al., 1988).

In the space domain, inversion by iterative forward modeling is common, repeating a sequence of direct calculations of the potential-field anomaly from a given model, comparing the calculated and observed values, and modifying the model until a satisfactory agreement is reached between observed and calculated values (Dobrin and Savit, 1988, p. 621). A number of methods have been developed for the forward calculation of potential fields from a model in two or three dimensions. Talwani et al. (1959) provides an efficient algorithm for the two-dimensional model, Cady (1980) modified the Talwani method for the so-called two-and-one-half-dimensional model, after Plouff (1976). For three-dimensional modeling, the method of Cordell and Henderson (1968) is frequently used. In their method, the density interface is divided into a number of vertical prisms by some averaging or interpolation scheme, and a linear function is applied to modify the depth of each prism after each iteration. This method takes longer than methods based on Parker's formula, especially for large data sets. For a large set of data, it is not possible to find a correction vector for the inverse model by matrix methods, and computing time and computer storage also do not allow solution of the inverse problem by matrix methods. The singular-value-decomposition technique can be used to determine a two-dimensional density interface (Xia, 1986), but is difficult to apply in three dimensions because there are too many unknowns.

Inversion of potential-field data does not yield a unique solution, because any observed potential-field can be produced by an infinite variety of sources (Dobrin and Savit, 1988, p. 163). Therefore, the inversion consists of finding a source in which certain parameter(s) may be adjusted to fit the observations. Convergence to a single solution can only be obtained when external constraints are placed on the subsurface geometry. Two such constrained geometries are dealt with in this study: a single, non-planar interface between two layers, each of uniform density or magnetization, and the distribution of the density or magnetization contrast within a single layer. The model of depth to a single, non-planar interface has obvious geological application. Given the geometry of the boundary, the derived distribution of density/magnetization looks like a geologic map (Cordell and McCafferty, 1989) and hopefully provides meaningful information about lithologic boundaries or geologic structures.

Inversion of large data sets in the spatial domain is impractical, but inversion in the wavenumber domain is efficient and effective. In this chapter, I first develop an inverse approach to determine the two above-mentioned models by iterative improvement in an initial subsurface model in the wavenumber domain. Forward calculation of anomalies is by Parker's (1973) algorithm (Blakely, 1981). I finish this chapter by testing the approach in two synthetic models to show that the inversion process is stable and is efficient for usage on large data sets.

3.2. Inverse Approach

In the wave-number domain, calculation of a gravity anomaly field *h(x,y)* due to a layer using Parker's formula (Equation 3.1) requires three known functions: the depth to the top of the layer ($ZT = z_1$), the depth to the bottom of the layer ($ZB = z_2$) and the distribution of the density $m(x,y)$, (see Figure 3-1).

$$F[h(x,y)] = 2\pi G \sum_{n=1}^{\infty} \frac{\left(-|\vec{k}|\right)^{n-1}}{n!} \times \left\{ e^{-|\vec{k}|\delta_2} F\left[m(x,y)\left(z_2(x,y)-\delta_2\right)^n\right] - e^{-|\vec{k}|\delta_1} F\left[m(x,y)\left(z_1(x,y)-\delta_1\right)^n\right] \right\}, \tag{3.1a}$$

where G is the gravitational constant; $\vec{k}$ is a wavenumber vector ($= k_x\vec{e}_x + k_y\vec{e}_y$, $\vec{e}_x$ and $\vec{e}_y$ are the unit vector in x and y directions, respectively.); δ_1 and δ_2 are the average values of Z_1 and Z_2, respectively; F is the Fourier transform. Based on Poisson's relation (e.g., Dobrin, 1976, p. 483), an equation for calculating total field magnetic anomalies can be written down directly from Equation (3.1a), which is shown in Equation (3.1b).

$$F[h(x,y)] = 2\pi\phi(\vec{k}) \sum_{n=0}^{\infty} \frac{\left(-|\vec{k}|\right)^{n}}{n!} \times \left\{ e^{-|\vec{k}|\delta_2} F\left[m(x,y)\left(z_2(x,y)-\delta_2\right)^n\right] - e^{-|\vec{k}|\delta_1} F\left[m(x,y)\left(z_1(x,y)-\delta_1\right)^n\right] \right\}, \tag{3.1b}$$

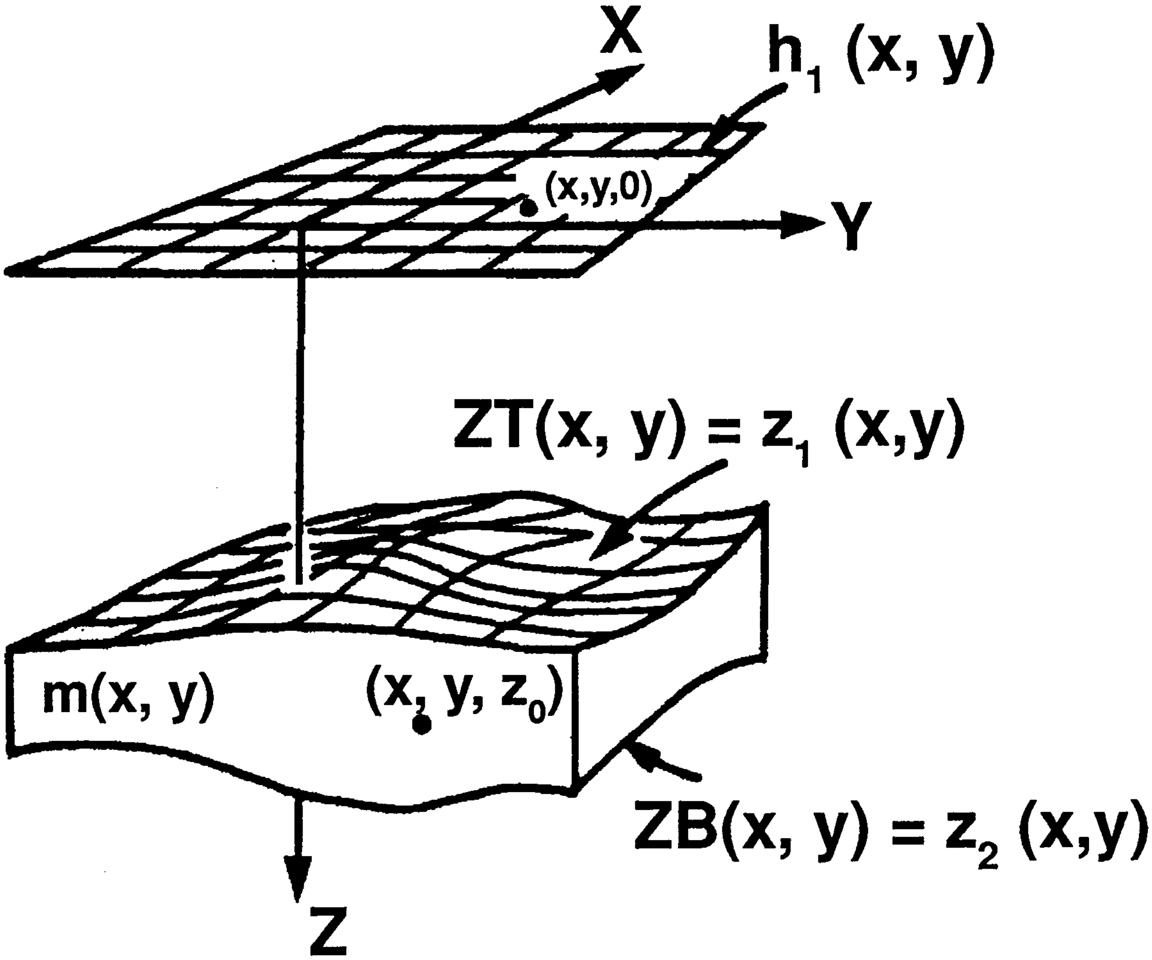

Figure 3-1. Geometry of observation surface and a physical layer. After Blakely (1981).

where $m\,(x,y)$ is the distribution of the magnetization contrast; $\phi(\vec{k})$ is a function of the wavenumber and is defined by

$$\phi(\vec{k}) = -\frac{(\vec{k}\cdot\vec{e})(\vec{k}\cdot\vec{j})}{|\vec{k}|^2};$$

$\vec{k} = i(k_x\vec{e}_x + k_y\vec{e}_y) + \sqrt{k_x^2 + k_y^2}\,\vec{e}_z$, $i = \sqrt{-1}$ is the imaginary unit;

$\vec{e} = f_x\vec{e}_x + f_y\vec{e}_y + f_z\vec{e}_z$, is the unit vector of the earth's magnetic field;

$\vec{j}$ is the unit vector of the magnetization with inclination (I) and declination (D); $m(x,y)$ is the length of the magnetization; and "$\cdot$" stands for the dot product of two vectors. The directions of the earth's field and the magnetization (inclination (I) and declination (D)) must be known for calculating a magnetic anomaly. The forward series expansion of Parker's formula is uniformly convergent for any reasonable topographic relief functions, *ZT* and *ZB* (Parker, 1973).

If *ZB* is known and the distribution of density/magnetization contrast ($\Delta\rho/J$) is known, then the goal of inversion is to determine *ZT*. Conversely, given *ZT* and *ZB*, I can determine the distribution function of density/magnetization contrast in the layer defined by *ZT* and *ZB*. For inverting magnetic anomalies, the direction of magnetization is assumed to be known. In either case, an initial model is assumed and its effects are determined. Misfit between the modeled field and the observed field is specified by error parameters. The error parameters are then reduced by iterative modification of the geologic model.

3.2.1. Initial model

If the depth to the top of the layer is to be calculated, I initialize *ZT* to an average depth and define $\Delta\rho$ (or J with known I and D) and the depth to the bottom of the layer (*ZB*), which are kept constant while solving for *ZT*. If the inversion is for distribution of density (or magnetization) contrast, I initialize the model $\Delta\rho$ (or J with known I and D) to an average value and define ZT and ZB which are held constant during the inversion.

3.2.2. Model modification

The formulas used to modify the model after each iteration are given below.

Case 1. Modifying the depth to the top of a magnetic layer.

$$\Delta H_i^k = 2\left[\tan(h_i^k / 4\bar{J}) - \tan(T_i / 4\bar{J})\right](ZT_i^k)^2 / \Delta L, \tag{3.2}$$

where superscript k is the kth iteration and subscript i is the ith data point; ΔH_i^k is the modification to the depth ZT_i^k, the depth of ZT below point i at the kth iteration; h_i^k and T_i are the calculated and measured total magnetic field anomalies, respectively; and ΔL is the average distance between data points;

$$\bar{J} = J \times (\sin^2 I - \cos^2 I \times \sin^2 D),$$

where I and D are the angles of inclination and declination, respectively, of the magnetization contrast, J.

Case 2. Modifying the distribution of magnetization contrast in the layer.

$$\Delta J_i^k = (T_i - h_i^k) / 4\tan^{-1}(\Delta L / 2ZT_i^k), \tag{3.3}$$

where ΔJ_i^k is the modification to J_i^k, the magnetization contrast below point i at the kth iteration.

Case 3. Modifying the depth to the density interface (Bott, 1960).

$$\Delta H_i^k = (g_i - h_i^k) / 2\pi G \Delta\rho, \tag{3.4}$$

where g_i and h_i^k are the measured and calculated gravity anomalies, respectively, G is the gravitational constant, and $\Delta\rho$ is the density contrast. Bott used this formula to solve the depth to the basement in two-dimensional sedimentary basins.

Case 4. Modifying the distribution of density contrast in the layer.

$$\Delta\rho_i^k = (g_i - h_i^k) / 2\pi G(ZB_i - ZT_i), \tag{3.5}$$

where $\Delta\rho_i^k$ is the modification to ρ_i^k, the density contrast below point i at the kth iteration.

Equations (3.2) and (3.3) are simplified from the 2-D vertical dike (Telford et al., 1982, p. 166). Equations (3.4) and (3.5) are based on the Bouguer-slab formula.

Two error parameters used to measure the effectiveness of the iterative procedure are a root-mean-square error, $RMS(k)$, at the kth iteration,

$$RMS(k) = \sqrt{\frac{1}{N}\sum_{i=1}^{N}(h_i^k - f_i)^2} \tag{3.6}$$

and the maximum deviation, $MAXD(k)$, at the kth iteration,

$$MAXD(k) = \max_{1\le i\le N}\left|h_i^k - f_i\right|, \tag{3.7}$$

where f_i is the measured anomaly at the ith point, and N is the total number of data points.

Figure 3-2 shows the flowchart of the inverse procedure. The inversion approach can be described as follows: 1) Determine an initial model: initialize the model ZT to a average depth of the interface and define $\Delta\rho$ (or J) = constant and ZB =

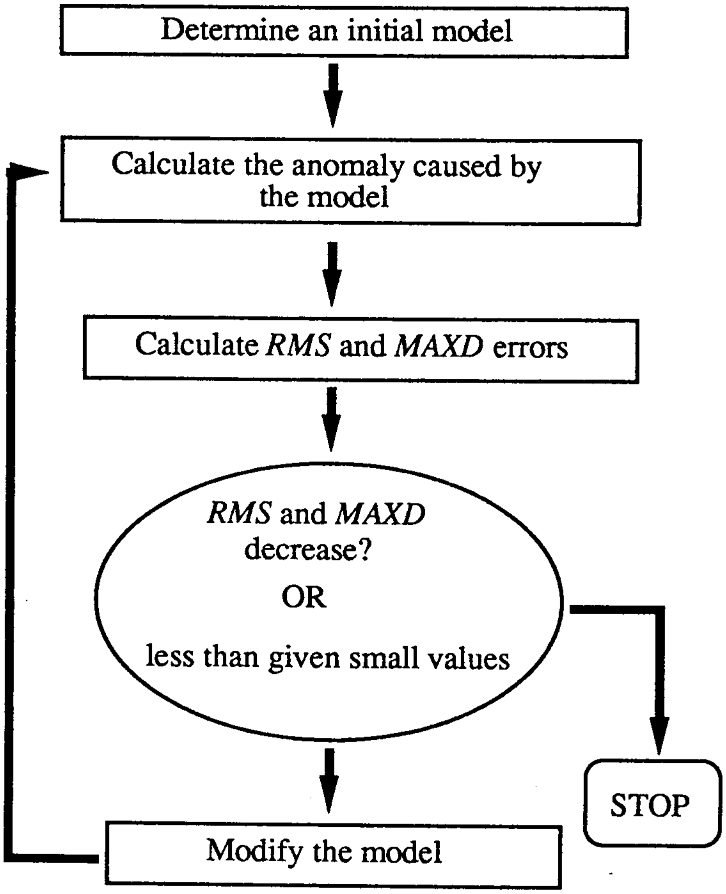

Figure 3-2. Flowchart of the inverse approach by iterative forward modeling.

constant (≥*ZT*) for case 3 (or case 1), or initialize the model $\Delta\rho$ (or J) to a average value and define *ZT* and *ZB* for case 4 (or case 2); 2) Calculate the anomaly $h(x,y)$ by Parker's formula and the *RMS* and *MAXD* errors by formulas (3.6) and (3.7), if neither of these errors are reduced or the *RMS* reaches the accuracy threshold, the iterative procedure will be terminated, otherwise; 3) Modify the model by one of the formulas (3.2) - (3.5) according to the goal of inversion and the type of anomaly, then return to step 2.

Iterative improvement to the geologic model should cause reduction in both of the errors, and the errors are minimized as the solution converges. In practice, a given iteration may not reduce both errors simultaneously because the modifications to the model are approximate. Iteration continues until no further improvement in either error is realized or when *RMS* reaches the accuracy threshold of the observational data.

The approach allows one to determine density/magnetization distribution within an undulating layer. This flexibility is very useful when inverting real potential-field data, as shown in Chapter 5.

The uniqueness of the derived model of depth to the top of the layer is restricted by the uncertainty in the assumed density/magnetization contrast and the assumed average depth to this interface. Clearly, reduction in the assumed density/magnetization contrast (or increase in average depth to interface) increases topographic relief on the calculated surface. Appropriate solutions are possible only when the initial parameters are constrained by other geological or geophysical information.

3.3. Synthetic Examples

Utility of the technique can be demonstrated using synthetic data. Also, the synthetic examples are used to debug the computer program. In this section, I will invert a synthetic magnetic anomaly into two models; one is the depth to the top of magnetic body, and the other is the magnetization distribution within a given layer. I will also invert a synthetic gravity anomaly into two models, one is the depth to the top of the anomalous density body, and the other is the density distribution within a given layer. In Figure 3-3a, a rectangular solid with a size of 80 km × 80 km × 3 km is buried at the center of the data field. The depth to the top and the bottom of the solid are 3 km and 6 km, respectively. Magnetization contrast and density contrast of the solid is 400 nT, and 0.5 g/cm^3, respectively. The inclination and declination of magnetization are 60 degrees and 45 degrees, respectively. Anomaly values were calculated at $z = 0$ km on a 100×100 grid of points, spaced every 1.6 km (1 mi). The synthetic magnetic anomaly is calculated with the formula given by Bhattacharyya (1964) and the synthetic gravity anomaly is calculated by Nagy (1966). Because the anomaly caused by the rectangle is equivalent to the anomaly caused by the interface (Figure 3-3b), the anomaly data can be inverted to determine either the topography of the upper interface (Figure 3-3b), or the magnetization contrast of the solid. The same is true for the gravity model.

3.3.1. Depth to top of magnetic body

This is case 1 to determine the upper magnetic interface. Assume $J = 400$ nT, which is the value of magnetization contrast of the synthetic model, and $ZB = 100$ km. I initialized the model to $ZT = 4.5$ km, which is the average depth to the interface. *RMS* and *MAXD* of the initial model are 132.1 nT and 626.3 nT, respectively. After 17 iterations, *RMS* is reduced to 37.2 nT (6% of the maximum anomaly) and *MAXD* is reduced to 128.9 nT. The final modeled interface *ZT* is shown in Figure 3-4. The edge locations, absolute amplitude, and depth to top and bottom of the structural step are well determined.

3.3.2. Magnetization distribution in a given layer

This is case 2 to determine the distribution of magnetization contrast. Assume $ZT = 3$ km and $ZB = 6$ km, and initialize the magnetization to 200 nT, which is the average magnetization of the synthetic model. The initial errors are the same as in case 1. After 20 iterations, the errors *RMS* is reduced to 28.9 nT (4.4% of the maximum anomaly) and *MAXD* is reduced to 99.2 nT. The final model of distribution of magnetization contrast in the layer, is shown in Figure 3-5. The modeled distribution is reasonably close to the actual values and the edges of the solid are well defined.

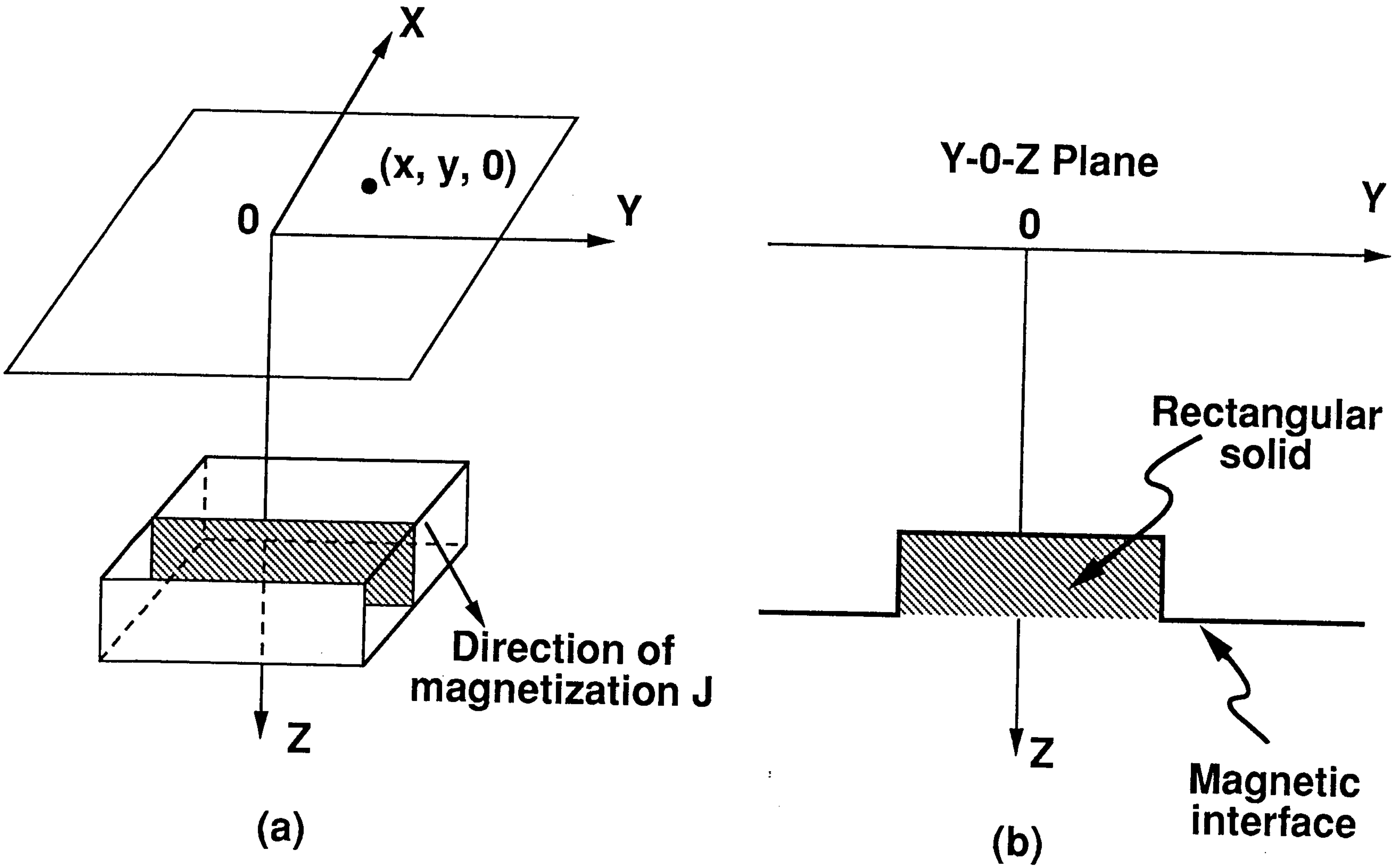

Figure 3-3. Anomaly caused by the rectangular solid (a) is equivalent to the anomaly caused by the interface (b).

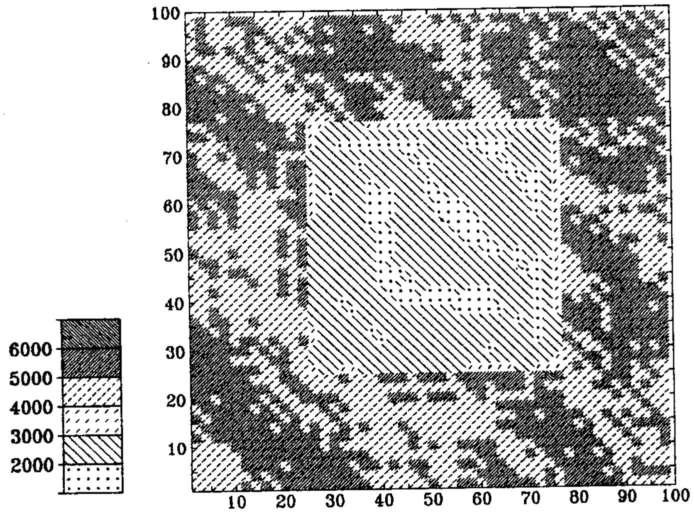

Figure 3-4. Inverse solution for depth to upper magnetic interface of the model in Figure 3-3. Shading interval is 1,000 m. The unit in both x and y directions is station-spacing, 1.6 km (1 mi).

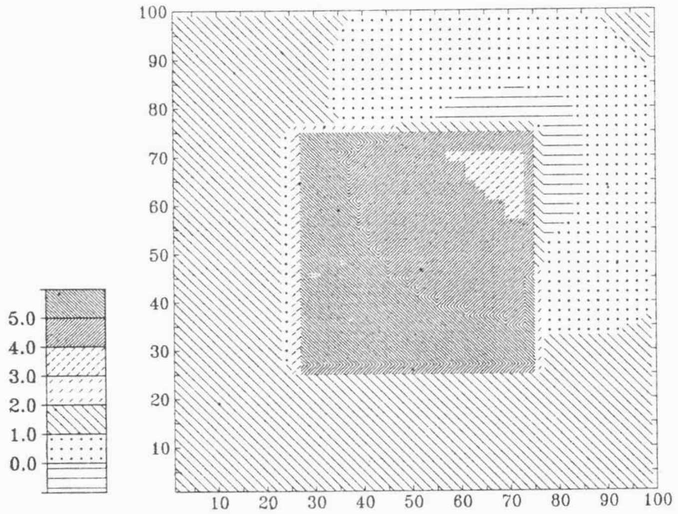

Figure 3-5. Calculated distribution of magnetization contrast within the model shown in Figure 3-3. Shading interval is 1 × (100) nT. The unit in both x and y directions is station-spacing, 1.6 km (1 mi).

Figure 3-6 shows the continual reduction in the two errors during inversion. The inversion procedure is stable and the formulas used to modify the magnetic models are appropriate.

In examples 1 and 2, the selected direction of magnetization (*I* and *D*) is equal to the actual values. Introducing errors in *I* and/or *D* of 5 to 10 degrees distorts magnetic anomalies by $RMS \in (8 \text{ nT}, 43 \text{ nT})$ (or $MAXD \in (35 \text{ nT}, 194 \text{ nT})$), that is, if errors in both of *I* and *D* are 5 degrees, *RMS* error in the magnetic anomaly will be 8 nT; if errors in *I* and *D* are 10 degrees, *RMS* error will be 43 nT. For this particular model, distortions in anomalies are almost a linear function of errors in *I* and/or *D*, when the errors are less than 10 degrees. With errors in *I* and/or *D* less than 7.5 degrees, the final results are not significantly altered. Calculation of error due to mis-estimation of initial magnetization is straight-forward because magnetic anomalies are linear functions of magnetization. In case 1, 5% error in *J* does not produce significant error in the depth-to-interface estimation.

3.3.3. Depth to top of anomalous density body

This is case 3, determining the upper density interface. Assume $\Delta\rho = 0.5$ g/cm^3, which is the value of density contrast of the synthetic model, and *ZB* = 100 km. I initialize the model *ZT* = 5.5 km, which is the average depth to the interface. *RMS* and *MAXD* of the initial model are 21.0 mGal and 46.2 mGal, respectively. After 6 iterations, *RMS* error is reduced to 0.4 mGal (1% of the maximum anomaly) and *MAXD* is reduced to 1.9 mGal. The final modeled interface *ZT* is shown in Figure 3-7. The edge locations, absolute amplitude, and depth to top and bottom of the structural step are well determined.

3.3.4. Density distribution in a given layer

This is case 4, determining the distribution of density contrast. Assume *ZT* = 3 km and *ZB* = 6 km, and initialize the density contrast to 0. The initial errors are the same as in case 3. After 6 iterations, *RMS* error is reduced to 0.3 mGal (less than 1% of the maximum anomaly) and *MAXD* is reduced to 1.9 mGal. The final model of

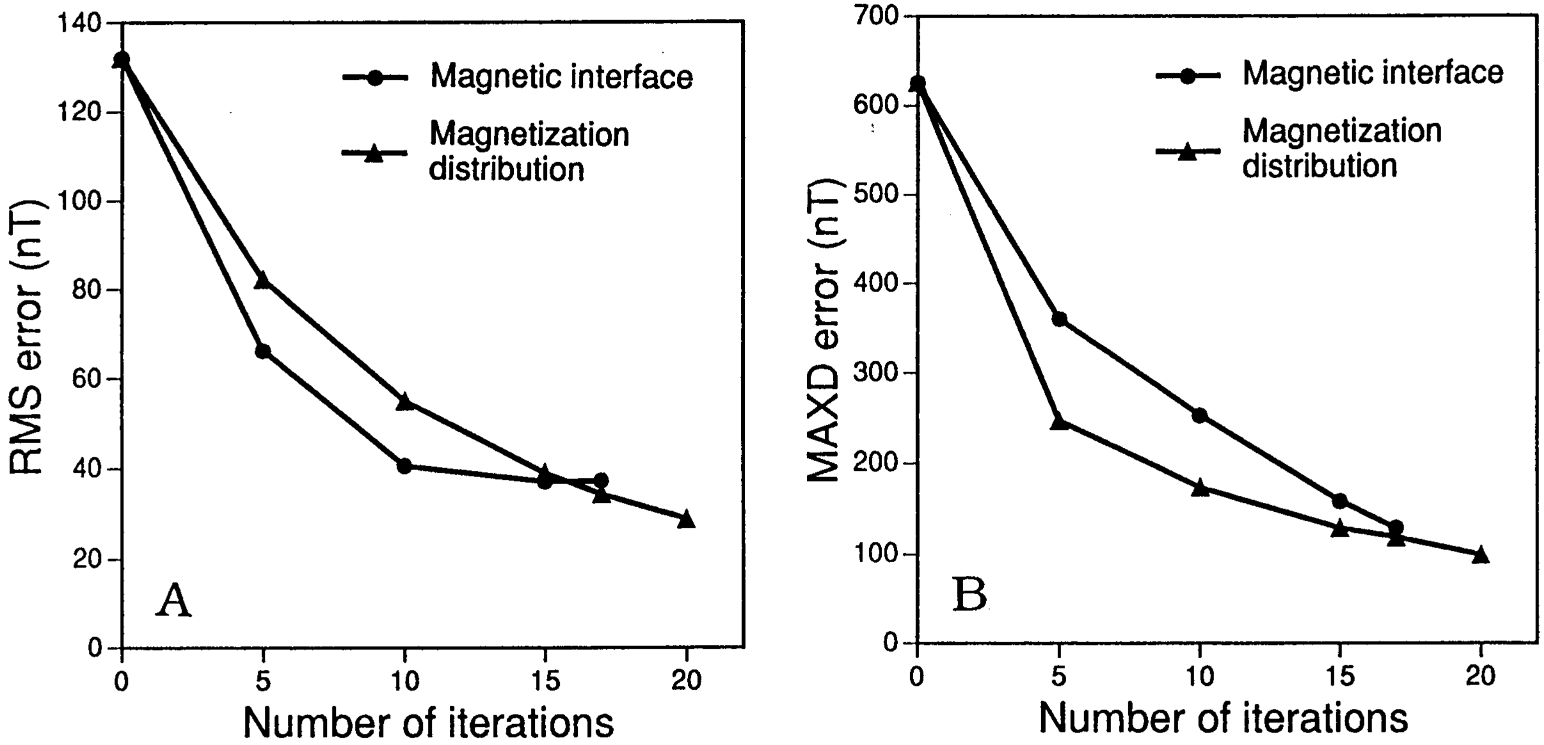

Figure 3-6. The convergent curves of the *RMS* (a) and *MAXD* (b) errors for the synthetic example.

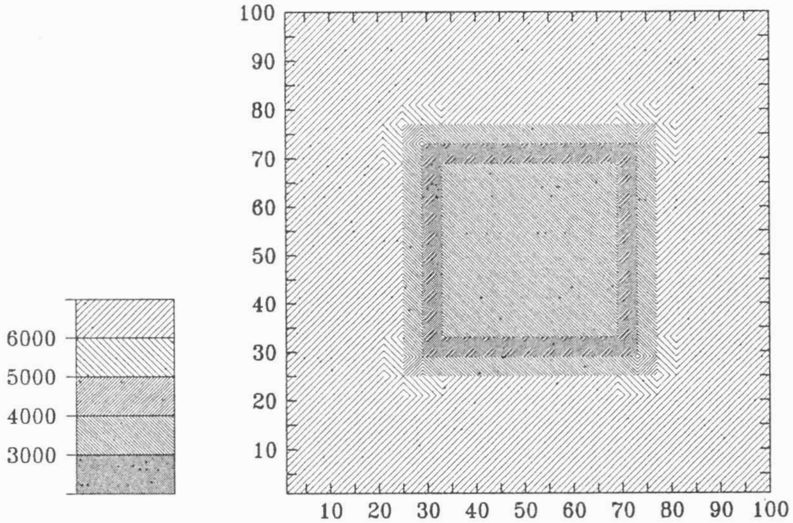

Figure 3-7. Inverse solution for depth to upper density interface of the model in Figure 3-3. Shading interval is 1,000 m. The unit in both in x and y directions is station-spacing, 1.6 km (1 mi).

distribution of density contrast in the layer, is shown in Figure 3-8. The modeled distribution is close to the actual distribution and the edges of the solid are well defined.

Each iteration in all of four examples took about 10 CPU seconds on a Data General MV20000. The inverse procedures are stable and fast enought to apply to a large set of data.

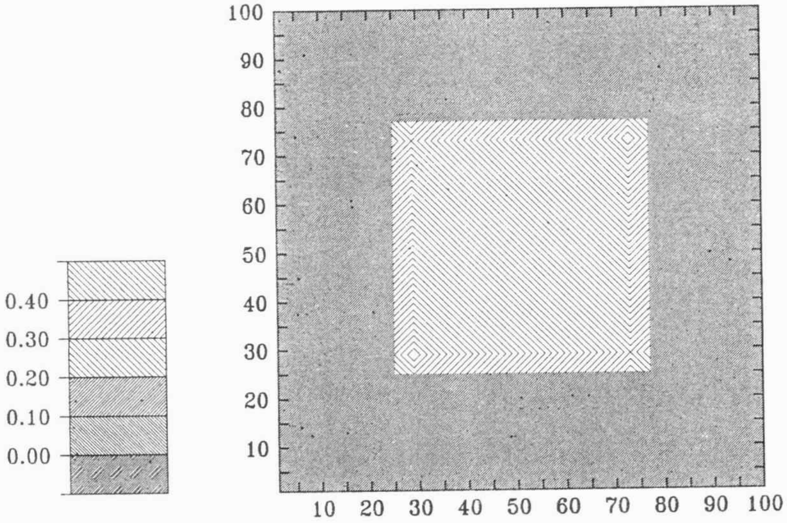

Figure 3-8. Calculated distribution of density contrast within the model shown in Figure 3-3. Shading interval is 0.1 g/cm^3. The unit in both *x* and *y* directions is station-spacing, 1.6 km (1 mi).

CHAPTER 4

INVERSION WITH AN EXPONENTIAL DENSITY MODEL

4.1. Introduction

In the mapping of a density interface, complex geology requires consideration of a variable density contrast above the interface as a function of depth. It is well known that the density of sedimentary rocks increases as a function of their depth of burial (Athy, 1930). The density of the rocks rapidly increases at shallow depths and increases progressively less rapidly at great depths. And the density of the rocks in the upper part of the earth's crust is less than the density of the rocks in the lower part of the earth's crust. As a result, treating the density contrast of rocks as a function of depth is reasonable.

It is difficult, however, to derive a formula for calculating the gravity anomaly over even a simple geometrical body with a density varying even linearly with depth in the spatial domain. Reamer (1986) derived a formula for the gravity anomaly of a linear density contrast model in the wavenumber domain. Reamer and Ferguson (1989) also discussed an inversion of a gravity anomaly into a density interface based on the linear density contrast model in the wavenumber domain. It is impossible to obtain an analytical expression in the spatial domain for the gravity anomaly of even a simple geometrical body when the density of the body varies exponentially with depth (Murthy and Rao; 1979). Cordell (1973) proposed a recursive procedure and Murthy and Rao (1979) extended Hubbert's (1948) line-integral method for the case of a linear density model to obtain an approximate solution for the exponential density contrast model. Chai and Hinze (1988) and Chenot and Debeglia (1990) presented an approach based on using vertical prisms with the exponential density contrast model in the wavenumber domain to invert the gravity anomaly into a density interface.

In this chapter, I first derive an analytical expression for calculating the gravity anomaly caused by a layer, density contrast in which changes with depth exponentially. Next, I show that the formula for calculating the gravity anomaly caused by the exponential density contrast model is correct. In order to show this, I first calculate the anomalies caused by a set of rectangles with varying densities, which are approximately determined by an exponential model. The summation of all anomalies caused by the rectangles should be very close to the anomaly directly calculated by the formula of the exponential density model. I compare both anomalies, which are caused by a set of a rectangular solids and calculated directly by the formula of the exponential density model. I finish this chapter by discussing an approach to invert the gravity anomaly by iterative forward modeling with the exponential density contrast model.

4.2. Forward Formula of an Exponential Density Contrast Model

An exponential density contrast model is

$$\Delta\rho(z) = a + be^{-\mu z} , \tag{4.1}$$

where (a+b) is a density contrast of surface rocks of a layer and μ is a decay constant with the unit of 1/length. The gravity anomaly caused by the layer with this density model is $h = h_1 + h_2$. The first term h_1, which is caused by the constant density a, can be calculated by Parker's formula. I have derived a formula (Equation 4.2) for calculating the gravity anomaly h_2 caused by the second exponential term. The derivation of Equation (4.2) is given in Appendix C.

$$F[h_2(x,y)] = 2\pi G b \sum_{n=1}^{\infty} \frac{\left[-\left(\mu + |\vec{k}|\right)\right]^{n-1}}{n!} \times$$

$$\left\{ e^{-\left(\mu+|\vec{k}|\right)\delta_2} F\left[\left(z_2(x,y) - \delta_2\right)^n\right] - e^{-\left(\mu+|\vec{k}|\right)\delta_1} F\left[\left(z_1(x,y) - \delta_1\right)^n\right] \right\} , \tag{4.2}$$

where F is Fourier transform; G is the gravitational constant; $\vec{k}$ is the wavenumber vector, $\vec{k} = k_x\vec{e}_x + k_y\vec{e}_y$, $\vec{e}_x$ and $\vec{e}_y$ are the unit vectors in x and y directions, respectively; $z_1(x,y)$ and $z_2(x,y)$ are the top surface and the bottom surface of the layer, respectively; δ_1 and δ_2 are the median values of $z_1(x,y)$ and $z_2(x,y)$, respectively.

If μ is zero, the second term in Equation (4.1) become the constant b, and Equation (4.2) simplifies to Parker's formula. In Appendix C, I show that the linear density contrast model (Reamer, 1986) is a specific case of the exponential density contrast model. It is also apparent that calculation of h_2 will require the same order of magnitude of time as the calculation of h_1. Equation (4.2) should be more computationally efficient than the formula using vertical prisms with the exponential model, Equation (4.1), to fit an interface (Chai and Hinze, 1988; Chenot and Debeglia 1990). The time savings are derived at the point of Fourier transformation.

4.3. Testing by a Rectangular Solid Model

A rectangular solid model is shown in Figure 4-1, which could be representative of a graben with vertical sides. The size of the solid is 1,000 m × 1,000 m × 800 m (3,300 ft × 3,300 ft × 2,600 ft) with a density contrast

$$\Delta\rho(z) = 0 \ \text{g/cm}^3, \ 0 \text{ m} < z < 50 \text{ m}, \tag{4.3a}$$

$$\Delta\rho(z) = -0.5e^{-0.0018z} \ \text{g/cm}^3, \ 50 \text{ m} \le z \le 850 \text{ m}. \tag{4.3b}$$

It is located in the center of the data area with the top at a depth of 50 m (160 ft) and the bottom at the depth of 850 m (2,790 ft). Figure 4-2 shows the exponential density contrast model of Equation (4.3). The measurement points are 50 × 50 with a station spacing of 100 m in both x and y directions.

Figure 4-3 shows the result directly from Equation (4.2) with the density model of Equation (4.3). The series in Equation (4.2) are cut off after n is larger than 8. The ratio of the eighth term to the summation of first seven terms is less than 1.5×10^{-6}, indicating rapid convergence of the series in Equation (4.2).

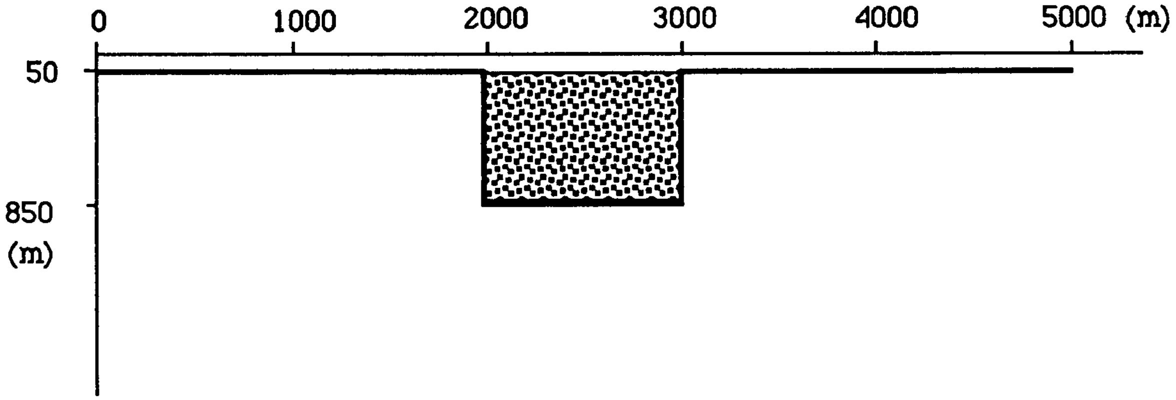

Figure 4-1. The geometry of a rectangular solid model.

I divide the rectangular model in Figure 4-1 into eight thinner rectangles, each of which has thickness of 100 m (330 ft). The top of the first thinner rectangle is 50 m (170 ft) and its bottom is at a depth of 150 m (500 ft); the top of the second thinner rectangle is 150 m (500 ft) and its bottom at a depth of 250 m (830 ft), and so on. The values of density contrast for each rectangle are listed in Figure 4-2. The summation of anomalies caused by all these thinner rectangles is shown in Figure 4-4, which are calculated by the rectangular formula (Nagy, 1966).

Obviously, I expect that the anomalies shown in Figures 4-3 and 4-4 should be very similar. Figure 4-5 shows the difference between the two anomalies. The maximum deviation between the two anomalies is 0.25 mGal, which is less than 5 percent of the amplitude of the expected anomaly. The difference is due to approximations in the eight-piece model and by noise from the Gibbs phenomena in Fourier transformation.

4.4. Inverse Approach

The two main steps in the inverse approach are determination of an initial model and modification of the model.

4.4.1. Initial model

I initialize *ZT* (the depth to the top of the layer) to an average depth and define an exponential density contrast model and the depth to the bottom of the layer (*ZB*), which are kept unchanged while solving for *ZT*. After these three parameters are determined, I can calculate the anomaly due to the initial model with Equation (4.2).

4.4.2. Model modification

The formula used to modify the depth to the density interface after each iteration is almost the same as the formula for the constant density contrast model of Equation (3.4). The only difference is the density contrast is not a constant here. The formula is

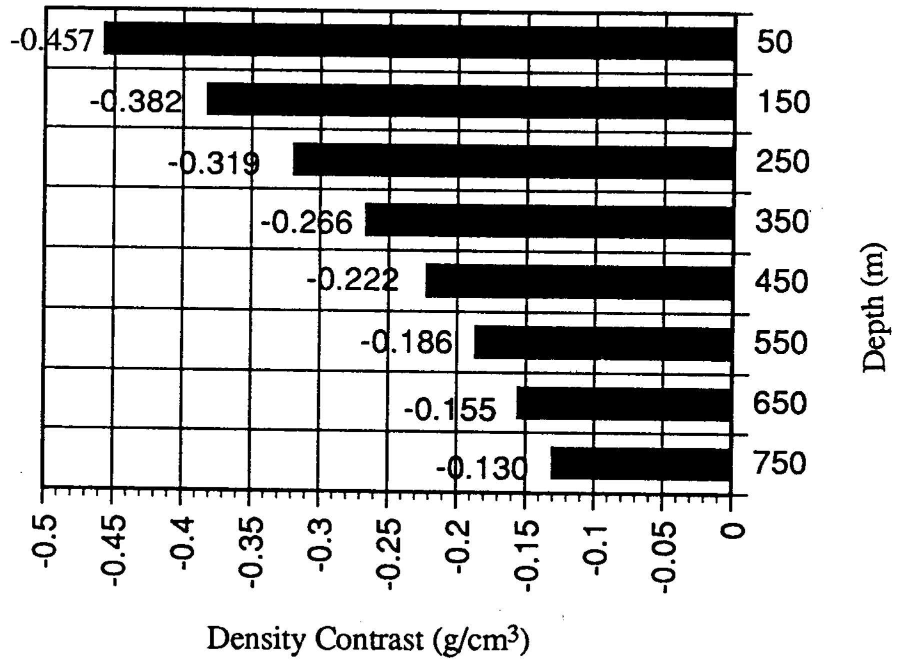

Figure 4-2. An exponential density contrast model used in the rectangular solid in Figure 4-1. The density contrast values next to the bars are determined by the exponential density contrast model of Equation (4.3) and used in eight thinner rectangles.

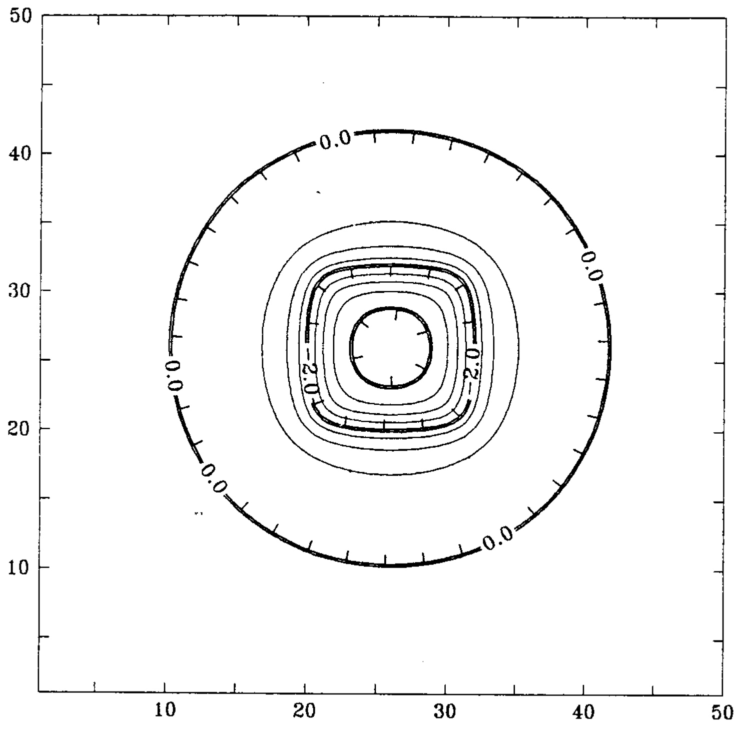

Figure 4-3. The gravity anomaly caused by the rectangular solid model with the density contrast model of Equation (4.3) and calculated by Equation (4.2). Contour interval is 0.5 mGal. The unit in both x and y directions is a station spacing, 100 m.

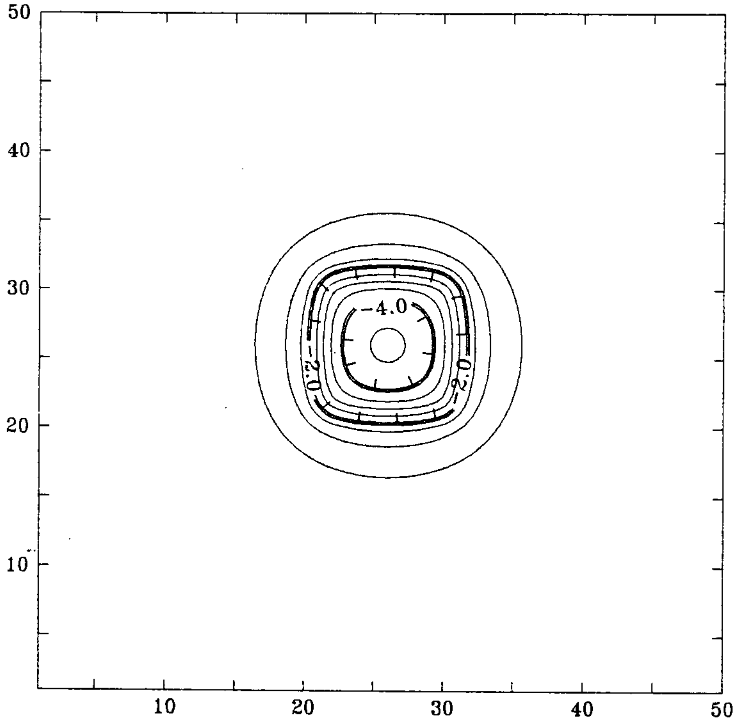

Figure 4-4. The summation of gravity anomalies caused by the eight thinner rectangular solids with the constant densities shown in Figure 4-2 and calculated by the rectangular formula (Nagy, 1966). Contour interval is 0.5 mGal. The unit in both *x* and *y* directions is a station spacing, 100 m.

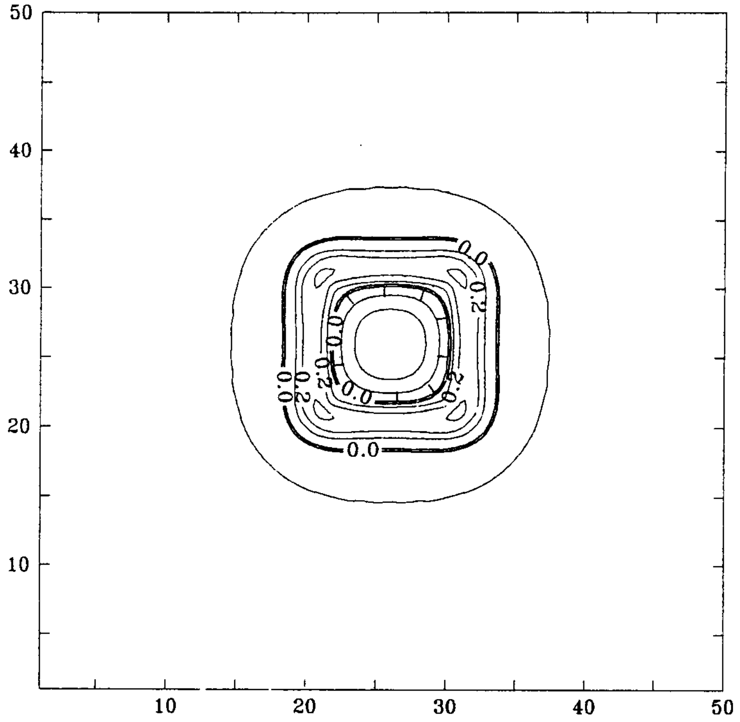

Figure 4-5. The difference between Figure 4-3 and Figure 4-4. Contour interval is 0.1 mGal. The unit in both *x* and *y* directions is a station spacing, 100 m.

$$\Delta H_i^k = (g_i - h_i^k) / 2\pi G \Delta\rho_i, \tag{4.4}$$

where superscript k is the kth iteration and subscript i is the ith data point; ΔH_i^k is the modification to the depth ZT_i^k, the depth of ZT below point i at the kth iteration; g_i and h_i^k are the measured and calculated gravity anomalies, respectively; G is the gravitational constant; and $\Delta\rho_i$ is the density contrast, which is function of the depth.

Two error parameters used to measure the effectiveness of the iterative procedure are a root-mean-square error, *RMS(k)*, at the kth iteration,

$$RMS(k) = \sqrt{\frac{1}{N}\sum_{i=1}^{N}(h_i^k - g_i)^2} \tag{4.5}$$

and the maximum deviation, *MAXD(k)*, at the kth iteration,

$$MAXD(k) = \max_{1 \le i \le N} \left| h_i^k - g_i \right|, \tag{4.6}$$

where g_i is the measured anomaly at the ith point, and N is the total number of data points.

This inverse approach is the same as the inverse approach for a constant density contrast model. The iterative improvement to the depth to the interface should cause reduction in both of these errors, and the errors are minimized as the solution converges (see Figure 3-2). The only difference is Equation (4.2) is used to calculate the anomaly caused by the density interface rather than Equation (3.1a). In practice, a given iteration may not reduce both errors simultaneously because the modifications to the model are approximate. Iteration continues until no further improvement in either error is realized or when *RMS* reaches the accuracy threshold of the observational data.

The uniqueness of the derived model of depth to the top of the layer is also restricted by the uncertainty in the assumed exponential density contrast model and the assumed average depth to this interface. Clearly, reduction in the assumed exponential density contrast (or increase in average depth to interface) increases topographic relief on the calculated surface. Appropriate solutions are possible only when the initial parameters are constrained by other geological or geophysical information.

4.5. Synthetic Example

Utility of the method can be demonstrated using synthetic data. Synthetics are also used to debug the computer program. In this section, I will invert the synthetic gravity anomaly, which is due to the exponential density model in Equation (4.3) and shown in Figure 4-4, into an equivalent density interface.

$\Delta\rho$ is defined in Equation (4.3), which is the value of density contrast of the synthetic model, and ZB = 10,000 m. I initialize the model ZT = 800 m. RMS and $MAXD$ of the initial model are 0.8 mGal and 4.3 mGal, respectively. After 10 iterations, RMS is reduced to 0.07 mGal (2% of the maximum anomaly) and $MAXD$ is reduced to 0.41 mGal. The final equivalent interface ZT is shown in Figure 4-6. The edge locations, thickness of the rectangular solid, and depth to top and bottom of the solid are well determined. It took only 66 CPU seconds on a Data General MV20000 to invert the gravity data with the exponential density contrast model.

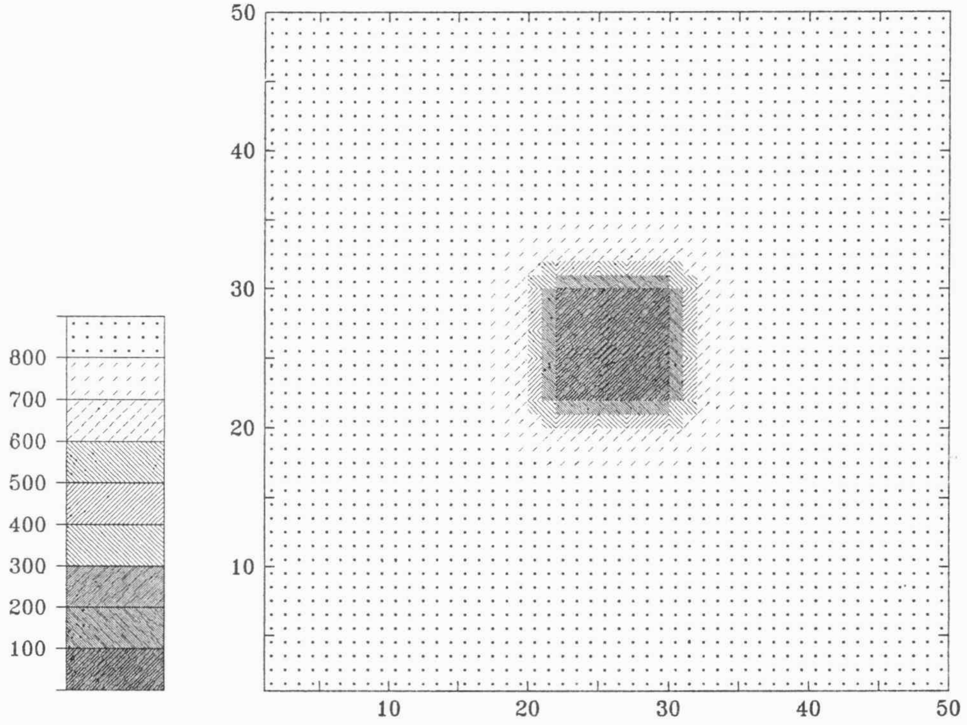

Figure 4-6. The equivalent interface inverted from the gravity anomaly shown in Figure 4-4 by the approach developed in Chapter 4. The exponential density contrast model is Equation (4.3). The shading interval is 100 m. The unit in both x and y directions is a station spacing, 100 m.

CHAPTER 5

KANSAS GEOLOGY FROM POTENTIAL-FIELD DATA

5.1. Introduction

In this chapter, I will apply the approaches developed in the last two chapters to gravity and magnetic data in Kansas. A model of the upper Precambrian lithology will be presented by inverting potential-field data to the density/magnetization distribution and a set of mapping conditions. A "modified" granitic boundary, across central Kansas between the 1,600-1,700 Ma mesozonal granitic terrane to the north and a younger, approximately 1,400 Ma epizonal granitic terrane to the south, will be determined by the model of the Precambrian lithology. Areal extent of the MRS and a structural zone associated with the MRS will also be proposed based on the model of the Precambrian lithology. Finally, I will use both a constant density contrast model and an exponential density contrast model to determine the depth to the Moho discontinuity. The depth to the Moho inverted from gravity data will be constrained by the seismic results.

5.2. Postulated Rock Types in the Basement

I apply the approaches developed in Chapter 3 to the potential-field data of Kansas in this section. First, two applications give the density and magnetization distributions in the Precambrian basement, which are inverted from the residual anomalies. I then use these results and the known geological information to determine possible types of rocks in the basement.

5.2.1. Density/magnetization contrast

In order to model potential-field anomalies caused by this physical interface, I calculated the weighted average density of the rocks above the Precambrian basement. Table 5-1 shows the approximate percentages of thickness of various sedimentary rock types above the Precambrian basement (Newell et al., 1987) and the bulk density of the rocks (Carmichael, 1989, p. 162-173; and Garland, 1979, p. 189). The weighted average density based on Table 5-1 is 2.39 g/cm^3. I assume that the rocks of the Precambrian basement would mostly be granitic, the average density of the basement was chosen as 2.66 g/cm^3 (Carmichael, 1989, p. 162). Therefore, the density contrast of the interface would be 0.27 (= 2.66 - 2.39) g/cm^3.

I also assume that the granitic rocks in the basement contained one percent of magnetite with the effective susceptibility $k = 0.25$ (*CGSM* unit) magnetized by the earth field of $H = 0.5$ Oe should have an intensity of magnetization approximately $M = Hk = 0.5 \times 0.01 \times 0.25 = 125$ nT (or $125 \times 10^{-9} / 4\pi \times 10^{-7} \cong 0.1 A/m$), which is an order-of-magnitude figure for polarization of basement rocks commonly used in magnetic model calculations (Nettleton, 1976, p. 362-363). Because sedimentary rocks are commonly nonmagnetic, I use 125 nT as the magnetization in modeling the magnetic interface.

Table 5-1. Percentages of thickness and density of sedimentary rocks above the basement.

Rocks	Density (g/cm^3) *	Percentages **
Limestone	2.34	41
Dolomite	2.78	17
Shale	2.35	23
Sandstone	2.22	16
Chalk	2.23	3

* *Information base on Carmichael (1989, p. 162-173) and Garland (1979, p. 189).*
** *Information based on Newell et al. (1987).*

5.2.2. Anomalies due to the relief of the basement

After determining these physical parameters, the calculation of the modeled anomalies due to the topographic relief of the Precambrian basement is by Equations (3.1). The depth to the Precambrian is controlled and modeled by the map of Configuration of the top of the Precambrian rocks in Kansas (Figure 1-1, Cole, 1976) and more than 3,400 well data (Figure 1-2, Cole and Watney, 1985).

The magnetic anomaly caused by the topographic relief of the Precambrian basement is shown in Figure 5-1, which has an amplitude of around 200 nT, and is subtracted from the residual magnetic anomaly (Figure 2-23). The remaining anomaly is shown in Figure 5-2. Based on the assumptions of the field separation mentioned in the end of Chapter 2, the residual magnetic anomaly (Figure 2-23) is caused by two kinds of geological sources: the topographic relief of the Precambrian basement and lithologic variation in the Precambrian basement rocks. Therefore, Figure 5-2 shows the magnetic anomaly only caused by the lithological change in the Precambrian basement rocks (the residual magnetic anomaly (Figure 2-23) minus the modeled anomaly due to the topographic relief of the Precambrian basement (Figure 5-1)). The gravity anomaly caused by the topographic relief of the Precambrian basement is shown in Figure 5-3, which has an amplitude of around 22 mGal, and is subtracted from the Bouguer anomaly (Figure 2-20). The remaining anomaly is shown in Figure 5-4. Again, based on the assumptions of the field separation, Figure 5-4 shows the gravity anomaly solely due to lithologic variation in the Precambrian basement (the residual gravity anomaly (Figure 2-20) minus the modeled anomaly due to the topographic relief of the Precambrian basement (Figure 5-3)).

5.2.3. Magnetization distribution in the basement

In this subsection, I invert the residual magnetic anomaly (Figure 5-2) caused by lithological variation in the Precambrian basement. This is case 2 in Chapter 3 to determine the magnetization distribution within a given layer. The total gridded data points are 408 × 205.

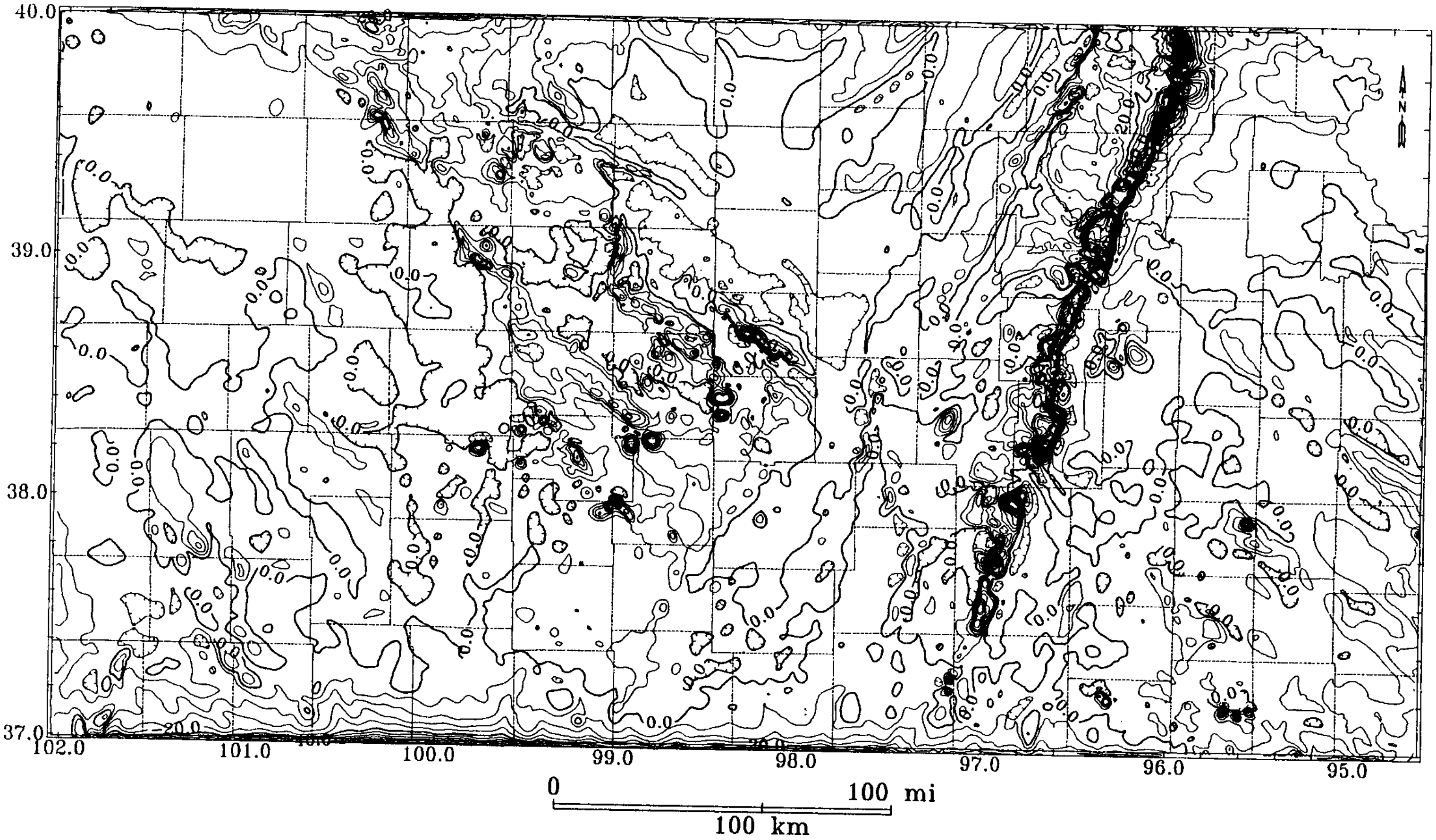

Figure 5-1. The magnetic anomaly caused by the topographic relief of the Precambrian basement. The magnetization contrast is assumed as 125 nT. Contour interval is 5 nT. Coordinates in *x* and *y* directions are degrees of longitude and latitude, respectively.

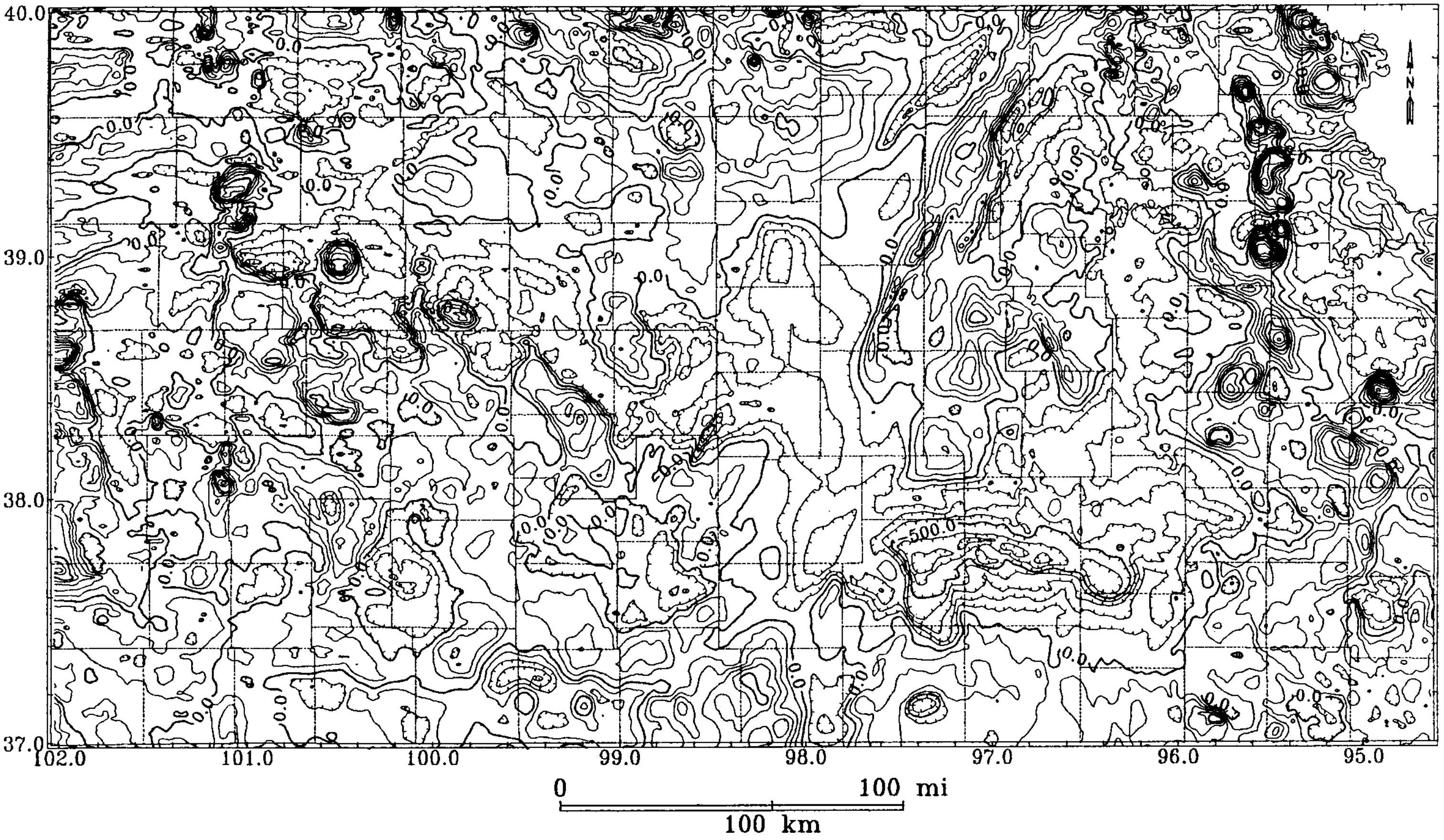

Figure 5-2. The residual magnetic anomaly caused by the lithological change in the Precambrian basement, which is the remains of the anomaly in Figure 5-1 subtracted from the residual anomaly in Figure 2-23. Contour interval is 100 nT. Coordinates in *x* and *y* directions are degrees of longitude and latitude, respectively.

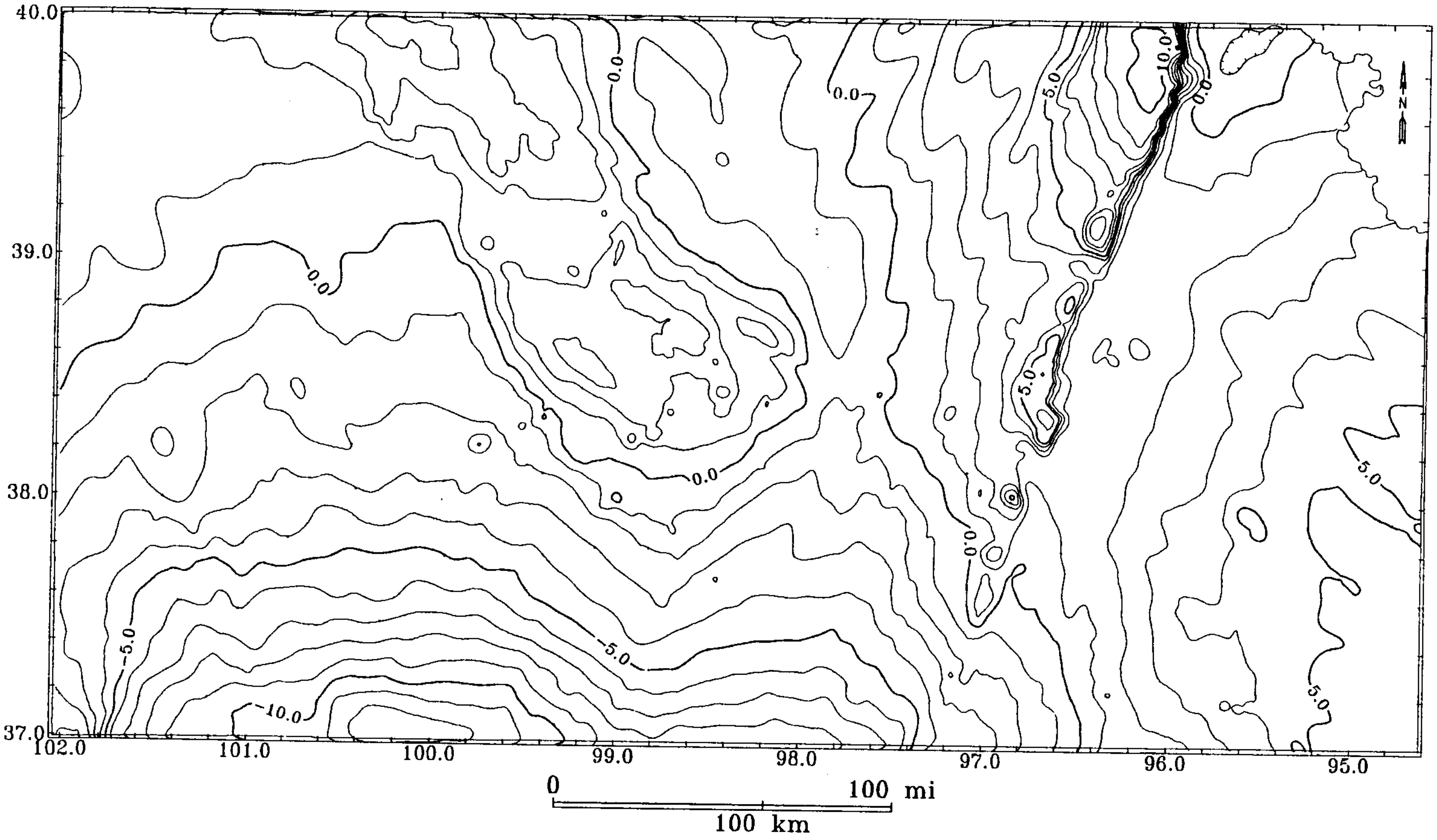

Figure 5-3. The gravity anomaly caused by the topographic relief of the Precambrian basement. The density contrast is assumed as 0.27 g/cm^3. Contour interval is 1 mGal. Coordinates in x and y directions are degrees of longitude and latitude, respectively.

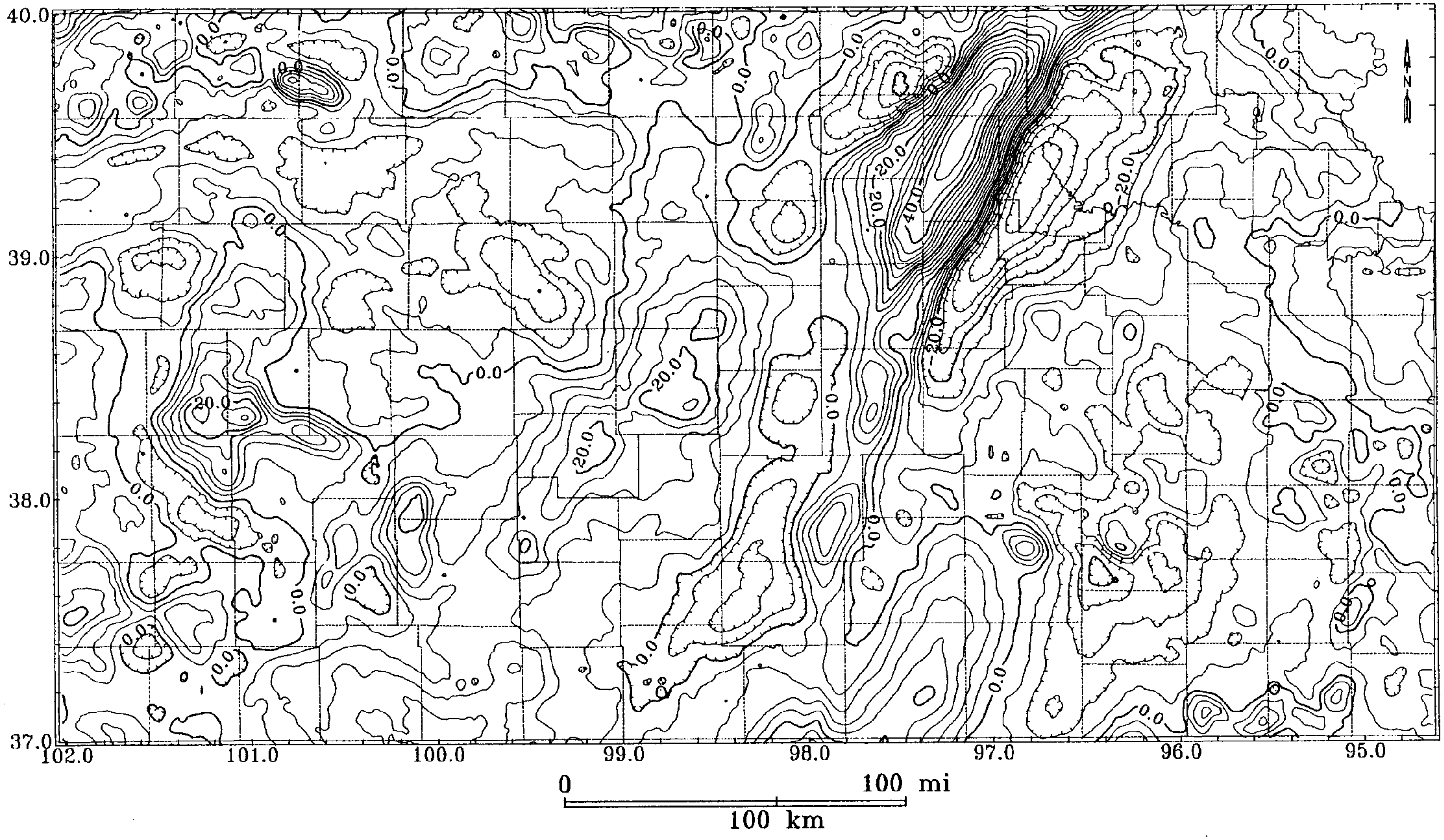

Figure 5-4. The gravity anomaly due to the lithological change in the Precambrian basement, which is the remains of the anomaly in Figure 5-3 subtracted from the residual anomaly in Figure 2-20. Contour interval is 4 mGal. Coordinates in *x* and *y* directions are degrees of longitude and latitude, respectively.

The top surface of the layer is defined by the digitized map of the top of the Precambrian rocks in Kansas (Cole, 1976) and more than 3,400 well data (Cole and Watney, 1985), which penetrate the Precambrian. The bottom surface of the layer is constrained to be parallel to the top surface. The thickness of the layer is chosen by trial-and-error. The thickness finally arrived at is 6 km, chosen because the magnetization distribution is consistent with the geological information shown in Figure 1-3. I initialize the magnetization of the layer to 125 nT. The inclination and declination of magnetization are chosen as 65 degrees and 7 degrees, respectively, which are the average values in Kansas.

The initial errors are RMS = 185 nT and $MAXD$ = 999 nT. Twenty iterations reduce the errors to RMS = 13 nT (1.3 % of the maximum real anomaly) and $MAXD$ = 67 nT. The calculations took 3,640 CPU seconds on a Data General MV20000. The final result, which represents the magnetization distribution within basement rocks, is shown in Figure 5-5. The modeled anomaly due to the magnetization distribution of Figure 5-5 is shown in Figure 5-6, which is confirmed by the residual magnetic anomaly in Figure 5-2.

5.2.4. Density distribution in the basement

In this subsection, I invert the residual gravity anomaly (Figure 5-4) caused by the lithologic variation in the Precambrian basement. This is case 4 in Chapter 3 to determine the density distribution within a given layer. The total gridded data points are 408×205.

The top surface is the same as for the magnetic inversion above. The bottom surface of the layer is again constrained as parallel to the top surface. The thickness of the layer is chosen by trial-and-error. A thickness of 2.7 km is chosen because the density distribution is consistent with the geological information shown in Figure 1-3. I initialize the density of the layer to 2.67 g/cm^3.

The initial RMS error and $MAXD$ are 11.7 mGal and 50.8 mGal, respectively. After ten iterations, RMS is reduced to 0.1 mGal (less than 0.2% of the maximum real anomaly), and $MAXD$ is reduced to 3.5 mGal. The calculations took 2,440 CPU

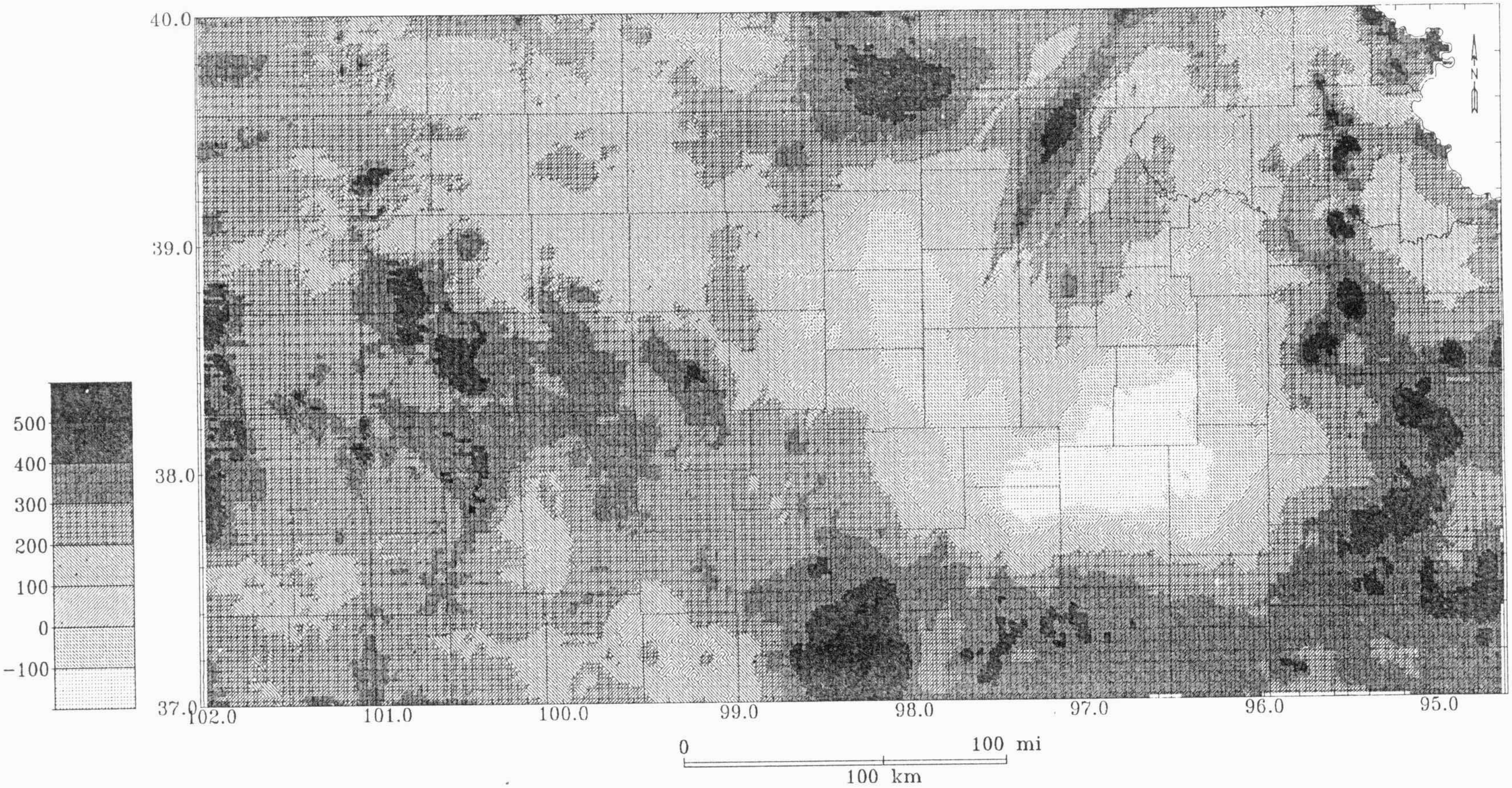

Figure 5-5. The magnetization distribution in the Precambrian basement. Shading interval is 100 nT. Coordinates in *x* and *y* directions are degrees of longitude and latitude, respectively.

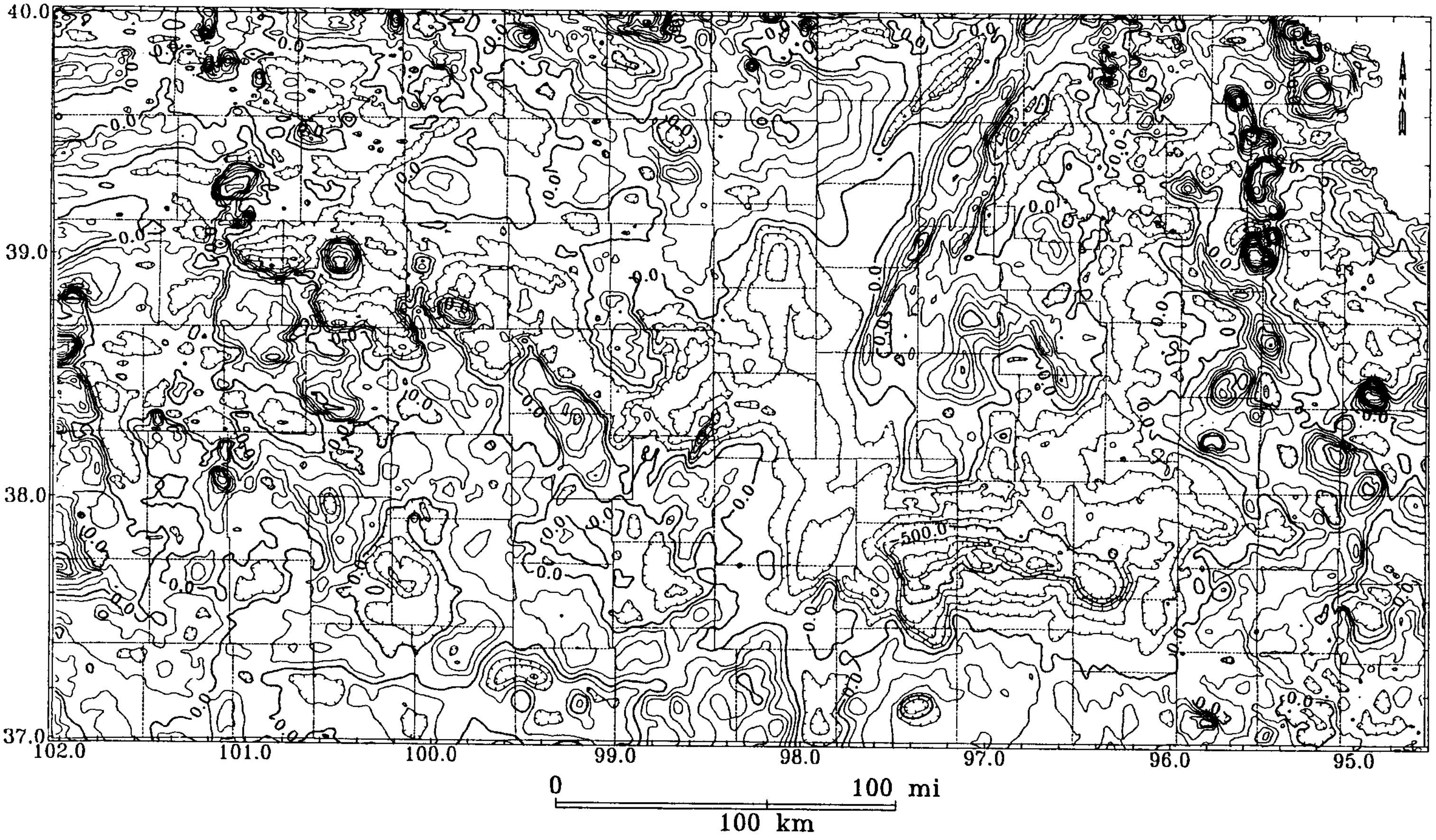

Figure 5-6. The magnetic anomaly due to the model of the magnetization distribution (Figure 5-5). Contour interval is 100 nT. Coordinates in x and y directions are degrees of longitude and latitude, respectively.

seconds on a Data General MV20000. The calculated density distribution is shown in Figure 5-7. The anomaly caused by the density distribution of Figure 5-7 is shown in Figure 5-8, which is confirmed by the residual gravity anomaly in Figure 5-4.

Inversion for the density distribution is a linear problem. Matrix methods, such as the singular-value-decomposition method (e.g., Xia, 1986), are thus appropriate for small data sets and give a full solution in one iteration. For large data sets such matrix inversion is impractical. The approach used here is an effective solution to this problem.

5.2.5. Postulated rock types in the basement

Density and magnetization are weak links between potential-field data and geology because different lithologies can have the same density or magnetization. This property makes interpretation of potential-field data difficult. On the other hand, density and magnetization are commonly functions of lithology. Therefore, knowledge of the density or magnetization distribution within a given layer should convey information about subsurface geology. In this subsection, I try to map the geophysical results, density and magnetization distributions, to rock types in the basement.

Some relationships between density/magnetization distribution and basement rock types can be determined by visually comparing the magnetization and density distribution maps (Figures 5-5 and 5-7) with the known geological information, map of basement rock types (Figure 1-3). Figure 5-9 shows the statistical relationship between density and three main rocks: granites, basalts (gabbro), and sandstone from Carmichael (1989, p. 163). Based on these relationships, I summarize the mapping parameters in Table 5-2, which allow me to estimate the rock types in the basement.

Figure 5-10 shows the postulated basement rock types in Kansas. It clearly shows the MRS trend (gabbro) almost south to the Kansas-Oklahoma border, the distinct boundary between north and south granitic terranes, and a structural zone associated with the MRS, which will be discussed following sections. It also shows the location of granitic plutons, which contain about 2% magnetite by weight (Steeples and Bickford, 1981).

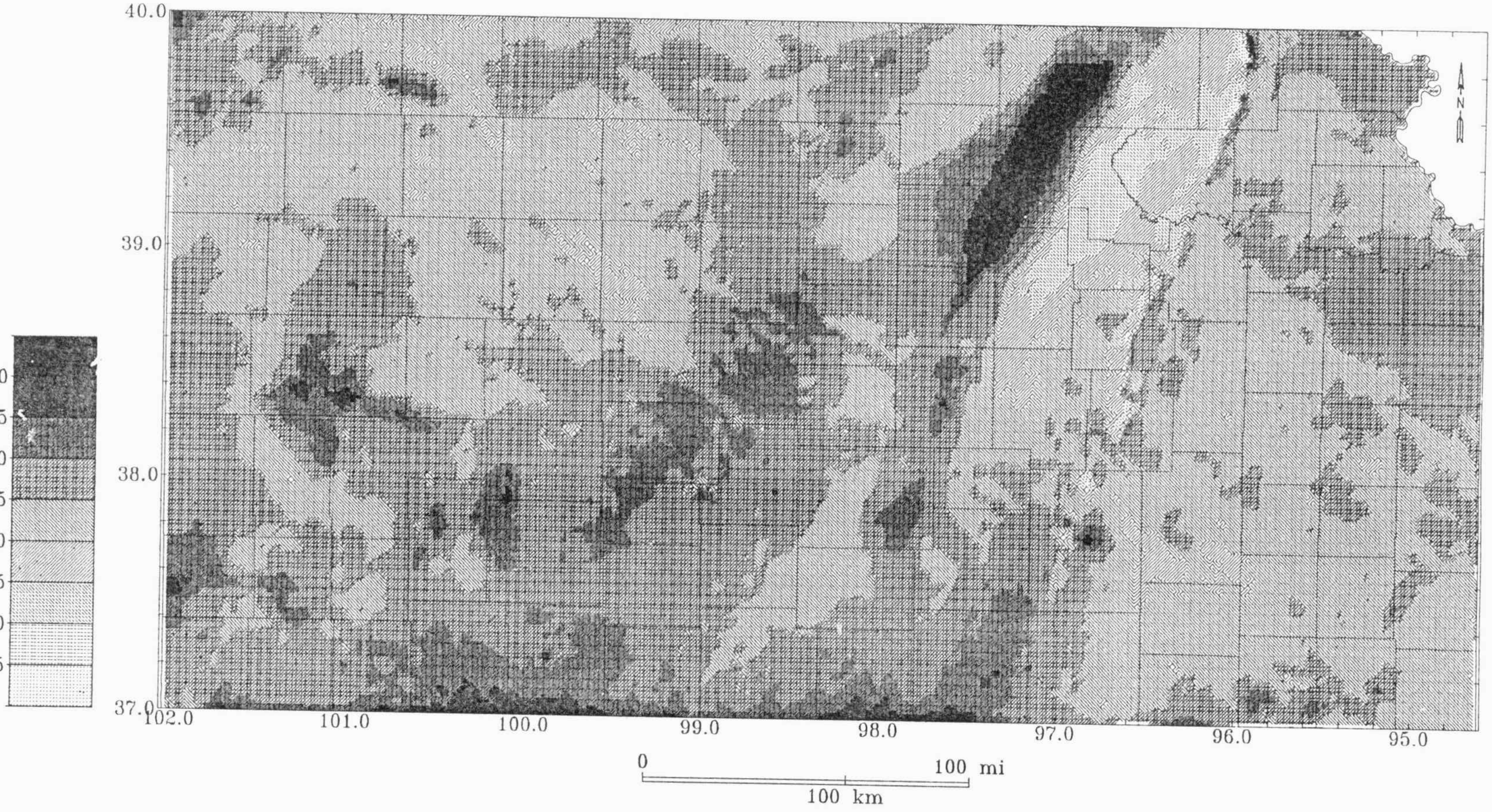

Figure 5-7. The density distribution in the Precambrian basement, inverse result of the residual anomaly shown in Figure 5-4. Shading interval is 0.15 g/cm^3. Coordinates in *x* and *y* directions are degrees of longitude and latitude, respectively.

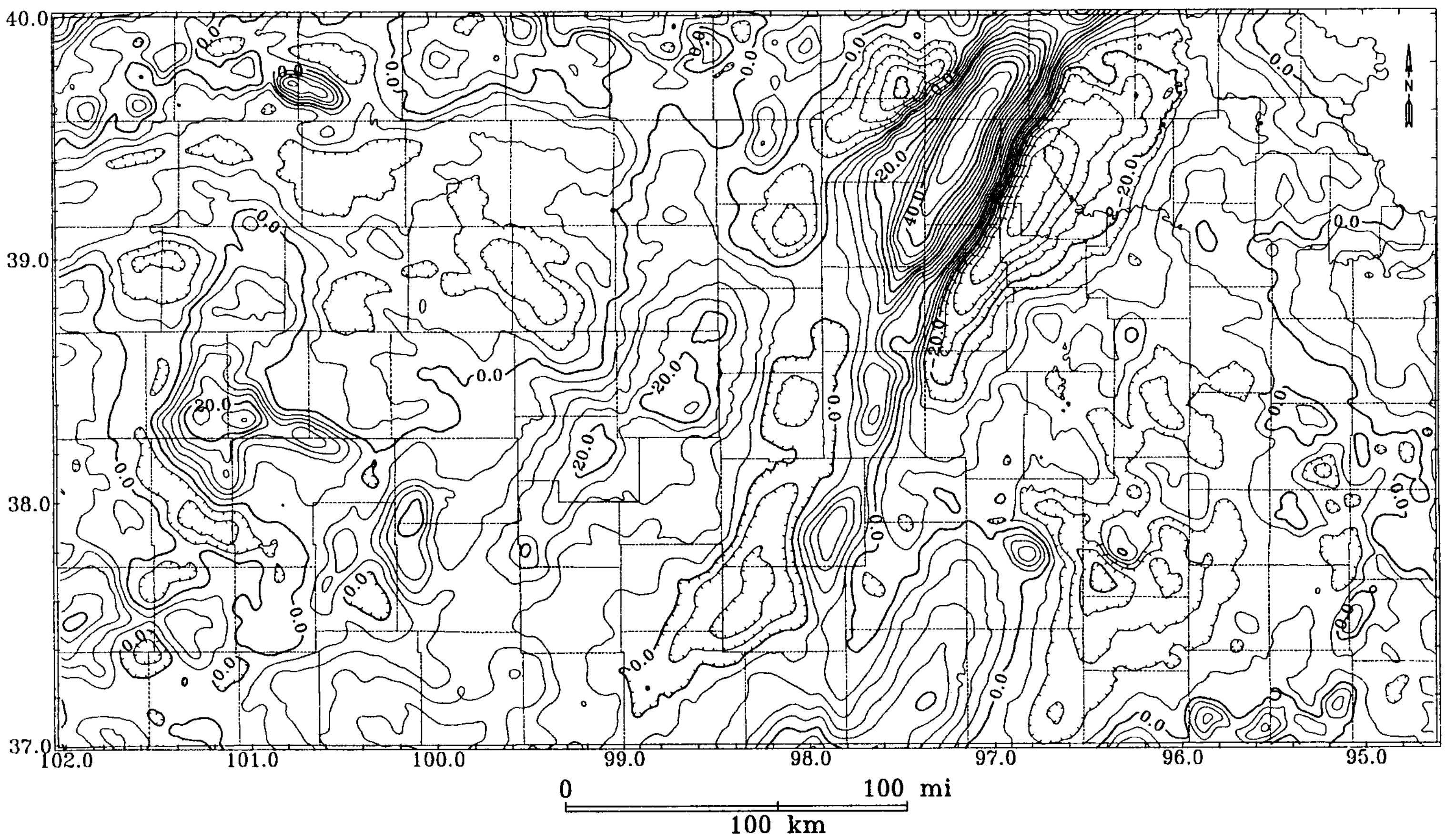

Figure 5-8. The modeled gravity anomaly due to the model of density distribution (Figure 5-7). Contour interval is 4 mGal. Coordinates in *x* and *y* directions are degrees of longitude and latitude, respectively.

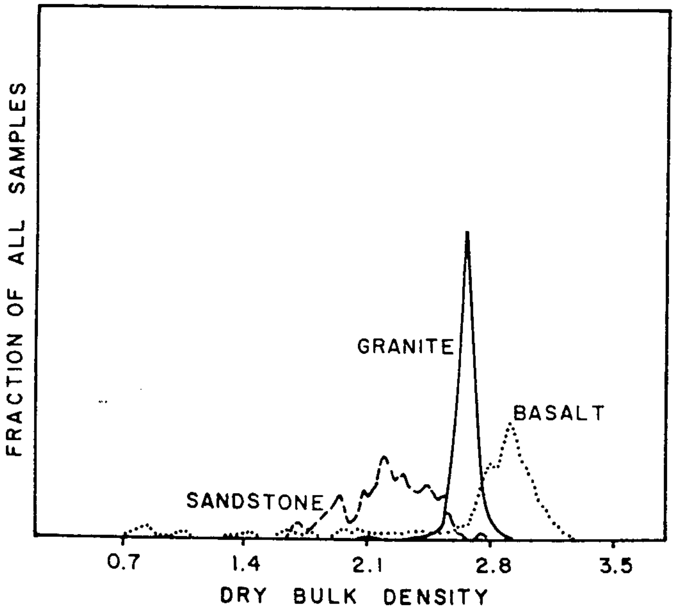

Figure 5-9. Comparison of frequency distributions of dry bulk densities of granites, basalts, and sandstone. After Carmichael (1989, p. 163).

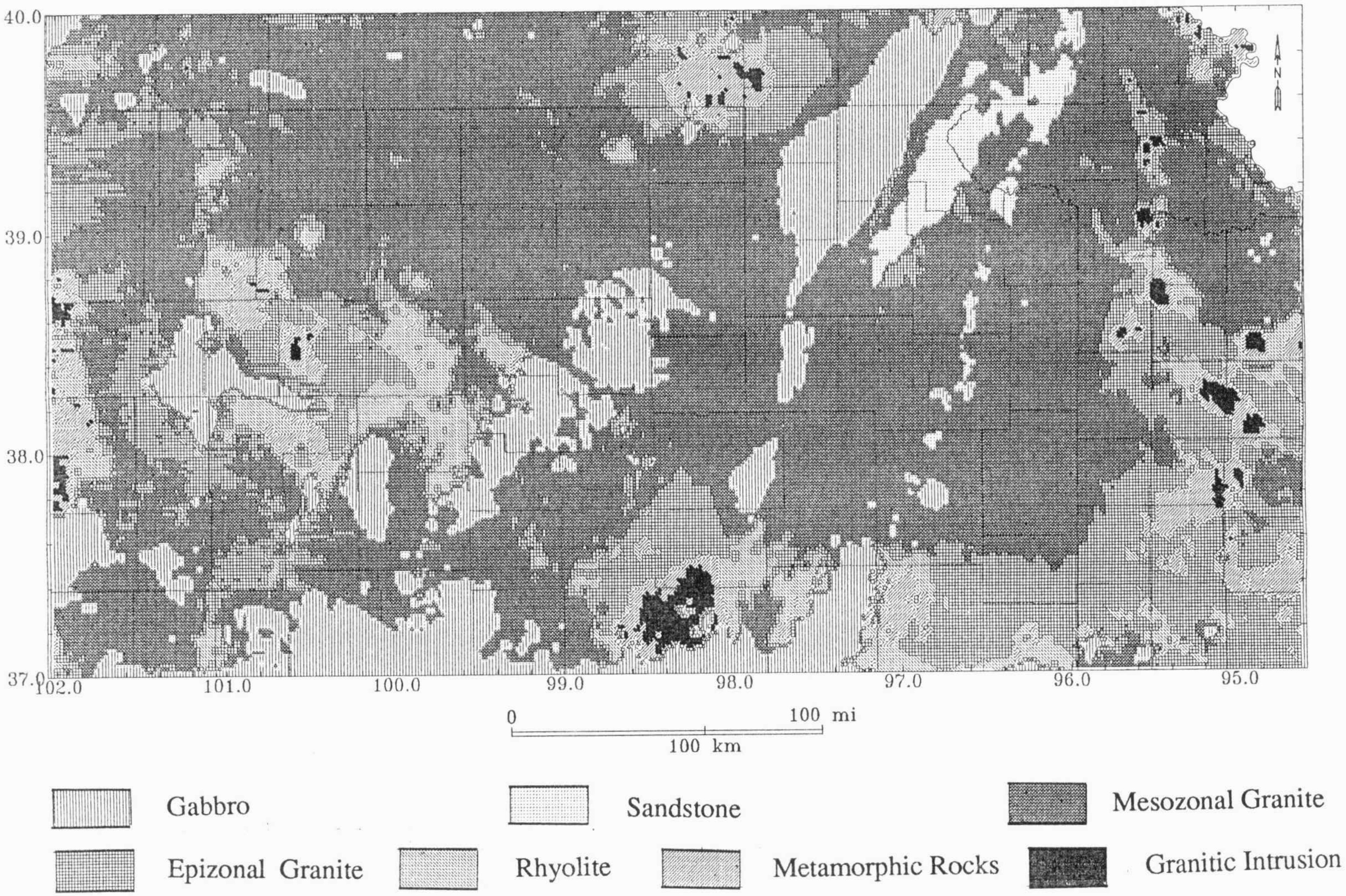

Figure 5-10. Postulated rock types in the basement of Kansas, based on the inverse results of potential-field data. Coordinates in x and y directions are degrees of longitude and latitude, respectively.

Table 5-2. Mapping conditions from potential-fields to rock types.

Rocks	Density (g/cm^3)	Magnetization (nT)
Gabbro	Larger than 2.80	
Sandstone	Less than 2.35	
Mesozonal Granite	2.35 -- 2.65	Less than 150
Epizonal Granite	2.35 -- 2.65	150 --300
Rhyolite	2.65 -- 2.80	200 -- 275
Metamorphic Rocks	2.30 -- 2.80	275 -- 350
Granitic intrusion	2.30 -- 2.80	Larger than 350

The horizontal resolution in Figure 5-10, as well as Figures 5-5 and 5-7, are related to several factors, including depth to source bodies, distances between source bodies, and distance between the measurement points, as well as non-uniqueness in the inverse solution. Thus, a general specification of horizontal resolution in these maps cannot be made. A sharp geologic boundary produces a potential field boundary which is smeared over a distance equal to about twice the depth of burial of the source body. This is confirmed by the synthetic results (Figures 3-4, 3-5, 3-7, and 3-8). In this context, the horizontal resolution in Figure 5-10 would be 6-10 km (4-6 mi).

5.3. 1,600 Ma/1,400 Ma Granitic Boundary

Yarger (1985) proposed a distinct east-west trending boundary across central Kansas between the 1,600-1,700 Ma mesozonal granitic terrane to the north and a younger, about 1,400 Ma epizonal granitic terrane to the south (Figure 1-5). Based on the model of the Precambrian lithology (Figure 5-10), I would draw a "modified" granitic boundary in Figure 5-11. The "modified" boundary is coincident with Yarger's result in most areas, except for southeastern Kansas. The boundary proposed by Yarger is located in Woodson, Allen, and Bourbon Counties in southeastern Kansas, which is coincident with one of the rock boundaries in Bickford et al.'s results (1981). The "modified" boundary is located in Osage, Franklin, and Miami Counties, which is coincident with the other boundaries in Bickford et al.'s result.

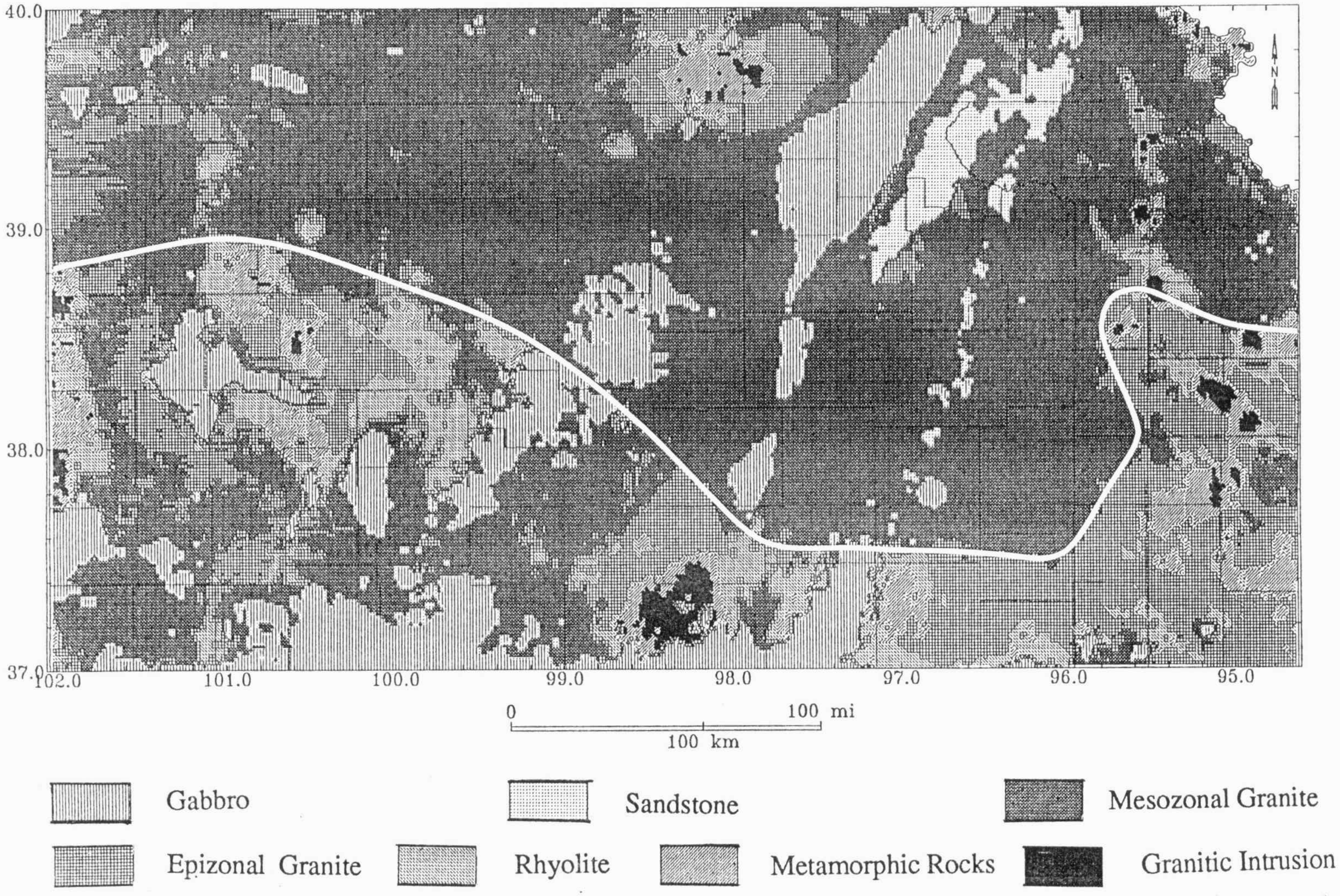

Figure 5-11. A "modified" granitic boundary (in the white line) based on the map of postulated rock types in the basement of Kansas.

Unfortunately, the rocks between the two rock boundaries in Bickford et al.'s result are unknown. The "modified" boundary is only indicated by potential-field data. This is the reason for the quotes around modified.

5.4. Areal Extent of MRS and Structural Zone Associated with MRS

In Figure 5-12, I highlight two groups of gabbro in Kansas based on the model of the Precambrian lithology and structural zone associated with the MRS (Figure 5-10). One group is located north of the east-west trending granitic boundary. The other is south of the granitic boundary, along the Kansas-Oklahoma border. Lines of A-A' and B-B' define a structural zone associated with the MRS. The line A-A' is based on the appearances of gabbro. The line B-B' is actually the Humboldt Fault.

Clearly, the MRS continues along a southwestern trend to at least the granitic boundary. The MRS does not terminate in central Kansas but continues along a southwestern trend to at least the Kansas-Oklahoma border. The occurrence of gabbro in the region bounded by A-A' and B-B' supports Yarger's conclusion (Figure 1-5).

As shown above, the results from the quantitative analysis (inversion) of potential-field data are confirmed by the qualitative analysis (filtering) of potential-field data and known geology.

5.5. Depth to the Moho Discontinuity

In this section, I will use the approaches developed in Chapters 3 and 4 to invert regional Bouguer gravity to the depth to the Moho discontinuity. These applications provide a smoothed representation of the topography of the Moho discontinuity in Kansas. Both constant density and exponential density contrast models are determined and used in the inverting procedures . The inverted results are controlled by the results from seismic refraction data (Steeples and Miller, 1989).

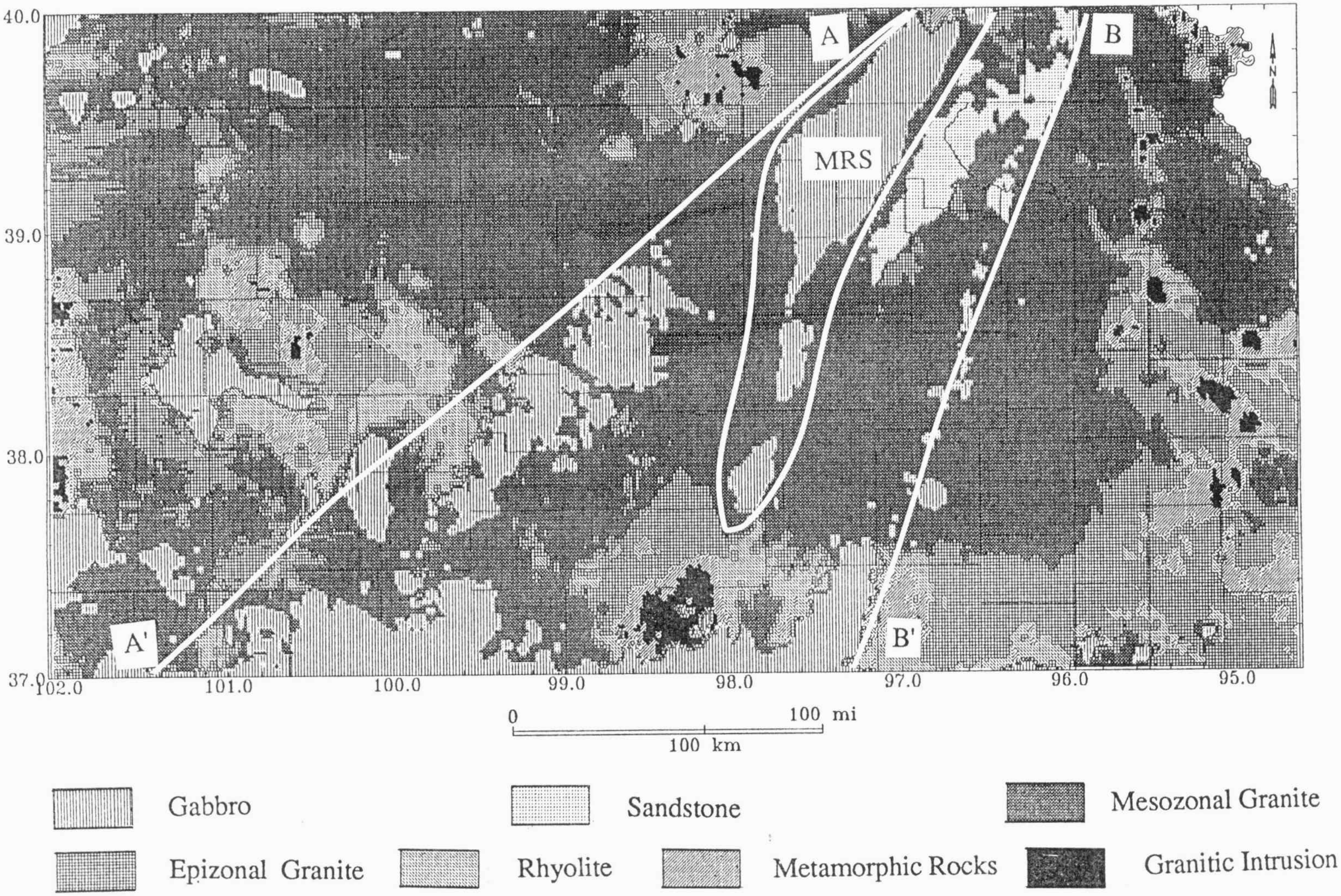

Figure 5-12. Areal extent of MRS and structural zone associated with MRS (lines A-A' and B-B') based on the map of postulated rock types in the basement of Kansas.

5.5.1. Depth to the Moho based on a constant model

I use the approach developed in Chapter 3 to invert the regional gravity anomaly (Figure 2-19), which is assumed due to the Moho discontinuity. This is case 3 to determine the density interface. The total gridded data points are 408 × 205.

In this case, any value could be depth to the bottom of a layer if it is larger than *ZT*. I define the density contrast as 0.657 g/cm^3, which is very close to conventional values for the crust 2.67 g/cm^3 and the upper mantle 3.35 g/cm^3. The initial top interface of the layer is defined by trial-and-error. Because the final result is constrained by seismic refraction, I can choose different depths until the final inverse model agrees with the seismic result along the two-dimensional profile. The depth I finally determine is 37.4 km.

The initial *RMS* error and *MAXD* are 25.7 mGal and 76.8 mGal, respectively. After three iterations, *RMS* is reduced to 1.0 mGal (1.3% of the maximum real anomaly), and *MAXD* is reduced to 11.3 mGal. The calculations took 529 CPU seconds on a Data General MV20000. The calculated depth to the Moho, which is a smooth representation of the topography of the Moho, is shown in Figure 5-13. The modeled anomaly is shown in Figure 5-14, which is confirmed by the regional gravity anomaly in Figure 2-19. Based on the inverse result from gravity data, the depth to the Moho at Concordia, Kansas is 36 km (23 mi), which is coincident with the result from seismic refraction. At the intersection of the Kansas - Colorado border and seismic profile is 42.5 km (26.4 mi), which also coincides with the result from the seismic refraction (42 km). The inverse result from gravity data looks reasonable, but there are clearly some edge effects caused by the Gibbs phenomenon in the Fourier transform.

5.5.2. Depth to the Moho based on an exponential model

In this subsection, I try to invert the regional gravity anomaly (Figure 2-19) into the depth to the Moho discontinuity by the approach discussed in Chapter 4. I assume that the density of the crust is an exponential function with respect to depth. The inverse result can be checked by the results from seismic refraction shown in Figure 1-7. I can adjust the exponential density model and the average depth to the Moho by

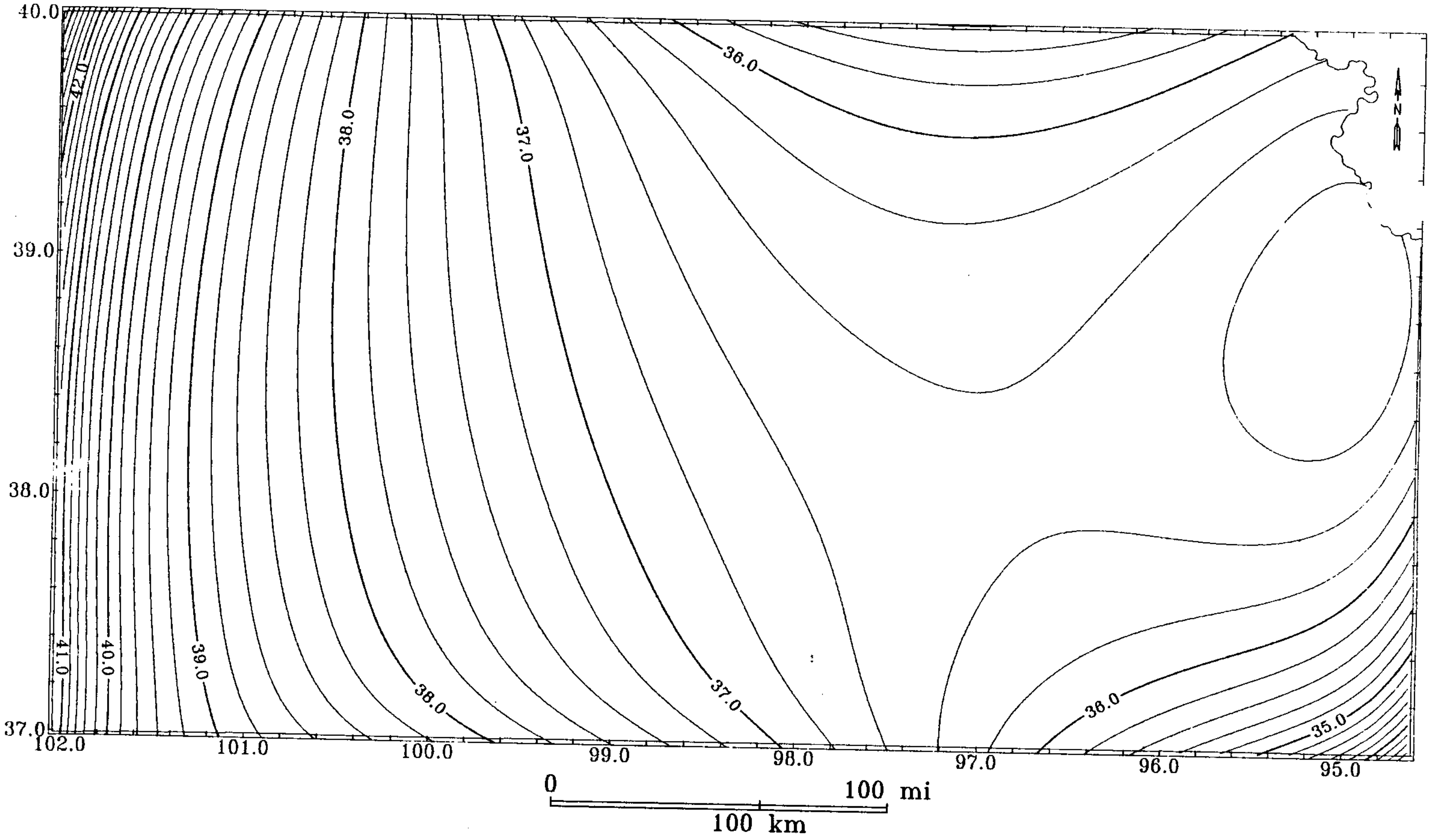

Figure 5-13. The depth to the Moho discontinuity, inverse results of the regional gravity (Figure 2-19) Contour interval is 0.2 km. Coordinates in *x* and *y* directions are degrees of longitude and latitude, respectively.

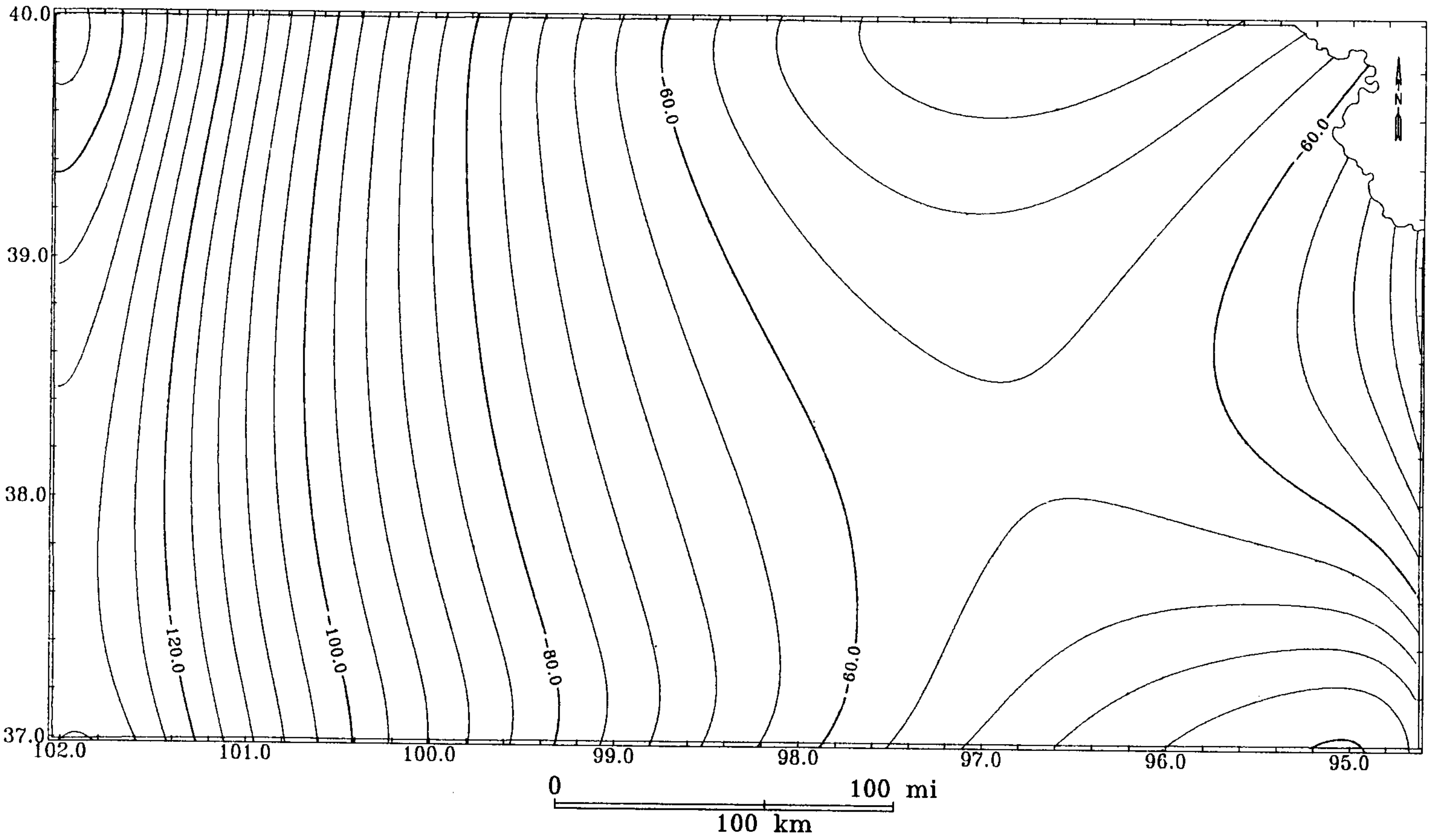

Figure 5-14. The modeled gravity anomaly due to the model of the depth to the Moho discontinuity (Figure 5-13). Contour interval is 4 mGal. Coordinates in x and y directions are degrees of longitude and latitude, respectively.

comparing the result from the inverse approach and the results from seismic refraction by trial-and-error. I choose the exponential density contrast model and the average depth to the Moho which produce the best coincidence between the results from the gravity inversion and seismic refraction.

The best solution for the average depth to the Moho is 37.0 km and the best exponential density contrast model is

$$\Delta\rho(z) = -1.0e^{-0.0187z} \text{ g/cm}^3, \tag{5.1}$$

where the unit of depth z is km. This density model indicates a density contrast at the surface of -1.0 g/cm^3 and at the average depth 37.0 km (23.0 mi) of -0.50 g/cm^3. These figures give a density at the surface of 2.35 g/cm^3 and at depth 37.0 km of around 2.85 g/cm^3. The average density contrast can be determined by

$$\Delta\overline{\rho} = \frac{1}{37.0}\int_{0}^{37.0} -1.0e^{-0.0187z}dz = -0.72 \text{ g/cm}^3. \tag{5.2}$$

Therefore, the average density of the crust is 3.35 - 0.72 = 2.63 g/cm^3, which is a little lower than the conventional density for continental crust 2.67 g/cm^3. The reason for this is that the higher density contrast at the surface increases the average density contrast for the whole crust. Both density values at the surface and at a depth of 37.0 km, however, are geologically reasonable.

Given a lower interface at ZB = 100 km, an initial guess for ZT is 37.0 km. The initial errors are RMS = 25.7 mGal and $MAXD$ = 76.8 mGal. Five iterations reduce the errors to RMS = 0.8 mGal (1.0% of the maximum real anomaly) and $MAXD$ = 11.5 mGal. The calculations took 824 CPU seconds on a Data General MV20000 (529 CPU seconds are needed in three iterations for the constant density model in the last subsection, thus, CPU time used per iteration is largely model independent). The final result, which represents the depth to a smoothed surface of the Moho, is shown in Figure 5-15. The gravity anomaly caused by the modeled Moho is

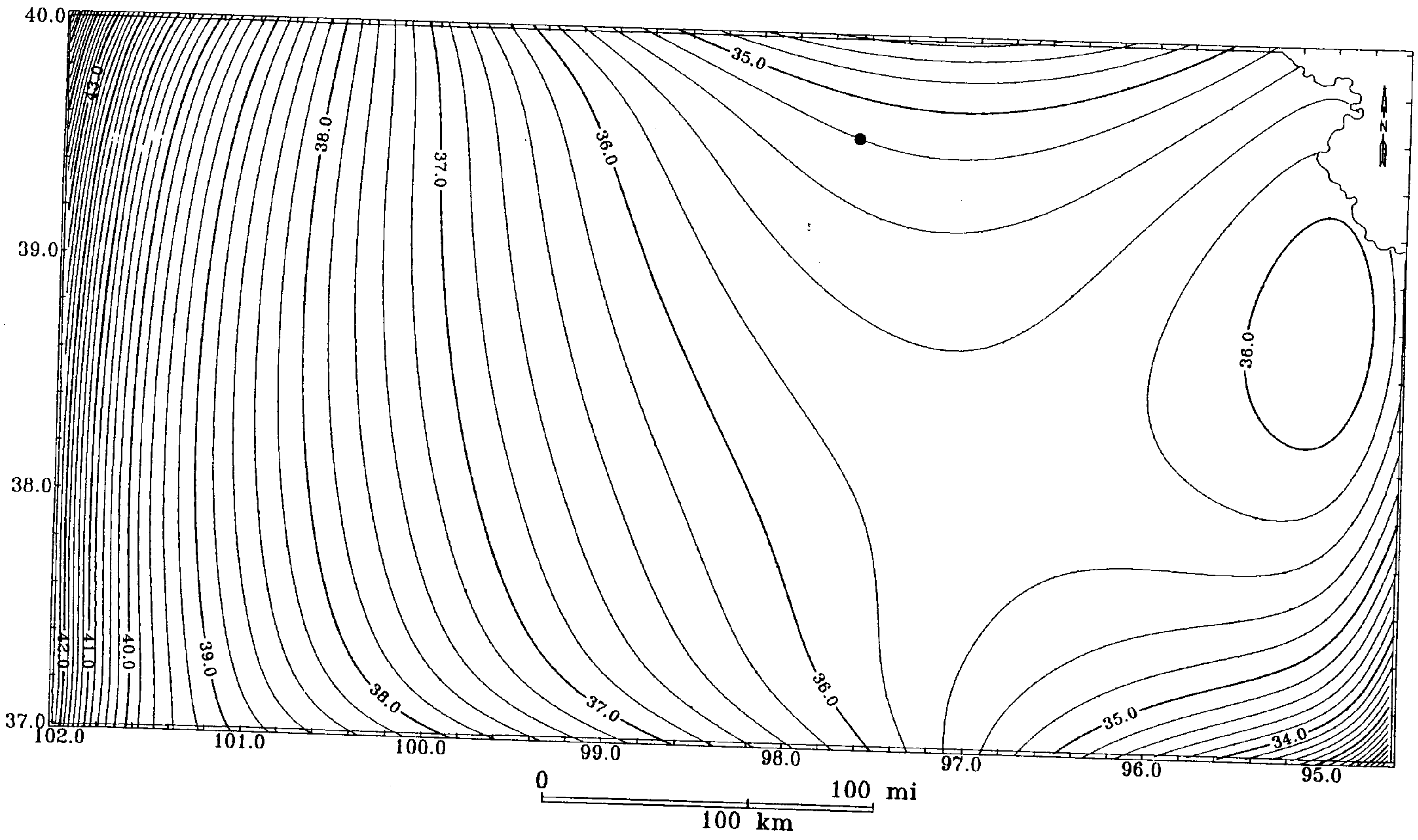

Figure 5-15. The depth to the Moho discontinuity calculated by the inverse approach developed in Chapter 4. Contour interval is 0.2 km. The black spot shows the location of Concordia, Kansas. Coordinates in *x* and *y* directions are degrees of longitude and latitude, respectively.

shown in Figure 5-16, which reproduces the regional Bouguer anomaly (Figure 2-19). Based on the inverse result from gravity data, the depth to the Moho at Concordia, Kansas is 35.2 km (21.9 mi), which is 0.8 km shallower than the result from the seismic refraction. The depth to the Moho at the intersection of the Kansas - Colorado border and the seismic refraction profile is 43.5 km (27.0 mi), which is about 1 km deeper than the result from the seismic refraction. The inverse result from gravity data looks reasonable, but again there are edge effects caused by the Gibbs phenomenon of Fourier transformation.

Both inverse results (Figures 5-13 and 5-15), based on the constant density model and the exponential density model, respectively, coincide with the result from the seismic refraction data. The thinner crust in the area around 97.2 degrees longitude and 39.2 degrees latitude is the area postulated by Miller (1983, see Figure 1-6) as high-velocity crust. Both gravity and seismic data suggest the presence of mantle material at fairly shallow depths in this region of the MRS. The other relative thin crust area is located in southeastern corner of Kansas, which is probably due to the Ozark Uplift (Greig, 1959; and Tanner, 1959).

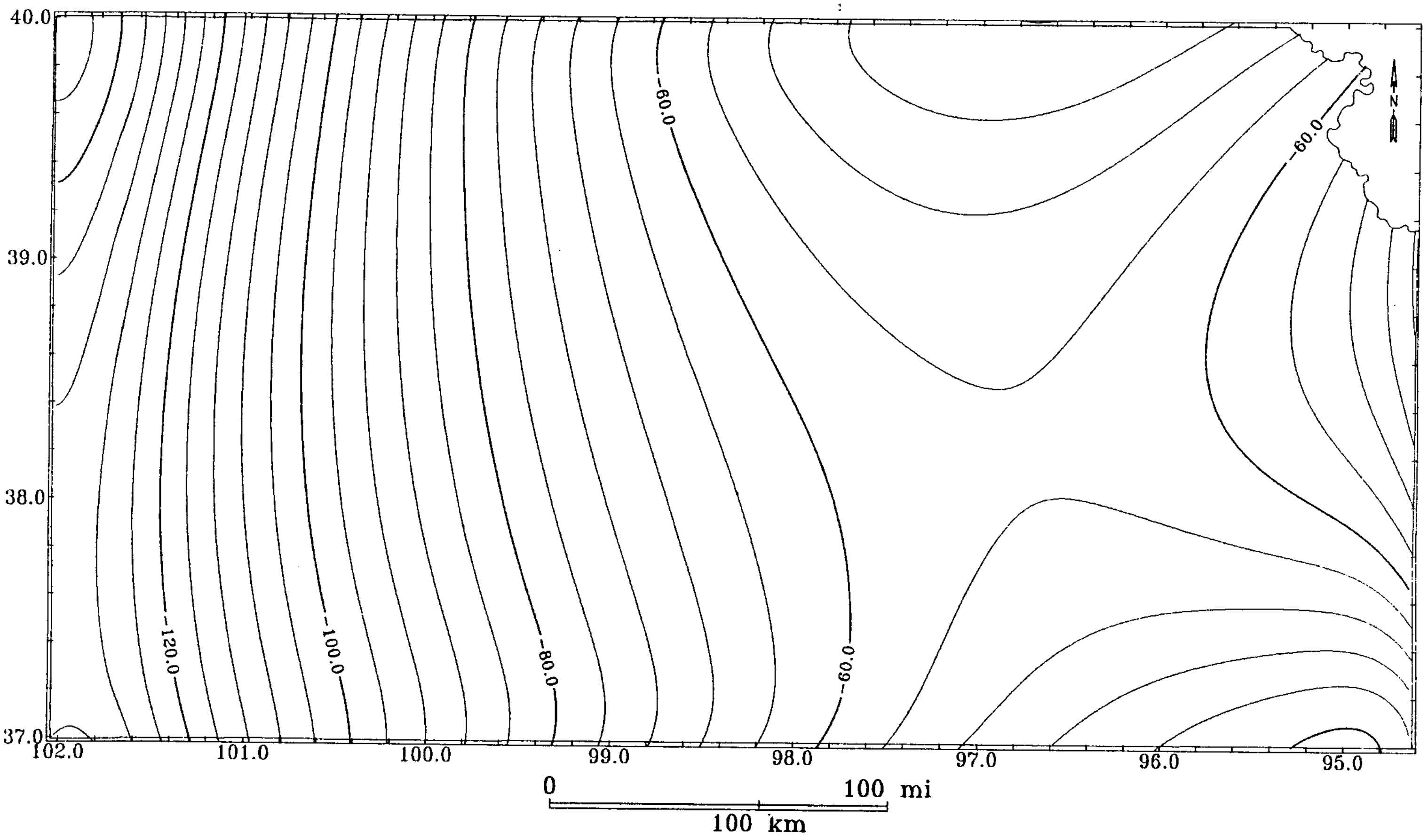

Figure 5-16. The gravity anomaly caused by the model shown in Figure 5-15. Contour interval is 4 mGal. Coordinates in *x* and *y* directions are degrees of longitude and latitude, respectively.

CHAPTER 6

CONCLUSIONS

The approach of correction of topographic distortions in gravity data developed in the spatial domain is useful in handling a relatively small set of data. The main advantages of the approach are fewer edge effects and ease of programming. The optimum depth, which can be determined by the criterion of smoothness between the data points, is a critical parameter. The disadvantage of the approach is the computer time needed for a relatively large set of data. In order to handle a large set of data, the Fourier-based approach is developed in this study. The main advantage of the approach is computational efficiency, which is demonstrated by processing the whole state potential-field data, which are gridded by kriging and contain 205×408 points (1.6 km by 1.6 km) and were not topographically corrected before this study. The accuracy of the approaches is demonstrated by synthetic examples.

The significance of the topographic distortions is shown by the results that the maximum elevation change in the gravity data up to 500 m causes the maximum correction in the gravity anomaly amplitudes up to 2.6 mGal. According to 0.1 mGal of the accuracy of gravity data, the topographic distortions in gravity data are not negligible, even though Kansas is thought to be very flat. The results for the aeromagnetic data are the maximum horizontal shifting of aeromagnetic anomaly up to 457 m with the maximum correction in aeromagnetic anomaly amplitudes up to 270 nT. Reduction to the horizontal plane must be done because of 3 nT of the accuracy of the magnetic data.

New approaches to inversion of potential-field data by iterative forward modeling developed in the study can determine one of two results: density (magnetization) distribution in a specified layer, and density (magnetic) interface. Because of the stability of the forward calculation, no particular filter is needed to produce convergence of the solution, and convergence can obtained from the worst initial model, a flat interface and/or constant density/magnetization.

The formula for calculating the gravity anomaly due to an exponential density contrast model derived in the study is a general formula which includes the constant density contrast model and the linear density contrast model. The constant and linear density contrast model are frequently used in inverting gravity data. Less computer time is needed for the exponential model than the linear model. The inverse approach based on the exponential model is presented.

The approaches are applied to topographically corrected data in Kansas. Based upon inverse models of the density and magnetization distribution, rock types in the Precambrian basement are inferred. The postulated rock distribution in the basement reflects known geological information. The modified east-west trending granitic boundary is consistent with known geology. The areal extent of MRS and the structural zone associated with MRS determined by the map of the postulated rock distribution confirm Yarger's results. The models of depth to the Moho discontinuity determined by the inverse approaches with both a constant density contrast model and an exponential density contrast model are constrained by the seismic results and reasonable in geology. The capability of inverting a large set of data by these approaches is clearly shown by the applications.

The unsolved problem in potential-field data processing is anomaly separation. In this study, I have assumed the potential-field anomalies can be separated and have also assumed the anomalous sources for the regional and residual anomalies. The assumptions seem acceptable from the results obtained by the inverse approach.

APPENDIX A

ORTHOGONAL-POLYNOMIAL FIT

Let $\varphi_1(x),\ \varphi_2(x),\ \cdots,\ \varphi_n(x),\ \cdots$ be a set of polynomials and subscript i is the order of the polynomial, let $w(x)$ be the weighting function. If

$$\left(\varphi_i(x),\varphi_j(x)\right)=\int_a^b w(x)\varphi_i(x)\varphi_j(x)dx\ =0,\quad (\mathrm{i}\neq\mathrm{j}),\tag{A.1}$$

then the polynomials $\varphi_i(x)$ and $\varphi_j(x)$ are orthogonal on the interval (a, b) with respect to the weighting function $w(x)$, and $\{\varphi_n(x)\}$ is called an orthogonal set of the polynomials. The orthogonal set of the polynomials can be constructed as follows (Cadwell, 1961; Clark et al., 1963).

a) $$\varphi_0(x)=1,\tag{A.2}$$

b) $$\varphi_{i+1}(x)=\left(x-\delta_{i+1}\right)\varphi_i(x)-\gamma_{i+1}^2\varphi_{i-1}(x),\tag{A.3}$$

where $\varphi_{-1}(x)$is defined as zero, and

$$\delta_{i+1}=\left(x\varphi_i(x),\varphi_i(x)\right)/\left(\varphi_i(x),\varphi_i(x)\right),\quad (i\geq 0),\tag{A.4}$$

$$\gamma_{i+1}^2=\left(\varphi_i(x),\varphi_i(x)\right)/\left(\varphi_{i-1}(x),\varphi_{i-1}(x)\right),\quad (\mathrm{i}\geq 1),\tag{A.5}$$

and γ_{i+1}^2 is zero for $i = 0$.

Suppose we have a set of orthogonal polynomials $\{\varphi\}=\{\varphi_r(x),r=1,2,\cdots,p\}$ and $\{\psi\}=\{\psi_s(y),s=1,2,\cdots,q\}$, we want to form an orthogonal polynomial

$$f(x,y)=\sum_{r=0}^{p}\sum_{s=0}^{q}\mu_{rs}\varphi_r(x)\psi_s(y)=\mu_{00}\varphi_0(x)\psi_0(y)+$$

$$\mu_{10}\varphi_1(x)\psi_0(y)+\mu_{11}\varphi_1(x)\psi_1(y)+\mu_{20}\varphi_2(x)\psi_0(y)+$$

$$\cdots+\mu_{pq}\varphi_p(x)\psi_q(y) \tag{A.6}$$

to fit the data set z_{ij}, where $i=1,2,\cdots, n$, n is the number of the data in x direction, and $j=1,2,\cdots, m$, m is the number of the data in y direction. The least-squares fit determines the coefficients μ_{rs} in Equation (A.6) which allow minimization of the function

$$\Phi=\sum_{i=1}^{n}\sum_{j=1}^{m}\left(f_{ij}-z_{ij}\right)^2 \tag{A.7}$$

where f_{ij} stands for $f\left(x_i,y_j\right)$. Taking derivatives of the function Φ with respect to μ_{rs} and letting them equal to zero, we obtain

$$\frac{\partial\Phi}{\partial\mu_{rs}}=2\sum_{i=1}^{n}\sum_{j=1}^{m}\left(f_{ij}-z_{ij}\right)\varphi_r(x_i)\psi_s\left(y_j\right)=0. \tag{A.8}$$

Because $\{\varphi\}$ and $\{\psi\}$ are the orthogonal polynomials, we can write

$$f_{ij}\varphi_r\psi_s=\mu_{rs}\varphi_r^2\psi_s^2. \tag{A.9}$$

Equation (A.9) allow us to solve the coefficients μ_{rs} for the orthogonal polynomial (A.6) by simple multiplications. We do not have to solve simultaneous equations as when using normal polynomial to fit the data. Based on Equation (A.9), we can write the coefficients μ_{rs} as

$$\mu_{rs}=\sum_{i=1}^{n}\sum_{j=1}^{m}z_{ij}\varphi_r(x_i)\psi_s\left(y_j\right)/\sum_{i=1}^{n}\sum_{j=1}^{m}\varphi_r^2(x_i)\psi_s^2\left(y_j\right)$$

$$=\sum_{j=1}^{m}\psi_s\left(y_j\right)\left[\sum_{i=1}^{n}z_{ij}\varphi_r(x_i)\right]/\sum_{i=1}^{n}\varphi_r^2(x_i)\sum_{j=1}^{m}\psi_s^2\left(y_j\right)$$

$$= \sum_{j=1}^{m} \psi_s(y_j)\lambda_{rj} / \beta_s, \qquad \text{(A.10)}$$

where

$$\beta_s = \sum_{j=1}^{m} \psi_s^2(y_j),$$

and

$$\lambda_{rj} = \sum_{i=1}^{n} z_{ij}\varphi_r(x_i) / \sum_{i=1}^{n} \varphi_r^2(x_i).$$

Equation (A.10) gives the coefficients for the orthogonal polynomial (A.6) with unit weighting functions.

APPENDIX B

CONVERGENCE OF POWER SERIES IN EQUATION (2-10)

I rewrite Equation (2-10)

$$g(\vec{k}) = 2\pi G\sigma(\vec{k})e^{-|\vec{k}|z_0}\sum_{n=0}^{\infty}\frac{\left[-|\vec{k}|h(\vec{r})\right]^n}{n!} . \tag{B.1}$$

Let $R = \max|\sigma(\vec{r})|$, then $|\sigma(\vec{k})| \le RA$, where A is the area covered by a data set. With $H = \max|h(\vec{r})|$, then

$$\begin{aligned} g(\vec{k}) &= 2\pi G\sigma(\vec{k})e^{-|\vec{k}|z_0}\sum_{n=0}^{\infty}\frac{\left[-|\vec{k}|h(\vec{r})\right]^n}{n!} \\ &\le 2\pi GAR\sum_{n=0}^{\infty}\frac{\left(H|\vec{k}|\right)^n}{n!}e^{-|\vec{k}|z_0} \\ &= 2\pi GAR\sum_{n=0}^{\infty}L_n , \end{aligned} \tag{B.2}$$

where

$$L_n = \frac{\left(H|\vec{k}|\right)^n}{n!}e^{-|\vec{k}|z_0} = \frac{\left(H|\vec{k}|\right)^n / n!}{\sum_{j=0}^{\infty}\frac{\left(|\vec{k}|z_0\right)^j}{j!}} < \left(\frac{H}{z_0}\right)^n , \tag{B.3}$$

independently of the value of $\vec{k}$. Because we can choose the plane E below the observation surface S $(Z_0 > H)$, (see Figure 2-11) the series in Equation (B.1) is uniformly convergent over the entire wavenumber domain, by the Weierstrass M-test (e.g., Whittaker and Watson 1962, p. 49). This property is the same as the convergence of Parker's formula (Parker, 1973).

APPENDIX C

GRAVITY ANOMALY CAUSED BY A VERTICALLY EXPONENTIAL DENSITY CONTRAST MODEL

In this appendix, I first derive the formula for calculating the gravity anomaly caused by an exponential density contrast model. Then I show that the linear density contrast model is a special case of the exponential density contrast model.

C.1. Derivation of the Formula for Calculating the Gravity Anomaly due to an Exponential Density Contrast Model

An exponential density model is

$$\rho(z) = a + be^{-\mu z}. \tag{C.1}$$

The gravity effect due to this density model is given by

$$h = h_1 + h_2, \tag{C.2}$$

where the first term h_1, which is caused by a constant contrast density model a, can be calculated by Parker's formula. In the following paragraphs, I will derive the formula for calculating the second term h_2, which is caused by the exponential density contrast model.

The gravity anomaly caused by a single-point mass of a body $m(\vec{r}_0, z_0)$ located at $(\vec{r}_0, z_0)$ ($\vec{r}_0$ is the horizontal position vector, $\vec{r}_0 = x_0\vec{e}_x + y_0\vec{e}_y, \vec{e}_x$ and $\vec{e}_y$ are the unit vectors in x and y directions, respectively; z_0 is the vertical coordinate of the location of the point-mass).

$$dh_2(\vec{r}) = m(\vec{r}_0, z_0) g_d(\vec{r} - \vec{r}_0, z_0) dx_0 dy_0 dz_0,$$

where $g_d(\vec{r}, z_0)$ is the anomaly of unit mass, $\vec{r} = x\vec{e}_x + y\vec{e}_y$. Integration over the limits of the body yields the anomaly caused by the entire body:

$$h_2(\vec{r}) = \int_{z_1(\vec{r}_0)}^{z_2(\vec{r}_0)} \iint m(\vec{r}_0, z_0) g_d(\vec{r} - \vec{r}_0, z_0) dx_0 dy_0 dz_0 . \tag{C.3}$$

Fourier transform of both sides of Equation (C.3) and reordering yields

$$F[h_2(\vec{r})] = \iint_{\vec{r}_0} \int_{z_1(\vec{r}_0)}^{z_2(\vec{r}_0)} m(\vec{r}_0, z_0) F[g_d(\vec{r} - \vec{r}_0, z_0)] dz_0 dx_0 dy_0$$

$$= \iint_{\vec{r}_0} \int_{z_1(\vec{r}_0)}^{z_2(\vec{r}_0)} m(\vec{r}_0, z_0) e^{-i\vec{k}\cdot\vec{r}_0} F[g_d(\vec{r}, z_0)] dz_0 dx_0 dy_0 , \tag{C.4}$$

where

$$F[g_d(\vec{r}, z_0)] = 2\pi G e^{-|\vec{k}| z_0} \tag{C.5a}$$

is the expression of the single-point mass in the wavenumber domain; G is a gravitational constant; $\vec{k}$ is the wavenumber vector ($\vec{k} = k_x\vec{e}_x + k_y\vec{e}_y$); $z_1(\vec{r}_0)$ and $z_2(\vec{r}_0)$ are the top surface and the bottom surface of the layer, respectively; and

$$m(\vec{r}_0, z_0) = b e^{-\mu z_0} . \tag{C.5b}$$

Substituting Equations (C.5) into Equation (C.4) and performing the integration over z_0 yields

$$F[h(\vec{r})] = \frac{-2\pi G b}{(\mu + |\vec{k}|)} \iint_{\vec{r}_0} \left[e^{-(\mu + |\vec{k}|) z_2(\vec{r}_0)} - e^{-(\mu + |\vec{k}|) z_1(\vec{r}_0)} \right] e^{-i\vec{k}\cdot\vec{r}_0} dx_0 dy_0$$

$$= \frac{-2\pi G b}{\left(\mu + |\vec{k}|\right)} F\left[e^{-\left(\mu+|\vec{k}|\right) z_2(\vec{r}_0)} - e^{-\left(\mu+|\vec{k}|\right) z_1(\vec{r}_0)} \right]. \tag{C.6}$$

Let δ_1 and δ_2 be the median values of $z_1(\vec{r}_0)$ and $z_2(\vec{r}_0)$, respectively, then Equation (C.6) becomes

$$F[h_2(\vec{r})] = \frac{-2\pi G b}{\left(\mu + |\vec{k}|\right)} \times$$

$$\left\{ e^{-\left(\mu+|\vec{k}|\right)\delta_2} F\left[e^{-\left(\mu+|\vec{k}|\right)\left(z_2(\vec{r}_0)-\delta_2\right)} \right] - e^{-\left(\mu+|\vec{k}|\right)\delta_1} F\left[e^{-\left(\mu+|\vec{k}|\right)\left(z_1(\vec{r}_0)-\delta_1\right)} \right] \right\}.$$

Now replacing the two inner exponential terms by power series and performing some minor simplification yields the final equation

$$F[h_2(\vec{r})] = 2\pi G b \sum_{n=1}^{\infty} \frac{\left[-\left(\mu + |\vec{k}|\right)\right]^{n-1}}{n!} \times$$

$$\left\{ e^{-\left(\mu+|\vec{k}|\right)\delta_2} F\left[\left(z_2(\vec{r}_0) - \delta_2\right)^n\right] - e^{-\left(\mu+|\vec{k}|\right)\delta_1} F\left[\left(z_1(\vec{r}_0) - \delta_1\right)^n\right] \right\}. \tag{C.7}$$

Taking the inverse Fourier transform in Equation (C.7) yields the gravity anomaly h_2 caused by the second exponential term in Equation (C.1).

If let $z_2(\vec{r}_0) = g(\vec{r}_0) + z$ and $z_1(\vec{r}_0) = t(\vec{r}_0) + z$, Equation (C.7) can also be written as

$$F[h_2(\vec{r})] = 2\pi G b e^{-\left(\mu+|\vec{k}|\right) z} \sum_{n=1}^{\infty} \frac{\left[-\left(\mu + |\vec{k}|\right)\right]^{n-1}}{n!} F\left[g(\vec{r}_0)^n - t(\vec{r}_0)^n\right]. \tag{C.8}$$

Let μ be zero, Equation (C.1) is the constant density model, Equations (C.8) becomes

$$F\left[h_2(\vec{r})\right] = 2\pi G b e^{-(|\vec{k}|)z} \sum_{n=1}^{\infty} \frac{\left[-(|\vec{k}|)\right]^{n-1}}{n!} F\left[g(\vec{r}_0)^n - t(\vec{r}_0)^n\right],$$

which is Parker's formula for the constant density model.

C.2. Relationship Between the Linear Density Contrast Model and the Exponential Density Contrast Model

In the following paragraphs, I will show that a linear density model

$$\rho(z) = \rho_0 + cz \tag{C.9}$$

is a special case of the exponential model (Equation (C.1)). Reamer (1986) derived the formula for the linear density model, which is

$$\begin{aligned} F\left[h(\vec{r})\right] = 2\pi G e^{-|\vec{k}|z} \Bigg\{ &\rho_0 \sum_{n=1}^{\infty} \frac{\left(-|\vec{k}|\right)^{n-1}}{n!} F\left[g^n(\vec{r}_0) - t^n(\vec{r}_0)\right] \\ &+ c \sum_{n=2}^{\infty} (n-1) \frac{\left(-|\vec{k}|\right)^{n-2}}{n!} F\left[g^n(\vec{r}_0) - t^n(\vec{r}_0)\right] \Bigg\}. \end{aligned} \tag{C.10}$$

Based on the binomial expansion formula, I can write

$$\left[-\left(\mu + |\vec{k}|\right)\right]^{n-1} = \sum_{j=0}^{n-1} C_{n-1}^{j} (-\mu)^j \left(-|\vec{k}|\right)^{n-1-j}$$

assuming $\mu << 1$, the terms with higher order of μ can be omitted, then the equation above becomes

$$\left[-\left(\mu+|\vec{k}|\right)\right]^{n-1} = C_{n-1}^{0}\left(-|\vec{k}|\right)^{n-1} + C_{n-1}^{1}(-\mu)\left(-|\vec{k}|\right)^{n-2}, \qquad \text{(C.11)}$$

where

$C_{n-1}^{0} = 1$, and $C_{n-1}^{1} = n-1$,

because of assuming $\mu << 1$, then

$$e^{-\left(\mu+|\vec{k}|\right)z} \cong e^{-|\vec{k}|z}. \qquad \text{(C.12)}$$

Substituting Equations (C.11) and (C.12) into Equation (C.8), I obtain the formula of calculating the gravity anomaly caused by the second term (*cz*, *c* will be defined later.) of the linear density model in Equation (C.9).

$$F\left[h_2(\vec{r})\right] = 2\pi G b e^{-|\vec{k}|z}\left\{\sum_{n=1}^{\infty}\frac{\left(-|\vec{k}|\right)^{n-1}}{n!}F\left[g^n(\vec{r}_0)-t^n(\vec{r}_0)\right]\right.$$

$$\left.+\sum_{n=2}^{\infty}(n-1)(-\mu)\frac{\left(-|\vec{k}|\right)^{n-2}}{n!}F\left[g^n(\vec{r}_0)-t^n(\vec{r}_0)\right]\right\}. \qquad \text{(C.13)}$$

Parker's formula for the constant density contrast *a* model is

$$F\left[h_1(\vec{r})\right] = 2\pi G a e^{-|\vec{k}|z}\sum_{n=1}^{\infty}\frac{\left(-|\vec{k}^{n-1}|\right)}{n!}F\left[g^n(\vec{r}_0)-t^n(\vec{r}_0)\right]. \qquad \text{(C.14)}$$

If let $a + b = \rho_0$ and let $-b\mu = c$ and μ be very small, the summation of Equations (C.13) and (C.14) is equal to Equation (C.10). Therefore, Equation (C.8) can be used to calculate the anomaly caused by the linear density contrast model (C.9).

A linear density model in the paper of Reamer and Ferguson (1989), for example, is

$$\rho(z) = -750 + 100z \,\mathrm{kg/m^3}, \qquad 0 \le z \le 4\mathrm{km}. \qquad \text{(C.15)}$$

Let μ be 0.001, based on $-b\mu = c$ yields b = -100,000, and from $a + b = \rho_0$, yields a = 99,250. Therefore, an approximate exponential density contrast model for the linear density contrast model (C.15) is

$$\rho(z) = 99{,}250 - 100{,}000e^{-0.001z}, \qquad 0 \le z \le 4\mathrm{km}. \qquad \text{(C.16)}$$

REFERENCES

Abdelrahman, E. M., Riad, S., Refai, E., and Amin, Y., 1985, On the least-squares residual anomaly determination: Geophysics, **50**, 473-480.

Athy, L. F., 1930, Density, porosity and compaction of sedimentary rocks: Bull. Am. Assn. Petr. Geol., **14**, 1-14.

Berendsen, P., Borcherding, R. M., Doveton, J., Gerhard, L., Newell, K. D., Steeples, D., and Watney, W. L., 1988, Texaco Poersch #1, Washington County, Kansas-Preliminary geologic report of the pre-Phanerozoic rocks: Kansas Geological Survey, Open-file report **88-22**.

Bhattacharyya, B. K.,1964, Magnetic anomalies due to prism-shaped bodies with arbitrary polarization: Geophysics, **29**, 517-531.

Bhattacharyya, B. K., and Chan, K. C., 1977, Reduction of magnetic and gravity data on an arbitrary surface acquired in a region of high topographic relief: Geophysics, **42**, 1411-1430.

Bickford, M. E., Harrower, K. L., Nussbaum, R. L., Thomas, J. J., Nelson, B. K., and Hoppe, W. J., 1981, Rb-Sr and U-Pb and geochronology and distribution of rock types in the Precambrian basement of Missouri and Kansas: Geological Society of America Bulletin, Part I, **92**, 323-314.

Bickford, M. E., Mose, D. G., Wetherill, G. W., and Franks, P. C., 1971, Metamorphism of Precambrian granite xenoliths in a mica peridotite at Rose Dome, Woodson County, Kansas: Part I, Rb-Sr isotopic studies: Geological Society of American Bulletin, **82**, 2863-2868.

Bickford, M. E., Van Schmus, W. R., and Zietz, I., 1986, Proterozoic history of the midcontinent region of North America: Geology, **14**, 492-496.

Blakely, R. J., 1981, A program for rapidly computing the magnetic anomaly over digital topography: U. S. Geol. Survey, Open-file report **81-298**.

Bott, M. H. P., 1960, The use of rapid digital computing methods for direct gravity interpretation of sedimentary basins: Geophys. J., **3**, 3-67.

Cadwell, J. H., 1961, A least squares surface fitting program: Comput. J. **3**, 266-269.

Cady, J. W., 1980, Calculation of gravity and magnetic anomalies of finite-length right polygonal prisms: Geophysics, **45**, 1507-1512.

Carmichael, R. S. (ed.), 1989, Practical handbook of physical properties of rocks and minerals: CRC Press, Boca Raton, Florida.

Chai, Y., and Hinze, W. J., 1988, Gravity inversion of an interface above which the density contrast varies exponentially with depth: Geophysics, **53**, 837-845.

Chenot, D., and Debeglia, N., 1990, Three-dimensional gravity or magnetic constrained depth inversion with lateral and vertical variation of contrast: Geophysics, **55**, 327-335.

Clark, R. E., Kubik, L. P., and, Phillips, L. P., 1963, Orthogonal polynomial least squares surface fit: Comm. ACM., **6**, 162-163.

Cole, V. B., 1976, Configuration of the top of the Precambrian rocks in Kansas: Kansas Geological Survey, Map M-7, scale 1:500,000, 1 sheet.

Cole, V. B., and Watney, W. L., 1985, List of Kansas wells drilled into Precambrian rocks: Kansas Geological Survey, Subsurface geology series **7**.

Cordell, L., 1973, Gravity analysis using an exponential density-depth funtion--San Jacinto graben, California: Geophysics, **38**, 684-690.

Cordell, L., and Henderson, R. B., 1968, Iterative three-dimensional solution of gravity anomaly data using a digital computer: Geophysics, **33**, 596-601.

Cordell, L., and McCafferty, A. E., 1989, A terracing operator for physical property mapping with potential field data: Geophysics, **54**, 621-634.

Dampney, C. N. G., 1969, The equivalent source technique: Geophysics, **34**, 39-53.

Davis, J. C., 1986, Statistics and data analysis in geology (2nd edition): New York, John Wiley & Sons, Inc.

Dobrin, M. B., 1976, Introduction to geophysical prospecting (3rd edition): McGraw-Hill, Book Company.

Dobrin, M. B., and Savit, C. H., 1988, Introduction to geophysical prospecting (4th edition): McGraw-Hill, Inc.

Ferguson, J. F., Felch, R.N., Aiken, C. L. V., Oldow, J. S., and Dockery, H., 1988, Model of the Bouguer gravity and geologic structure at Yucca Flat, Nevada: Geophysics, **53**, 231-244.

Franks, P. C., Bickford, M. E., and Wagner, H. C., 1971, Metamorphism of Precambrian granite xenoliths in a mica peridotite at Rose Dome, Woodson County, Kansas: Part II, Petrologic and mineralogic studies: Geological Society of American Bulletin, **82**, 2869-2899.

Garland, G. D., 1979, Introduction to geophysics-Mantle, Core, and Crust (2nd edition): W. B. Saunders Company.

Granser, H., 1986, Convergence of iterative gravity inversion: Geophysics, **51**, 1146-1147.

Granser, H., 1987, Nonlinear inversion of gravity data using the Schmidt-Lichtenstein approach: Geophysics, **52**, 88-93.

Greig, P. B., 1959, Geology of Pawnee County, Oklahoma: Oklahoma Geol. Survey Bull. **83**.

Gusip, F., 1987, Frequency-domain reduction of potential field measurements to a horizontal plane: Geoexpl., **24**, 87-98.

Halliday, D., and Resnick, R., 1981, Fundamentals of physics (2nd edition): John Wiley & Sons, Inc.

Henderson, R. G., and Cordell, L., 1971, Reduction of unevenly spaced potential field data to a horizontal plane by means of finite harmonic series: Geophysics, **36**, 856-866.

Hildebrand, G. M., Steeples, D. W., Knapp, R. W., Miller, R. D., and Bennett, B. C., 1988, Microearthquakes in Kansas and Nebraska 1977-1987: Seismological Research Letters, **59**, 159-163.

Hubbert, M. K., 1948, A line integral method of computing the gravimetric effect of two-dimensional mass: Geophysics, **13**, 215-225.

Jacobsen, B. H., 1987, A case for upward continuation as a standard separation filter for potential-field maps: Geophysics, **52**, 1138-1148.

Kane, M. F., and Godson, R. H., 1985, Features of a pair of long-wavelength (> 250 km) and short-wavelength (< 250 km) Bouguer gravity maps of the United States; *in*, The Utility of Regional Gravity and Magnetic Anomaly Maps, W. J. Hinze, ed.: Society of Exploration Geophysicists, Special Volume, 46-61.

Kieniewicz, P. M., and Luyendyk, B. P., 1986, A gravity model of the basement structure in the Santa Maria Basin, California: Geophysics, **51**, 1127-1140.

Krige, D. G., 1966, Two-dimensional weighted moving average trend surface for ore valuation, *in* Proc. Symposium on Mathematical Statistics and computer Applications in Ore Valuation, Mar. 7-8: Jour. South African Inst. Mining and Metallurgy, Johannesburg, 13-38.

Lam, C. K., 1986, Interpretation of state-wide gravity survey of Kansas: Ph.D. thesis, University of Kansas, Lawrence.

Lam, C. K., and Yarger, H. L., 1989, State gravity map of Kansas: Kansas Geological Survey, Bulletin **226**, 185-196.

Miller, R. D., 1983, Crustal study in Kansas using earthquake seismograms: M.S. thesis, University of Kansas, Lawrence.

Mittermayer, E., 1969, Numerical formulas for the Geodetic Reference System 1967: Bullentino di Geofisca Teorica ed Applicata, **11**, 96-107.

Murthy, I. V. R., and Rao, D. B., 1979, Gravity anomalies of two-dimensional bodies of irregular cross-section with density contrast varying with depth: Geophysics, **44**, 1525-1530.

Nagy, D., 1966, The gravitational attraction of a right rectangular prism: Geophysics, **31**, 362-371.

Newell, K. D., Watney, W. L., Cheng, S. W. L., and Brownrigg, R. L., 1987, Stratigraphic and spatial distribution of oil and gas production in Kansas: Subsurface geology series **9**, Kansas Geological Survey,

Nettleton, L. L., 1976, Gravity and magnetics in oil prospecting: McGraw-Hill Book Co.

Oldenburg, D. W., 1974, The inversion and interpretation of gravity anomalies: Geophysics, **39**, 526-536.

Parker, R. L., 1973, The rapid calculation of potential anomalies: Geophys. J. Roy. Astr. Soc., **31**, 447-455.

Parker, R. L., and Huestis, S. P., 1974, The inversion of magnetic anomalies in the presence of topography: J. Geophys. Res., **79**, 1587-1593.

Pawlowski, R. S., and Hansen, R. O., 1990, Gravity anomaly separation by Wienner filtering: Geophysics, **55**, 539-548.

Peters, L. J., 1949, The direct approach to magnetic interpretation and its practical application: Geophysics, **14**, 290-320.

Pilkington, M., 1990, Private communication.

Pilkington, M., and Crossley, D. J., 1986, Determination of crustal interface topography from potential field: Geophysics, **51**, 1277-1284.

Pilkington, M., and Urquhart., W. E. S., 1990, Reduction of potential field data to a horizontal plane: Geophysics, **55**, 549-555.

Plouff, D., 1976, Gravity and magnetic fields of polygonal prisms and application to magnetic terrain corrections: Geophysics, **41**, 727-741.

Pustisek, A. M., 1990, Noniterative three-dimensional inversion of magnetic data: Geophysics, **55**, 782-785.

Rall, L. B., 1974, Theory of nonlinear integral equations; *in*, Numerical solution of integral equations, Delves, L. M., and Walsh, J., Eds.: Clarendon Press, 207-222.

Reamer, S. K., 1986, Improvements to the Fourier gravity inversion method with applications: M.Sc. thesis, Univ. of Texas at Dallas.

Reamer, S. K., and Ferguson, J. F., 1989, Regularized two-dimensional Fourier gravity inversion method with application to Silent Canyon caldera, Nevada: Geophysics, **54**, 486-496.

Sampson, R., 1988, SURFACE III: Interactive Concepts Inc.

Snedecor, G. W., and Cochran, W. G., 1989, Statistical Method (8th edition): Iowa State University Press, Ames, Iowa.

Somanas, C., Knapp, R. W., Yarger, H., and Steeples, D., 1989, Geophysical model of the Midcontinent Geophysical Anomaly in northeastern Kansas: Kansas Geological Survey Bulletin **226**, 215-228.

Steeples, D. W., and Bickford, M. E., 1981, Piggyback drilling in Kansas: An example for the Continental Scientific Drilling Program: Transactions of the American Geophysical Union, **62**, 473-476.

Steeples, D. W., 1982, Structure of the Salina-Forest City interbasin boundary from seismic studies: University of Missouri Rolla, Journal, No. **3**, 55-81.

Steeples, D. W., and Miller, R. D., 1989, Kansas refraction profile: Kansas Geological Survey, Bulletin **226**, 129-148.

Steeples, D. W., 1992, Private communication.

Syberg, F. J. R., 1972, Potential field continuation between general surfaces: Geophys. Prosp., **20**, 267-282.

Talwani, M., Worzel, J. L., and Landisman, M., 1959, Rapid gravity computations for two-dimensional bodies with application to the Mendocino submarine fracture zone: J. Geophys. Res., **64**, 49-59.

Tanner, W. F., 1959, Permo-Pennsylvanian paleogeography of part of Oklahoma: Jour. Sed. Petrol., **29**, 326-335.

Telford, W. M., Geldart, L. P., Sheriff, R. E., and Keys, D. A., 1982, Applied geophysics: Cambridge University Press.

Tsuboi, C., 1965, Calculation of Bouguer anomalies with due regard to the anomaly in the vertical gravity gradient: Japan Acad. Proc., **41**, 386-391.

Whittaker, E. T., and Watson, G. N., 1962, A course of modern analysis: Cambridge University Press, Cambridge.

Woelk, T. S., and Hinze, W. J., 1991, Model of the midcontinent rift system in northeastern Kansas: Geology, **19**, 277-280.

Xia, J., 1986, Solving inverse problem of two-dimensional single density interface by singular value decomposition: Computing Techniques for Geophysical and Geochemical Exploration, Ministry of Geology and Minerals, China, **8**, 128-134.

Xia, J., and Sprowl, D. R., 1990, Inversion of potential-field data by iterative forward modeling in the wavenumber domain: 60th Ann. Internt. Mtg., Soc. Expl. Geophys., Expanded Abstracts, 635-638.

Xia. J., 1991, Computer program of inversion of potential-field data by iterative forward modeling: Kansas Geological Survey Open file report, **91 - 14**.

Xia, J., and Sprowl, D. R., 1991, Correction of topographic distortions in gravity data: Geophysics, **56**, 537-541.

Xia, J., and Sprowl, D. R., and Adkins-Heljeson, D., 1991, A fast and accurate approach: Correction of topographic distortions in potential-field data: 61th Ann. Internt. Mtg., Soc. Expl. Geophys., Expanded Abstracts, 626-629.

Xia, J., and Sprowl, D. R., 1992, Inversion of potential field data by iterative forward modeling in the wavenumber domain: Geophysics, **57**, 126-130.

Yarger, H. L., 1985, Kansas basement study using spectrally filtered aeromagnetic data; *in*, The Utility of Regional Gravity and Magnetic Anomaly Maps, W. J. Hinze, ed.: Society of Exploration Geophysicists, Special Volume, 213-232; Kansas Geological Survey, Open-file Report **83-9**, (1983).

Yarger, H. L., 1989, Major magnetic features in Kansas and their possible geologic significance: Kansas Geological Survey, Bulletin **226**, 197-213.

Yarger, H. L., Robertson, R. R.,Martin, J. A., Ng, K., Sooby, R. L., and Wentland, R. L., 1981, Aeromagnetic map of Kansas: Kansas Geological Survey, Map *M*-16, scale 1:500,000, color interval 200 nT, contour interval 50 nT.

Yarger, H. L., 1983, Regional interpretation of Kansas aeromagnetic data: Kansas Geological Survey, Geophysics series **1**.

Yarger, H. L., Robertson, R. R., and Wentland, R. L., 1978, Diurnal drift removal from aeromagnetic data using least squares: Geophysics, **46**, 1148-1156.